National Library of Canada
Acquisitions and Bibliographic Services Branch
395 Wellington Street
Ottawa, Ontario
K1A 0N4

Bibliothèque nationale du Canada
Direction des acquisitions et des services bibliographiques
395, rue Wellington
Ottawa (Ontario)
K1A 0N4

Your file Votre référence

Our file Notre référence

NOTICE

The quality of this microform is heavily dependent upon the quality of the original thesis submitted for microfilming. Every effort has been made to ensure the highest quality of reproduction possible.

If pages are missing, contact the university which granted the degree.

Some pages may have indistinct print especially if the original pages were typed with a poor typewriter ribbon or if the university sent us an inferior photocopy.

AVIS

La qualité de cette microforme dépend grandement de la qualité de la thèse soumise au microfilmage. Nous avons tout fait pour assurer une qualité supérieure de reproduction.

S'il manque des pages, veuillez communiquer avec l'université qui a conféré le grade.

La qualité d'impression de certaines pages peut laisser à désirer, surtout si les pages originales ont été dactylographiées à l'aide d'un ruban usé ou si l'université nous a fait parvenir une photocopie de qualité inférieure.

Canada

BIOLOGICAL APPLICATIONS OF SCANNING TUNNELING MICROSCOPY AND SCANNING FORCE MICROSCOPY

By

Wei Xu

SUBMITTED IN PARTIAL FULFILLMENT OF THE
REQUIREMENTS FOR THE DEGREE OF
DOCTOR OF PHILOSOPHY
AT
DALHOUSIE UNIVERSITY
HALIFAX, NOVA SCOTIA
NOVEMBER, 1994

ISBN 0-612-05244-3

Canada

Name Wei Xu

Dissertation Abstracts International is arranged by broad, general subject categories. Please select the one subject which most nearly describes the content of your dissertation. Enter the corresponding four-digit code in the spaces provided.

Physics
SUBJECT TERM

0611
SUBJECT CODE

U·M·I

Subject Categories

THE HUMANITIES AND SOCIAL SCIENCES

COMMUNICATIONS AND THE ARTS
Architecture 0729
Art History 0377
Cinema 0900
Dance 0378
Fine Arts 0357
[illegible] 0723
[illegible] ..... [illegible]
[illegible] ..... [illegible]
Music 0413
Speech Communication 0459
Theater 0465

EDUCATION
General 0515
Administration 0514
Adult and Continuing 0516
Agricultural 0517
Art 0273
Bilingual and Multicultural 0282
Business 0688
Community College 0275
Curriculum and Instruction 0727
Early Childhood 0518
Elementary 0524
Finance 0277
Guidance and Counseling 0519
Health 0680
Higher 0745
History of 0520
Home Economics 0278
Industrial 0521
Language and Literature 0279
Mathematics 0280
Music 0522
Philosophy of 0998
Physical 0523
Psychology 0525
Reading 0535
Religious 0527
Sciences 0714
Secondary 0533
Social Sciences 0534
Sociology of 0340
Special 0529
Teacher Training 0530
Technology 0710
[illegible] ..... [illegible]

LANGUAGE, LITERATURE AND LINGUISTICS
Language
- General 0679
- Ancient 0289
- Linguistics 0290
- Modern 0291

Literature
- General 0401
- Classical 0294
- Comparative 0295
- Medieval 0297
- Modern 0298
- African 0316
- American 0591
- Asian 0305
- Canadian (English) 0352
- Canadian (French) 0355
- English 0593
- Germanic 0311
- Latin American 0312
- Middle Eastern 0315
- Romance 0313
- Slavic and East European 0314

PHILOSOPHY, RELIGION AND THEOLOGY
Philosophy 0422
Religion
- General 0318
- [illegible] ..... [illegible]
- [illegible] ..... [illegible]
- [illegible] ..... [illegible]

Theology 0469

SOCIAL SCIENCES
American Studies 0323
Anthropology
- Archaeology 0324
- Cultural 0326
- Physical 0327

Business Administration
- General 0310
- Accounting 0272
- Banking 0770
- [illegible] ..... [illegible]
- [illegible] ..... [illegible]

Economics
- General 0501
- Agricultural ..... [illegible]
- Commerce-Business ..... [illegible]
- Finance 0508
- History 0509
- Labor 0510
- Theory 0511

Folklore 0358
Geography 0366
Gerontology 0351
History
- General 0578
- Ancient 0579
- Medieval 0581
- Modern 0582
- Black 0328
- African 0331
- Asia, Australia and Oceania 0332
- Canadian 0334
- European 0335
- Latin American 0336
- Middle Eastern ..... [illegible]
- [illegible] ..... [illegible]

Law 0398
Political Science
- General 0615
- International Law and Relations 0616
- Public Administration 0617

Recreation 0814
Social Work 0452
Sociology
- General 0626
- Criminology and Penology 0627
- Demography 0938
- Ethnic and Racial Studies 0631
- Individual and Family Studies 0628
- Industrial and Labor Relations 0629
- Public and Social Welfare 0630
- Social Structure and Development 0700
- Theory and Methods 0344

Transportation 0709
Urban and Regional Planning 0999
Women's Studies 0453

THE SCIENCES AND ENGINEERING

BIOLOGICAL SCIENCES
Agriculture
- General 0473
- Agronomy 0285
- Animal Culture and Nutrition 0475
- Animal Pathology 0476
- Food Science and Technology 0359
- Forestry and Wildlife 0478
- Plant Culture 0479
- Plant Pathology 0480
- Plant Physiology 0817
- Range Management 0777
- Wood Technology 0746

Biology
- General 0306
- Anatomy 0287
- Biostatistics 0308
- Botany 0309
- Cell 0379
- Ecology 0329
- Entomology 0353
- Genetics 0369
- Limnology 0793
- Microbiology 0410
- Molecular 0307
- Neuroscience 0317
- Oceanography 0416
- Physiology 0433
- Radiation 0821
- Veterinary Science 0778
- Zoology 0472

Biophysics
- General 0786
- Medical 0760

EARTH SCIENCES
Biogeochemistry 0425
Geochemistry 0996
Geodesy 0370
Geology 0372
Geophysics 0373
Hydrology 0388
Mineralogy 0411
Paleobotany 0345
Paleoecology 0426
Paleontology 0418
Paleozoology 0985
Palynology 0427
Physical Geography 0368
Physical Oceanography 0415

HEALTH AND ENVIRONMENTAL SCIENCES
Environmental Sciences 0768
Health Sciences
- General 0566
- Audiology 0300
- Chemotherapy 0992
- Dentistry 0567
- Education 0350
- Hospital Management 0769
- Human Development 0758
- Immunology 0982
- Medicine and Surgery 0564
- Mental Health 0347
- Nursing 0569
- Nutrition 0570
- Obstetrics and Gynecology 0380
- Occupational Health and Therapy 0354
- Ophthalmology 0381
- Pathology 0571
- Pharmacology 0419
- Pharmacy 0572
- Physical Therapy 0382
- Public Health 0573
- Radiology 0574
- Recreation 0575
- Speech Pathology 0460
- Toxicology 0383

Home Economics 0386

PHYSICAL SCIENCES
Pure Sciences
Chemistry
- General 0485
- Agricultural 0749
- Analytical 0486
- Biochemistry 0487
- Inorganic 0488
- Nuclear 0738
- Organic 0490
- Pharmaceutical 0491
- Physical 0494
- Polymer 0495
- Radiation 0754

Mathematics 0405
Physics
- General 0605
- Acoustics 0986
- Astronomy and Astrophysics 0606
- Atmospheric Science 0608
- Atomic 0748
- [illegible] ..... [illegible]
- [illegible] ..... [illegible]
- High Energy 0798
- Fluid and Plasma 0759
- Molecular 0609
- Nuclear 0610
- Optics 0752
- Radiation 0756
- Solid State 0611

Statistics 0463

Applied Sciences
Applied Mechanics 0346
Computer Science 0984
Engineering
- General 0537
- Aerospace 0538
- [illegible] ..... [illegible]
- [illegible] ..... [illegible]
- [illegible] ..... [illegible]
- Chemical 0542
- Civil 0543
- [illegible] ..... [illegible]
- [illegible] ..... [illegible]
- [illegible] ..... [illegible]
- Marine 0547
- Materials Science 0794
- Mechanical 0548
- Metallurgy 0743
- Mining 0551
- Nuclear 0552
- Packaging 0549
- Petroleum 0765
- Sanitary and Municipal 0554
- System Science 0790

Geotechnology 0428
Operations Research 0796
Plastics Technology 0795
Textile Technology 0994

PSYCHOLOGY
General 0621
Behavioral 0384
Clinical 0622
Developmental 0620
Experimental 0623
Industrial 0624
Personality 0625
Physiological 0989
Psychobiology 0349
Psychometrics 0632
Social 0451

Table of Contents

List of Figures

Abstract

The present study focuses on development of techniques of STM and SFM for biological applications and is divided into two parts: investigation of metal-coating techniques for STM imaging of biological materials; and development of a new SFM technique for the measurement of the elastic properties of biological materials.

We used Pt/Ir coatings prepared by a simple procedure and obtained ~1 nm resolution on S-layer sheath of *Methanospirillum hungatei* (Mh). The 3 nm x 3 nm 2-D lattice structure of sheath was observed for the first time by STM. The surface characteristics of cell plugs of Mh was resolved, and the register alignment of the plug layers was identified for the first time. Effects of film grain size, tip convolution, and tip-sample interaction on the imaging resolution and interpretation are discussed.

A new technique was developed which measures elastic properties by bending or stretching biological material suspended on grooves etched in a GaAs substrate. We measured the Young's modulus of β-chitin fibres with cross sections less than 40 nm x 20 nm to be (0.5-1.5) x 10^{11} N/m^2. In the case of Mh sheath, a homogeneous approximation gave a Young's modulus of (2-5) x 10^{10} N/m^2, while an inhomogeneous hoop model provided information about the molecular bonding of the sheath. By testing the sheath to its breaking strength we estimated the maximum internal pressure as well as the maximum extension the sheath can sustain, which gave insight into possible biological mechanisms.

Symbols and abbreviations

a spacing between springs in hoop joints

CITS current imaging tunneling spectroscopy

d surface indentation

D tip-sample distance

ΔQ change in parameter Q

δ centre deflection of a material under a normal load

δ_0 initial sag

δ_m maximum deflection at elastic limit

$\delta(x)$ deflection of a clamped beam at position x from one of the two ends

e electron charge

E Young's modulus

E^* $\pi E/(1-\nu^2)$, where ν is the Poisson ratio

$\bar{E}$ electron energy

E_f Fermi energy

ϵ_i extension of the ith joint in the hoop model

ϵ_t total extension of the half sheath

Ξ bonding energy of hoop joints

f(E) Fermi function

F force

F_0 imaging force

F_m maximum force at elastic limit

$\hbar$ $h/2\pi$, where h is Planck's constant

θ_m maximum angle in the trapezoidal model

I tunneling current

j tunneling current density

k inverse decay length of electron density outside the surface of an electrode

K spring constant

K_c spring constant of the cantilever

K_h spring constant of the hoop joints

K_i stiffness of the tip-sample system

K_m stiffness of the SFM system

K_s spring constant of the sample

K_t spring constant of the tip

l length of the cantilever

2L length of the material

$2L_0$ span distance

L_{eff} lateral resolution

m electron mass

m^* 0.24 m_b, effective mass of a ractangular beam of mass m_b

$M_{\mu\nu}$ tunneling matrix element between states μ and ν

Mh Methanospirillum hungatei

PM purple membrane

P pressure

PMT photomultiplier tube

ρ density of mass

$\rho(R_t,E_f)$ local density of states (LDOS) at Fermi level

r_t effective tip contact radius

R tip radius

R_t position of a tip as a mathematical point source of current

s tunneling barrier width

S_{ieff} effective width of the i^{th} section in the trapezoidal region

SEM scanning electron microscopy

STM scanning tunneling microscopy

SFM scanning force microscopy

TEM transmission electron microscopy

t thickness of a beam or plate

T tension

T_i tension per unit angle in the i^{th} section

T_c tension per unit angle in the central section

$\bar{T}$ tension per unit length

T_m maximum tension at elastic limit

UHV ultra high vacuum

V voltage applied to a tunnel junction

V(z) barrier potential function

w width of the material

w_i width of the ith joint in the hoop model

w_t width of the trapezoidal sheath at the tip end

W_{eff} effective width

ϕ tunneling barrier height

ϕ_a apparent barrier height

x,y,z Cartesian coordinates of real space

χ stress function

Z cantilever deflection

Z_g gap between the z-piezo and the back of the cantilever

Z_p distance between the z-piezo and the back of the sample

Z_s height of the sample

Z_t length of the tip

ψ electron wavefuction

ω_0 $2\pi\nu_0$, where ν_0 is the resonant frequency

Acknowledgements

I wish to thank my supervisor Dr. Brad Blackford for his constant encouragement and support during my study at Dalhousie, and for his numerous suggestions and helpful discussions on this research work. I also wish to thank Dr. Manfred Jericho for his advice and helpful discussions, especially on the analysis and interpretation of the experimental results. I extend my appreciation to Dr. Peter Mulhern for his assistance during the completion of this work, in particular, for his helpful comments regarding the editing of this manuscript.

Drs. Terry Beveridge, Max Firtel and Gordon Southam at Department of Microbiology, University of Guelph, provided the Mh sheath and plug. Dr. L.Fritz at National Research Council-Canada, Institute for Marine Biosciences, provided the chitin samples. Dr. I.Templeton at Institute for Microstructural Sciences at the National Research Council-Canada, Ottawa, supplied the GaAs grating for the elasticity measurements. Lynn Maillet, operator of the Transmission Electron Microscope, prepared the TEM images of tips. Dr. Gary Faulkner at Department of Microbiology provided the use of their freeze-etch unit for the electron beam bombardment evaporation of Pt/Ir/C films. I express my gratitude to all the above-named.

Lastly, I gratefully acknowledge the graduate scholarship received from Dalhousie.

Part 1 STM of metal coated biological structures

1 Introduction

1.1 General background of the STM

The scanning tunneling microscope (STM), invented by G.Binnig, H.Rohrer and coworkers in 1981 [1,2], is a successful combination of vacuum tunneling with electronic feedback and a piezoelectric drive system.

The basic principle of operation of the STM is illustrated in Figure 1.1. A probe that is sharp and electrically conductive is brought close enough to the sample surface that electrons can tunnel through the vacuum barrier separating tip and sample. A small voltage applied between the tip and the surface results in a current flow from one electrode to the other. A piezoelectric drive system and a feedback loop is used to keep the tip-sample distance constant while the tip is scanned over the surface. A map of the surface topography can be obtained by recording the z-piezo voltage. The exponential dependence of the tunneling current on the tip-sample spacing is the key to the high spatial resolution which can be achieved with the STM. STM can provide real-space images of surfaces of conducting materials down to the atomic scale. STM has made a dramatic impact in fields as diverse as material science, semiconductor physics, biology, electrochemistry, catalysis, surface thermodynamics, micromechanics, etc.

1.2 Biological applications

The attempt to use the STM for the visualization of biological macromolecules started soon after the invention of the STM. The successful imaging of DNA deposited on a carbon

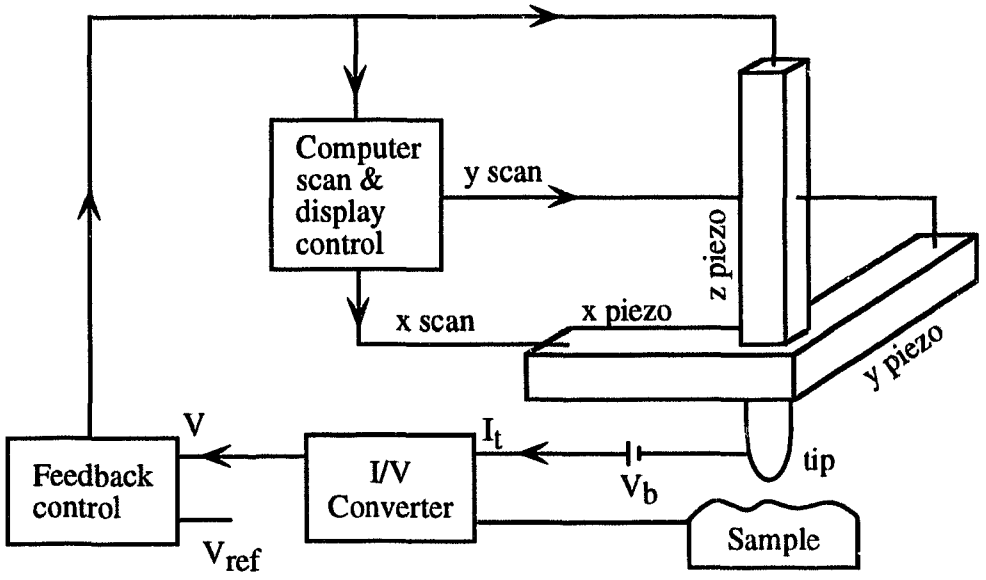

Figure 1.1: Schematic of the scanning tunneling microscope.

film [3], and later, the bacteriophage ϕ29 [4], indicated that imaging biological material is possible provided that the specimen is deposited on a conducting surface. Bio-STM studies have since increased steadily. The specimens investigated range from single molecules to whole cells [5,6].

Two major problems with STM imaging of biological materials are the low electric conductivity of biomolecules and the often poor bonding of the specimen to the substrate. The tip damages the specimen as it tries to get closer to the substrate in order to maintain the tunneling current, and the lateral force moves the specimen around, making imaging difficult, or even pushes it away and no image is obtained.

In cases where the specimen has some conductivity, or is thin enough to tunnel through, the bonding problem is thought to be the main obstacle. One approach to avoid the problem caused by poor bonding is to try alternative substrates to Highly oriented pyrolytic graphite (HOPG), which interact with the biomaterials more strongly and therefore efficiently immobilize the specimen and provide good electric contact. Substrates such as crystalline WSe_2 [7], epitaxial Au film on mica [8,9] and Flame-grown Au ball crystals [10,11] have been used with some success. Standard transmission electron microscopy (TEM) supports such as carbon (C) or platinum-carbon (Pt-C) films evaporated on cleaved mica platelets have also been used successfully in a number of STM experiments as supports for biomaterials [12-14]. Binding biological material strongly to surfaces by chemisorption has attracted some interest [15-17].

A special technique "hopping mode" which tries to minimize the lateral forces exerted onto biological samples during scanning was reported by Jericho et al. [18]. The tip is periodically withdrawn and reapproached during scanning to prevent the lateral stress build-up. Successful application of the hopping technique were reported on bare Mh sheath fragments [19, 20] and on bare pepsin molecules [19]. A similar technique "tapping mode" was used for SFM imaging of weakly bonded materials [21,22]. The cantilever being oscillated

near its resonance frequency periodically taps the sample surface during scanning, and the z height information is obtained from the amplitude change of the oscillating lever.

Alternatively, the immobilization and electric connection can be accomplished by a conductive film deposited on top of the specimen by vacuum evaporation. This method is especially useful for large biological structures, since it is relatively easy to obtain reproducible, trustworthy images that are not influenced by the low conductivity of the biological macromolecular structures. The coating sets a limit for the resolution which can be achieved with coated preparation. However when using a fine-grain, stable coating film, the method permits direct three-dimensional visualization of structural details at the level of individual subunits in protein complexes. Successful results have been obtained on Pt/Ir/C coated freeze-dried phage T4 polyhead [23], HPI layer [24] and recA-DNA [25], on Pt/C coated HPI layer and type IV collagen [26], and on Pt coated Mh sheath [27,28].

Imaging of some bare proteins was made possible by using extremely small tunneling current (a fraction of pA) and at relatively high voltage (up to 8V), and the resolutions in these cases were similar to that of metal coated preparations. Examples are protein HPI layer [26] and purple membrane PM [13]. However, the images sometimes showed negative contrast as well as positive contrast, and the contrast depended on the sharpness of the tip. Humidity was found very important for successful imaging. The conduction mechanism in bare sample imaging is not understood even though some ideas have been proposed.

In an effort to understand the conduction mechanism in the imaging of bare samples, spectroscopic measurements were carried out. Lindsay et al. [29] measured the I-V curves over gold substrate and over DNA aggregates, and observed conduction enhancement over DNA. Their results suggested an electron tunneling mechanism and the enhancement of conductivity over DNA adsorbate was a result of modification of the electronic properties of the adsorbate by contact with the tip.

1.3 Summary of early investigations with metal-coating technique

To overcome the problems of the insufficient electric conductivity of biological materials and their poor binding to the substrate STM experiments on metal-coated or replicated objects have begun. The earliest results were reported for DNA [25] and for bacteriophage T4 type polyheads by Amrein et al. [23], for Mh sheath by Blackford et al. [27,28], for bacteriophage T7 by Garcia et al. [30], and for HPI-layer and also for type IV collagen by Guckenberger et al. [26].

The most extensive and successful STM studies of coated biological materials was reported on freeze dried specimens coated with Pt/Ir/C films. Amrein et al. obtained images of the recA-DNA complex that equalled or exceeded results obtained with electron microscopy [25]. Later, this group achieved a lateral resolution of 1.5 nm on T4 and HPI-layer coated with 1-2 nm thick Pt/Ir/C film [23]. The P6 symmetry of both these crystalline protein layers was observed, with lattice constants of 13 and 18 nm for T4 polyheads and HPI layer, respectively. The ratio of the platinum, iridium, and carbon components in the films were found to be important to the granularity of the coating and resolution [24].

Blackford et al. [27,28] has extensively studied the outer sheath component of the bacteria Methanospirillum hungatei, using both Au and Pt coatings on HOPG substrates. The corrugations expected from EM studies at multiples of 3 nm running perpendicular to the sheath axis could be resolved easily. However, the 3 nm x 3 nm lattice structure expected on the basis of diffraction studies [31] was not seen at that time in the STM images, nor had it been detected in conventional scanning electron microscopy (SEM) or transmission electron microscopy (TEM) [32]. They also imaged the individual hoops (carbon coated) which comprise the Mh sheath tubular structure [33]. The resolution on these structures was limited to ~3 nm.

Other materials and coatings reported are bacteriophage T7 and DNA strands coated

with Pt/C on HOPG substrates [34], macromolecule fibronectin coated with Pt/C on mica [35]. The resolutions obtained in these studies were about 5 nm.

The high vertical resolution of STM provides valuable thickness data to complement EM thickness data which, by comparison to STM, are imprecise and difficult to obtain. Coated samples are best suited for absolute height measurements. The height sensitivity on coated biological samples was exploited by Fisher et al. [36], Wang et al. [37], and Blackford et al. [27,28]. Thickness values were found not to be influenced significantly by substrate and preparation method for some materials [36,37], but influenced by coating and preparation method for some other materials [27,28,37].

A method closely related to metal coating, the replica technique, was also investigated for STM imaging of biological structures. Zasadzinski et al. [38] studied freeze-fracture replicas of dimyristoylphosphatidylcholine (DMPC) bilayers. They observed the ripple phase and measured the period (13 nm) and amplitude (4.5 nm) with a lateral resolution of about 3 nm. Blackford et al. [39] reported a different technique in which the biological structures are first deposited on a flat HOPG substrate and then over-coated with a thick metallic film. The metallic film is then peeled off from the substrate and its underside was scanned by the STM to reveal indentation-type replicas. The technique was used on Mh sheath and gave a lateral resolution of about 3 nm, which was similar to that for metal coated sheath specimens.

1.4 Aim and scope of the present investigation

The present study is an investigation of the coating technique for STM imaging of large biological materials. The aim is to study the ability of STM to reveal three dimensional features of biological structures, and its capability to be used as a routine structural analysis tool complementary to TEM.

There have been reports of successful imaging of some specimens with the coating

technique, which involved use of different coating materials and different preparation methods. It was hoped that a detailed examination of the effects of coating films, preparation methods and probe tips on the image will provide information which can guide us to optimize this technique for STM imaging of biological materials.

The samples investigated are the S-layer sheath and the end plug, two cell envelope components of the ancient bacterial cell *Methanospirillum hungatei*. This bacterial organism is important because of its potential for economical methane production and as a candidate to study the evolution of both the archaebacteria and eubacteria [54]. The unusual structural forms of the Mh cells: in addition to their walls, they are surrounded by a paracrystalline sheath in their longitudinal dimension and plugs at their polar ends, reflect the extreme conditions in their evolution. The combination of the plug and sheath layers is thought to produce a differential permeability barrier to nongaseous molecules which can only gain entry to the cellular compartment through the end plugs [57]. Since the functional significance of the sheath and plug is dependent on their orientations, organizations, and detailed molecular structures, characterization of them is an important part of a comprehensive investigation of their properties. Both sheath and plug are well characterized by TEM and diffraction studies. It is interesting to adapt STM, a new technique, to investigate these materials to confirm structures identified by TEM and diffraction studies, to provide complementary information such as thicknesses and three dimensional features, and to reveal new structural details. The plug is a multilaminar structure stacked with morphologically different proteinaceous assemblies. STM study of this structure may provide information about the orientation and stacking arrangement of the plug and finer details of structure which are not revealed by TEM. The S-layer sheath has been studied by STM extensively before. Results showed the sheath is an assembly of hoop-like components, consistent with TEM studies. The surface of each hoop showed a complicated structure of ~3 nm repeats but the evidence for the 2-D crystal structure revealed by diffraction study was not convincing. Some doubts remained as

to whether the observed ~3 nm repeat structure was due to the crystal lattice, due to the metal film used to coat the sheath for STM imaging or due to tip-sample convolution effects. A further study may help us to identify this structural detail and provide clues as to what resolution limit can be obtained on metal coated specimens. Structures of a few nm dimension are subject to both the metal coating and the tip convolution effects, and therefore challenge the STM metal coating technique.

In this investigation, efforts went into the development of fine-grain films and stable and sufficiently sharp tips to increase the imaging resolution. Studies of bacterial cell plugs confirmed the TEM information on morphology and plug dimensions, and in addition provided information about both the thickness of the plug layers and the internal organization of the plug assembly. Studies of S-layer sheathes revealed clearly the ~3 nm x 3 nm lattice structure predicted by diffraction studies. A lateral resolution of ~1 nm was achieved, suggesting that graininess was very small for the Pt/Ir films used, and that the elaborate coating techniques reported by other researchers may not be necessary. Problems encountered in image interpretation are discussed. Possible imaging mechanisms are given to explain observations in which part of the film was removed but the remaining part of the structure was still imaged reproducibly. The possible effect of the tip-sample interaction force on the image is also examined, aiming to understand how the elastic properties of the sample (coated) contribute to the image formation.

2 Theory of scanning tunneling microscopy

2.1 Basic principles

2.1.1 The tunneling current

STM is based on the principle of electron tunneling, one of the main consequences of quantum mechanics. A particle such as an electron, which can be described by a wave function, has a finite probability of entering a classically forbidden region. In the STM the vacuum region between the sample and tip acts as a barrier to electrons. The transmission probability for electron tunneling between infinite, parallel, plane metal electrodes (as in Figure 2.1a) can be easily calculated.

The solutions of Schrodinger's equation inside a rectangular barrier in one dimension have the form

$$\psi \propto \exp(\pm kz) \qquad 2.1$$

where the parameter k is the inverse decay length of the wave function outside the surface and is given by the expression

$$k^2 = \frac{2m[V(z) - \bar{E}]}{\hbar^2} \qquad 2.2$$

here $\bar{E}$ is the electron energy of the state, and V(z) is the potential in the barrier. In general, as shown in Fig 2.1b, V(z) may not be constant across the gap. However, to the first approximation, this potential can be replaced with its average value in the barrier. In the simplest case V(z) is simply the vacuum level; so for states at the Fermi level, $V(z)-\bar{E}$ is just

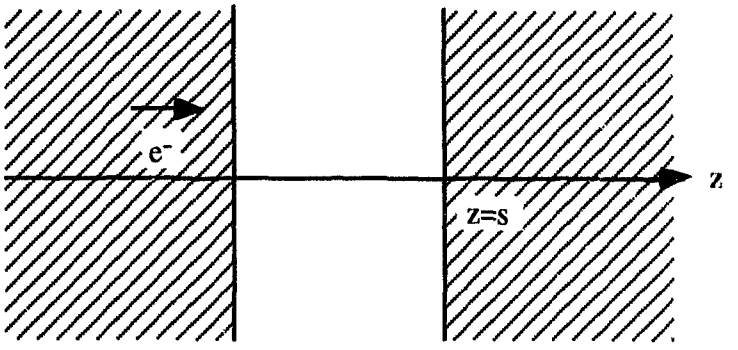

(a)

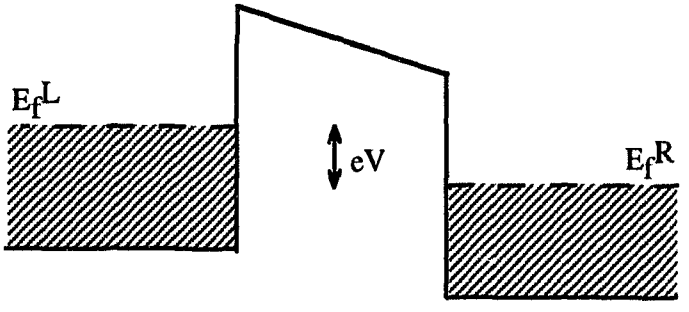

(b)

Figure 2.1a: A planar metal-vacuum-metal junction; 2.1b: Potential barrier between electrodes biased with a voltage V at $T=0^0$ K.

the average work function of the two electrodes.

For tunneling between two metals with a voltage difference V across the gap (Figure 2.1b), only electrons tunneling from states between $E_f(1)$ and $E_f(1)$-V in the left electrode to unoccupied states between $E_f(2)$ and $E_f(2)$+V in the right contribute to the tunneling current. Other states cannot contribute either because there are no electrons to tunnel at higher energy, or because of the exclusion principle at lower energy.

The tunneling current density at the limits of small voltage and temperature can be written as [40]

$$j=\frac{e^2}{\hbar}\frac{k}{4\pi^2 s}V\exp(-2ks) \qquad 2.3$$

The tunneling current through the rectangular barrier around zero bias voltage follows Ohm's law, whereas the dependence on the barrier width is exponential which is responsible for the extreme sensitivity of the tunneling current to the tunneling distance. For a typical work function of 4 eV, we find from Eqn.2.2 that k~1 $Å^{-1}$, thus the tunneling current drops by nearly an order of magnitude for every 1 Å distance change between the electrodes.

2.1.2 Scanning tunneling microscopy

For topographic imaging of the surface, the STM can be operated in the constant current mode or the constant height mode. In the operation of the constant current mode, a feedback loop is used to keep the tunneling current constant while the tip is scanned over the surface, a map of the surface topography can be obtained by recording the z-piezo voltage (Fig. 1.1). In the constant height mode, a tip is scanned across a surface at constant height while the current is monitored. The integrator time constant and the scanning speed are set so that the feedback loop cannot follow the rapid atomic scale changes in tunneling current.

Therefore, only the average value of the current, and the average height of the tip above the surface are maintained. The rapid variations in current, due to the tip passing over surface features such as atoms, are plotted versus scan position. This operation mode is only practicable in cases where the surface is close to atomically flat.

The exponential dependence of the tunneling current on the tip-to-sample spacing has proven to be the key for the high spatial resolution which can be achieved with the STM. Under favourable conditions, a vertical resolution of hundredths of an angstrom and a lateral resolution of about one angstrom can be achieved.

Besides these topographic measurements, the STM can be used to get information about the local tunneling barrier height which is related to the work functions of both electrodes. In this measurement the dI/ds signal derived from the response of the tunneling current I to a fast modulation of the tip-sample distance s is recorded. For the simple case of a one-dimensional rectangular barrier, it is derived easily that the local tunneling barrier height ϕ relates to the dI/ds signal by

$$\phi = \frac{\hbar^2}{8m} (d\ln I/ds)^2 . \qquad 2.4a$$

Therefore the (dI/ds) signal reflects work function-related properties such as chemical composition of the surface material, in the case of ideal tunneling.

Eqn. 2.4a can also be used to estimate the barrier height from the static measurement in which a change in tunneling current dI is produced by changing the reference setting of the feedback circuit and the z-piezo movement ds is measured. A similar relationship between the barrier height ϕ and dV/ds,

$$\phi = \frac{\hbar^2}{8m} (d\ln V/ds)^2 \qquad 2.4b$$

is obtained if the tunneling current is kept constant. This formula is used to estimate barrier height when the bias voltage is varied and the z-piezo movement is measured.

2.2 Theory of the STM imaging

The simple one dimension model outlined above does describe quite accurately the tunneling current between two metal surfaces. It does not, however, account for energy-dependent density of states, which is characteristic for semiconductors and superconductors.

One can calculate directly the transmission coefficient for an electron incident on the vacuum barrier between a surface and tip [41,42]. However, such a calculation is fairly complex for a realistic model of the surface. The tunneling-Hamiltonian formalism [43] based on perturbation theory provides a successful approach to this problem.

2.2.1 Tunneling-Hamiltonian approach

The tunneling-Hamiltonian formalism originally was used by Bardeen [43] to explain the first tunneling spectra obtained by Giaever [44]. Tersoff and Hamann [45] and Baratoff [46] first applied this formalism to STM-related problems. For typical tip-sample separations (of order 9Å nucleus-to-nucleus [47]) the coupling between tip and sample is weak, the electron waves in the two metal electrodes are therefore considered to be independent and the coupling of the electron waves in the gap is treated as a perturbation. The tunneling-Hamiltonian formalism takes into account the detailed electronic states of the electrodes.

In first-order perturbation theory, the current is

$$I=\frac{4\pi^2 e}{h}\sum_{\mu,\nu}\{f(E_\mu)\,[1-f(E_\nu)]-f(E_\nu)\,[1-f(E_\mu)]\}\,|M_{\mu\nu}|^2\delta(E_\nu+V-E_\mu),$$

where f(E) is the Fermi function, V is again the applied voltage, $M_{\mu\nu}$ is the tunneling matrix element between states ψ_μ and ψ_ν of the respective electrodes, and E_μ is the energy of ψ_μ. In the limits of small voltage and temperature, this expression simplifies to

$$I=\frac{4\pi^2}{h}e^2V\sum_{\mu,\nu}|M_{\mu\nu}|^2\delta(E_\mu-E_F)\,\delta(E_\nu-E_F)\,. \qquad 2.6$$

where E_F is the Fermi level. The essential problem is to calculate $M_{\mu\nu}$. Bardeen [43] has shown that

$$M_{\mu\nu}=\frac{h^2}{8\pi^2m}\int dS\cdot(\psi_\mu^*\nabla\psi_\nu-\psi_\nu\nabla\psi_\mu^*)\,, \qquad 2.7$$

where the integral is over any surface lying entirely within the barrier region and separating the two half-spaces.

Tersoff and Hamann [45] used surface electron wave functions with an exponential decay into the vacuum and expanded these wave functions in the generalized plane-wave form. They modelled the tip as if it consisted of a mathematical point source of current, whose position is denoted as $\mathbf{R}_t$. In that case, Eqn. 2.6 for the current at small voltage reduces to [45,48]

$$I\propto\sum_\nu|\psi_\nu(\boldsymbol{R}_t)|^2\,\delta(E_\nu-E_F)=\rho(\boldsymbol{R}_t,E_F)\,. \qquad 2.8$$

Thus the ideal STM would simply measure $\rho(\mathbf{R}_t,E_F)$, the local density of states at E_F (LDOS), i.e., the charge density from states at the Fermi level. Tersoff and Hamann [45] also showed that Eqn. 2.8 remains valid, regardless of tip size, so long as the tunneling matrix elements can be adequately approximated by those for an s-wave function. The tip position $\mathbf{R}_t$ must then be interpreted as the effective center of curvature of the tip, i.e., the origin of the s-

wave which best approximates the tip wave functions.

In this more accurate approach, it is again found that the tunneling junction is ohmic at low voltage (V is in the prefactor) and that the tunneling current depends exponentially on the distance.

From the tunneling-Hamiltonian theory, the recorded image in constant current mode can be interpreted as a contour map of constant LDOS at the Fermi level of the surface. The image interpretation is complicated by the interplay of both geometric and electronic effects to the LDOS. For simple or noble metals, the STM images may be interpreted as reflecting the atomic geometry in a very direct way, while for tunneling to the semiconductors, the image contains both geometrical and electronic information which are usually intermixed in a complex way.

2.2.2 Resolution

Since the tip has a finite radius, the surface topography is determined only with a finite resolution. The lateral resolution of STM, calculated by Tersoff et al. [48] under the assumption of small corrugation, is

$$L_{eff} = [2\,(R+s)\,/k]^{1/2} \qquad 2.9$$

where R is the radius of the tip and s the distance of closest approach between the tip and the surface. The distances are in nm and k in nm^{-1}.

Eqn. 2.9 describes the lateral averaging due to the finite width of the tunneling current filament. With highly corrugated specimens, the point of the tip coming closest to the object can vary during a scan. Thus, the resolution achievable is limited by the tip convolution to the topography of the specimen.

2.3 Tunneling spectroscopy

Tunneling spectroscopy on a local length scale is one of the strengths of STM. The basic tunneling spectrum is the local I-V curve measured by ramping the tunneling voltage and recording the tunneling current at desired locations of the surface while the feedback is not active. Information about the LDOS at the surface can be gathered by analysis of the dependence of the tunneling current on the bias voltage. Because of the difficulty of calculating $I(r_t, V)$ in general, most detailed analyses have focused on I(V), without regard to its detailed tip-position dependence.

STM can also measure spatially-resolved spectroscopy. Alternative to the tunneling current, the local conductivity dI/dV, also a measure of the electronic properties of the sample, as a function of the bias voltage can be measured by modulating the bias voltage and detecting dI/dV with a lock-in. During this measurement, the feedback remains active, but its response frequency is much lower than the modulation frequency so that the feedback maintains only the DC level of the tunneling current. An image produced by recording the dI/dV signals across the surface reveals the variation of sample conductivity.

More comprehensive information concerning electronic properties of the sample is acquired by recording current versus voltage characteristics at each pixel. This technique is referred to as "current imaging tunneling spectroscopy" (CITS) [49]. The feedback is activated only during the time of scan from point to point to adjust the tip-sample distance, and interrupted for the rest of the time to record the current versus voltage characteristic at each particular point.

2.4 Mechanical tip-sample interactions

Ideally, in STM the tip and surface are separated by a vacuum gap, and are

mechanically non-interacting. However the existence of interaction forces between the tip and the surface in the STM had been recognized since the invention of the instrument. The best known examples of the effects of compressive forces are the anomalously large atomic corrugations [50,51], often several times the size expected from the surface local density of states which controls normal STM imaging, and the very low measured values of the tunneling barrier height defined in terms of dlnI/ds [52]. Graphite provides the most widely known example of giant corrugations, but other materials showed similar effects. Combs and Pethica [52] presented a model to explain the often observed anomalously low tunneling barrier heights. They suggested that the tip and sample are in mechanical contact through an oxide or dust particle. Following the earlier suggestion of Coombs and Pethica, Soler et al. [50] attributed the observed amplification of the atomic corrugation of graphite in air to the elastic deformation of the surface under the tip-sample interaction. In their model, they proposed that the deformation results from a force acting locally over atomic distance and the tip and sample are in "physical" contact. A detailed study by Mamin et al. [51] suggests that in fact the interaction is mediated by contamination, consistent with Coombs and Pethica's early proposal. As evidence of this contamination mediated surface deformation, they observed that at very clean UHV conditions measurements apparently give corrugations of at most a small fraction of an Å, consistent with recent theoretical calculations for single-atom tips [53].

The suggestion of the contamination-mediated deformation is that an insulating contaminant (e.g., oxide) acts like a compressed spring which transmits the tip force to the surface. The actual point of tunneling could be a nearby part of the tip which is free of oxide [52], or an asperity protruding through the contamination layer [51]. Once the tip is displaced towards the surface, the compressed contamination layer pushes down the surface, or compresses the tip if it is sufficiently soft. As a result, the surface-tip separation changes a smaller amount than expected from the nominal displacement of the tip, and so the current variation is correspondingly less. The difference is the amount absorbed by the weakest part

of the loop, usually the surface.

The barrier height measurement can be used to estimate the surface deformation. The apparent barrier height, which is often defined in terms of dlnI/ds, will be lower on softer structures than on harder structures, if the effect from difference in work function of the material is much smaller. In our case, the sample is covered with a uniform conductive coating, presumably its surface chemical composition is also uniform, but the local elastic properties vary due to the presence of soft biological structures under the cover. The measured difference in ds over a soft spot and a hard spot is the relative deformation of the soft part with respect to the hard part.

3 Materials and sample preparation

3.1 Materials

Methanospirillum hungatei GP1 grows naturally as linear chains of cells (up to 12 cells long) and it possesses cell envelope components including end plugs and a sheath formed from stacked hoops (Figure 3.1) [54,57].

The tubular sheath is several μm long, about 440 nm in diameter, and 9 nm in wall thickness. Diffraction studies by Stewart et al. [31] suggest that the sheath consists of a two-dimensional crystalline structure on its outer surface with p2 symmetry and a 2.8 nm x 5.7 nm unit cell. The unit cell contains two nearly identical lobes, which means that TEM and STM images of Mh sheath are expected to show a nearly square ~3 nm x 3 nm lattice of lobes. Figure 3.2 is a drawing to show the shape and surface crystalline structure of the sheath. The sheath tends to break into hoops, and dissolution analysis of the material suggested the covalent bonding in the form of strategic disulfide bonds between hoops [55]. Previous STM studies of dehydrated sheath reported by Blackford et al [28] and Beveridge et al. [20] showed linear corrugations running perpendicular to the cylinder axis, corresponding to the stacked-hoop structure. The hoop widths were multiples (4-7 typically) of the expected 3 nm subunit, with deep grooves marking the hoop-hoop boundaries [56]. The P2 lattice structure was not seen by TEM and not seen in those previous STM studies.

The disk shaped plug is extracted from the cell by physical or chemical methods, separated from the sheath by membrane filtration and sucrose gradient sedimentation [57]. Intact plugs can be made to completely dissociate into their component layers by exposure to alkali or detergent at 60^0 C for short periods. TEM work [57] on negatively stained plugs showed the end plug was a multilaminar structure which contained two morphologically different disk-shaped proteinaceous assemblies with a diameter of about 440 nm. Both of

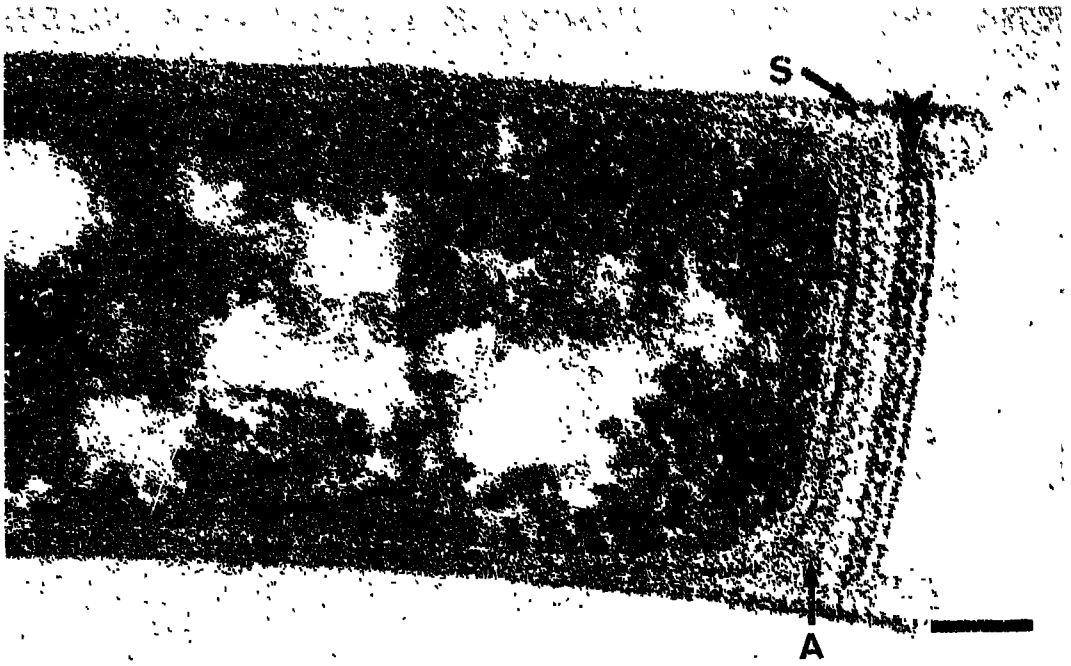

Figure 3.1: A longitudinal TEM thin section through M. hungatei, demonstrating the relationship between the sheath (S), the cell wall (W), the plasma membrane (P), the multilaminar end plug (arrowhead) and the amorphous material (A). Bar is 100 nm.

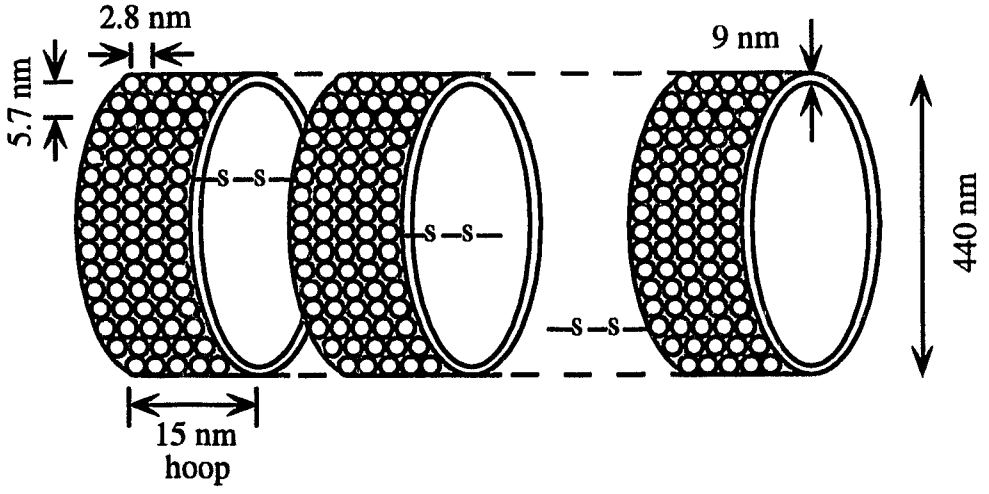

Figure 3.2: Drawing to show the shape and surface crystalline structure of the sheath.

these two individual plug layers possessed 18 nm repeats with different P6 packing arrangements: a particulate layer consisting of circular 14 nm units, and a holey layer consisting of circular 12.5 nm pores. Figure 3.3 is a transmission electron micrograph of negatively stained plug layers showing the particulate and holey layer structures. Computer image reconstruction based on optical diffraction data predicted finer structures on particulate and holey plug layers: each unit particle of the particulate layer is linked to six other particles through six thin arms, which suggests that each unit consists of six subunits; each unit of the holey layer consists of six delta-shaped subunits which are linked to one another by delicate linkers at each tip [57]. These fine structures are not seen by TEM.

The sheath and plug samples were provided by T.J.Beveridge's group at Department of Microbiology, University of Guelph.

3.2 Sample preparation

3.2.1 Substrate

In order to perform STM of metal-coated biological macromolecular structures, we first have to immobilize the structures onto a smooth, stable and conductive substrate. Highly oriented pyrolytic graphite (HOPG) has been widely used as a specimen support, because it is readily cleaved to expose an atomically flat surface over distances of microns, and is conductive. However the adsorption of biological specimens is usually poor on graphite so that they tend to form aggregates on it.

$TaSe_2$ [58] was used as the substrate for protein materials in this study. Besides the advantages HOPG has, such as flat and conductive, the adsorption of the proteins onto $TaSe_2$ was better so that a uniform distribution of biological structures over the surface could be obtained. This is important because the relatively small maximum field of view and the

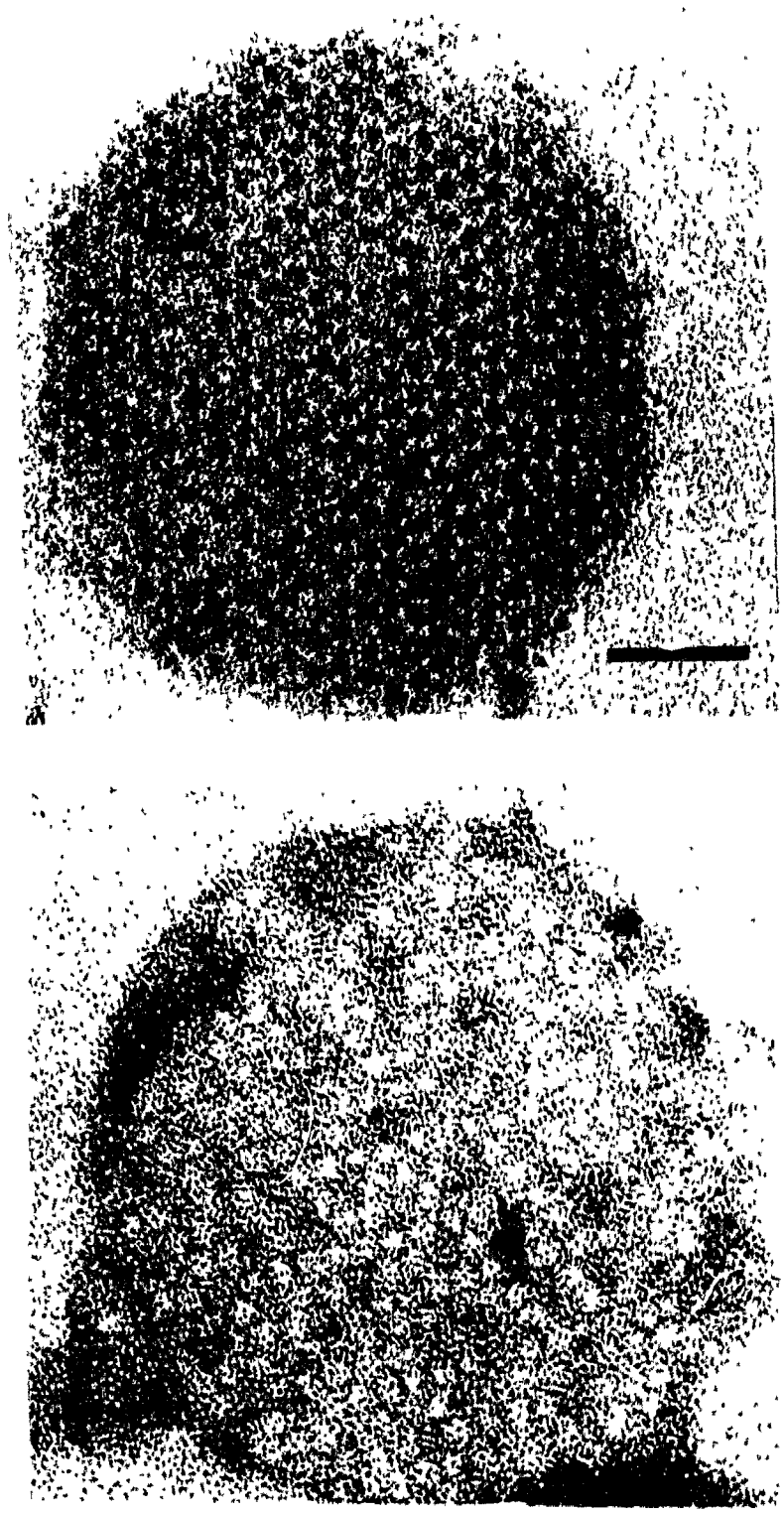

Figure 3.3: TEM negative stain of plug layers. Note the two different types, holey (upper) and particulate (lower), of the paracrystalline assemblies. Bar is 100 nm.

slow scan speed of most STM makes searching for biological objects a tedious task when they are not densely and homogeneously distributed on the support.

3.2.2 Deposition and dehydration of objects

Both sheath and plug materials were deposited on the substrate in the same way. Small drops (2 to 4 μl) of the suspension were applied to freshly cleaved $TaSe_2$ substrates and allowed to dry in air. This simple method for depositing and drying the biological structures onto the substrate is generally effective, although the air-drying process may introduce artifacts which we will discuss later.

Freeze-drying is an established TEM approach to prevent the biological samples from collapsing as the result of the air-drying process. This method was used for plug preparation. In freeze-drying a sample, a drop of solution was deposited on the $TaSe_2$ and left for 15 mins to let the specimens settle on the substrate. The drop was then removed with filter paper and the sample was quickly immersed in liquid nitrogen to be frozen. The sample was quickly transferred from liquid nitrogen to a cold stage in the evaporator. The sample was left to sublime at 1 x 10^{-5} torr pressure at -150 C^0 for about three hours. The cold stage was then warmed up slowly to room temperature and metal coating followed.

3.2.3 Metal coating

Films of 2-3 nm thick Pt or Pt/Ir were deposited from below at 0.5 nm/sec on room temperature samples. Pt or Pt/Ir heated by a tungsten filament was evaporated at a pressure of 10^{-5} torr. The thickness of deposition was measured on a quartz crystal thickness monitor. For the preparation of Pt/Ir/C electrodes, a Pt/Ir cylinder of 1.5 mm diameter and about 1.5 mm long, composed of 30% Pt and 70% Ir was inserted into a carbon rod of diameter of about

2 mm [24]. The evaporation of Pt/Ir/C was carried out by electron beam bombardment in a freeze-etch unit (Balzers) at a pressure of 4×10^{-6} torr. Films of ~2 nm thick were deposited at 0.2 nm/sec on room temperature samples. A high tension of about 1800 V and an emission of about 70 mA were used. The sample rotated during coating, with the source material oriented at 45^0 with respect to the sample. The thickness of the Pt/Ir/C film was monitored by a similar quartz crystal. Since the calibration depends on the Pt-Ir-C composition, which varies in different evaporation and was not determined, the film thickness was estimated with the STM by measurement of the height of a step edge of a Pt/Ir/C film. The step was formed by a removed patch of biological structure.

4 Apparatus and measurement

4.1 The STM

The STM used in this study was designed by B.L.Blackford and M.H Jericho [59]. This microscope utilizes two concentric piezoelectric tubes; an inner scanning tube which moves the tunneling tip across the sample surface and controls the tip-sample separation, and an outer positioning tube which provides for inertial translation of the sample into tunneling range. Home built electronics and an Atari computer provided the electronic controls of this system and data acquisition.

4.1.1 Mechanical structure

(a) Micropositioner

Figure 4.1 shows the principle of operation for coarse sample positioning. Two parallel quartz rods are secured to the end of the outer piezoelectric tube, forming a horizontal longitudinal track. The sample holder is a slider rod resting on the track. By applying a cycloidal waveform [60] between the inner and outer electrodes, the piezo tube [61] expands slowly and then retracts quickly in the longitudinal direction, making the sample holder slide in or out by the inertia-type motion. The outer electrode is split into a right and left sector, thus, by applying voltages of the same amplitude but opposite sign to the two electrodes to activate the bending mode of the piezo tube, the transverse motion of the sample can be produced by inertia-type rotation of the sample holder in the track. This gives the ability to move the sample transversely in a few tens to a few hundreds of nm steps, which is very useful for searching the sample for biological specimens.

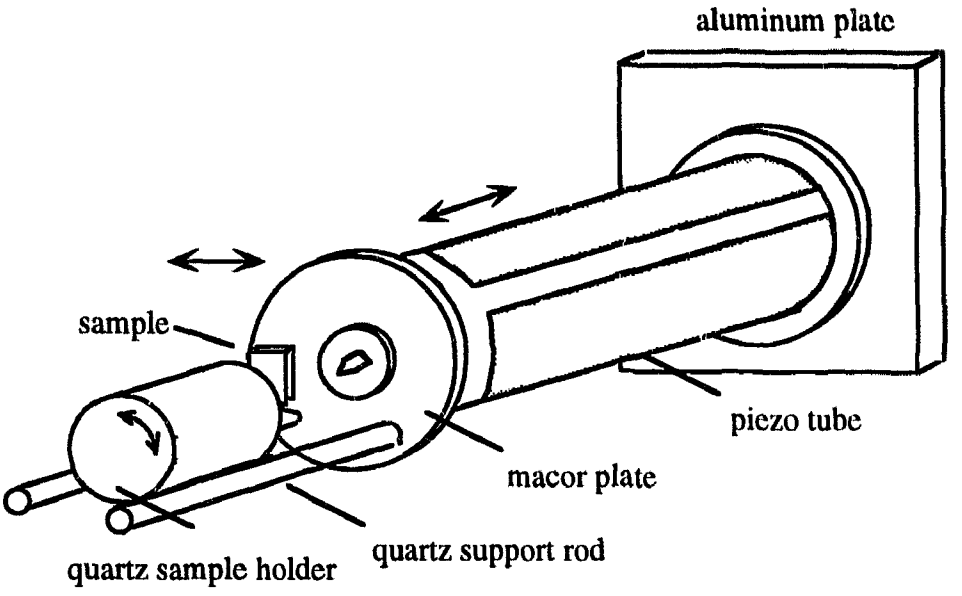

Figure 4.1: Schematic of the two dimensional micropositioner.

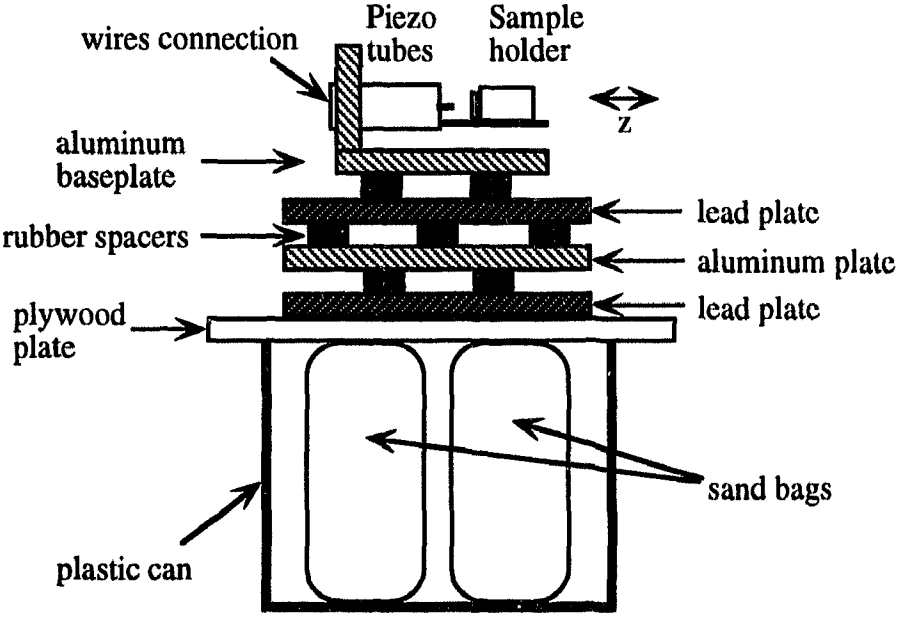

Figure 4.2: Diagram of the vibration isolation system.

(b) Scanner

The scanning tube which is arranged inside the concentric positioning tube is the device that moves the tunneling tip across the sample surface and controls the tip-sample separation [Figure 4.3]. In order to get three orthogonal displacements, the tube has the outside electrodes split into two sections with equal length along the longitudinal dimension. One of them serves as the z-motion drive and the other which is further segmented in four equal sectors of 90° serves as the xy scan drive. The inner wall electrode is grounded. By applying mirror symmetric driving signals across two diagonally opposite electrodes of the xy drive, the tube is bent perpendicular to its axis, producing lateral motion. The linearity of the scan is improved by using these + and - electrodes. By applying voltage with the appropriate sign to the z electrode, the tube expands and contracts, producing vertical z motion. The tip is mounted in the end of the tube near the z-piezo side. The sensitivities are 50 Å/V in z and 200 Å/V in x and y. A small coaxially shielded lead runs from the tip to the input of the I/V converter preamp (~15 cm distance).

The scanning tube is about 25 mm long and 9 mm in diameter, while the outside coarse positioning tube is the same length and about 13 mm in diameter. Both tubes have a wall thickness of 0.5 mm.

(c) Vibration isolation

Considering the resolution and sensitivity of STM, the maintenance of a vibration free environment is essential to the proper operation of the STM. The vibration isolation for our STM was obtained with a stacked metal plate system (Figure 4.2). First, the 12 mm thick aluminum baseplate of the unit is mounted on top of a 25 mm thick lead plate, separated by rubber spacers, then on another 12 mm thick aluminum plate and 25 mm thick lead plate, also

separated by rubber spacers. This combination is housed in a sheet metal box resting on a plywood plate. The latter rests on top of 4 20-kg sand bags piled in a plastic can. A PVC plastic cover box (10 mm thick) over the whole system isolates against acoustic vibrations in the air. Vibration propagating along the electrical wires connecting the tunneling area to outside electronics are prevented by using thin wires and by clamping them on the intermediate stages. We found that the compactness and the rigidity of this microscope design can tolerant a even less perfect vibration isolation system.

4.1.2 Electronics and data acquisition

Figure 4.3 shows a block schematic of the electronics used for controlling the tip-to-sample spacing of the STM, tunneling current, scanning movements and data acquisition. A detailed circuit of the preamplifier and feedback amplifiers is shown is Figure 4.4.

The sample is held at a fixed bias voltage produced by the sample bias circuitry. The tip is connected to a current-to-voltage converter (I/V converter) with a sensitivity of 0.01 V/nA. The output of the I/V converter is fed into an absolute value circuit which is used to maintain negative feedback conditions when the sample bias is reversed. The logarithmic amplifier is used to linearize the exponential dependence of current on tunneling distance, eqn 2.3, which improves the stability of the feedback system. The tunneling current is set by the reference adjust of the log amplifier. Proportional feedback was also used sometimes to improve the response time. The output signal was then integrated and amplified (High voltage amplifier for Z, not shown in Fig. 4.4), and supplied to the z-piezoelectric tube for adjusting the tunneling gap spacing (constant current mode operation).

The computer interface system generates a raster scan via digital-to-analog convertors and reads the z-data with an analog-to-digital converter. High-voltage amplifiers [62] are used to achieve large scale scans. The z piezo voltage or the tunneling current is recorded as

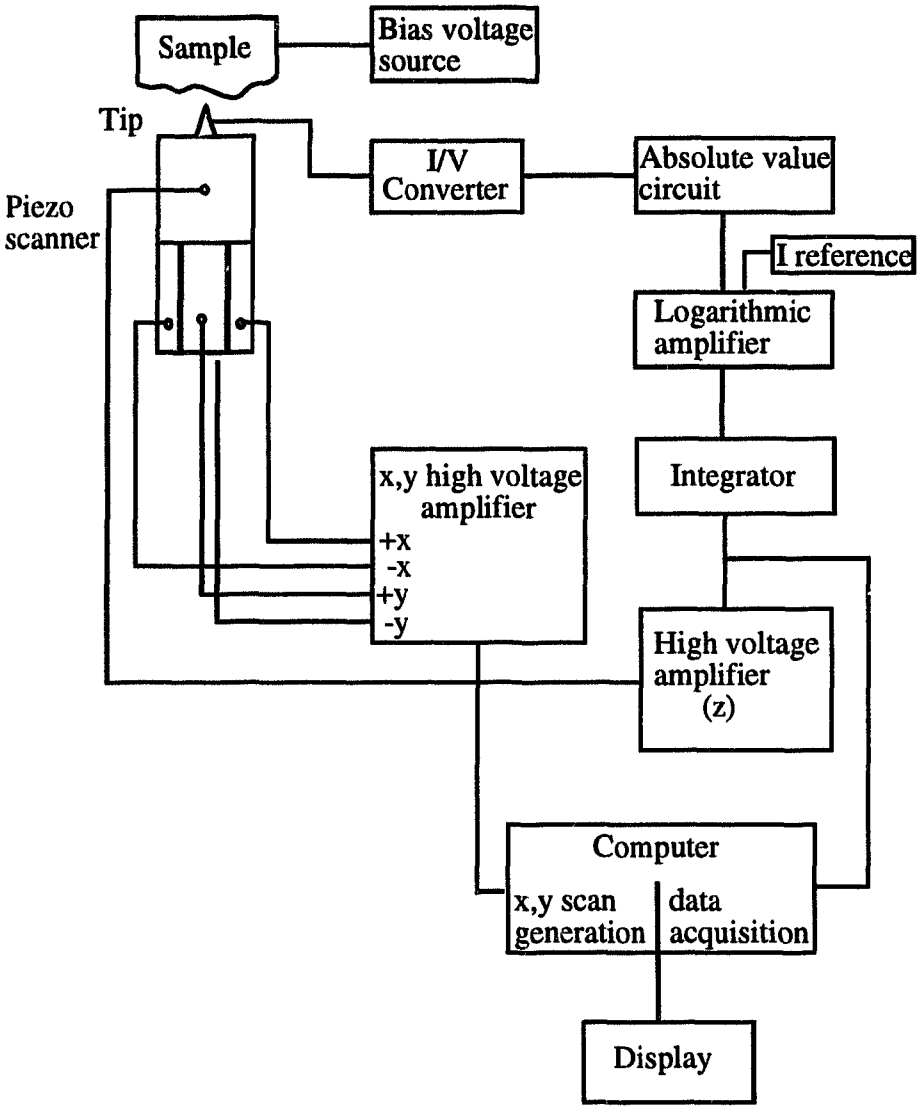

Figure 4.3: Block schematic of the electronics of STM.

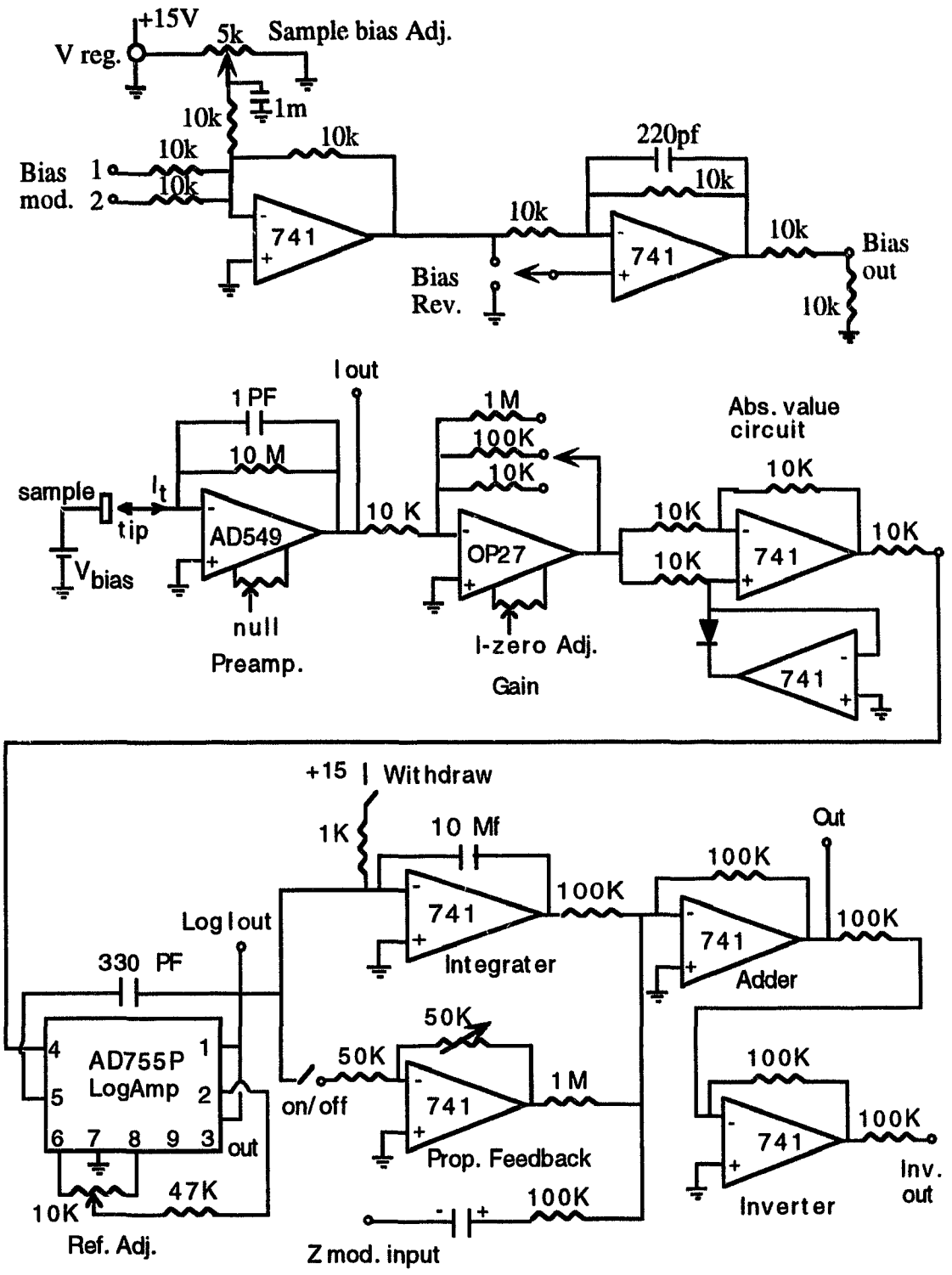

Figure4.4: Schematic of the sample bias adjustment and the tip position control feedback circuitry.

the signal, depending on whether the constant current mode or the constant height mode is used. The x,y and z voltages, when translated into distances, define a picture or image of the surface.

4.2 Tunneling tips

The properties of the tip are decisive for the quality of the STM images. For imaging atomically flat samples only the apex atoms of the tip contribute to the tunneling current and therefore are relevant. For imaging highly corrugated samples like biological specimens, however, the point of the tip coming closest to the object can vary during a scan. The geometry of the tip is thus convoluted to the topography. A good image, which represents the true structure of the surface, requires a tip which is ideally sharp at its end and has an aspect ratio (ratio of the length to the width of the tip) larger than the corrugation of the surface structure. The tip should be mechanically and chemically stable and have a good conductivity.

Three types of tips were used in this study: commercial electrochemically etched Pt/Ir tips [63], mechanically cut Pt/Ir tips, and electrochemically etched tungsten tips. Pt/Ir tips are free of oxidization in air and therefore are advantageous for the stability of tunneling in air. Figure 4.5 is a TEM image of a commercial Pt/Ir tip showing the tip to have a radius of ~50 nm. This type of tip provided stable and high resolution (resolved the ~18 nm lattice structure of the plug) images of biological specimens. However the insufficient sharpness could have limited the imaging resolution as I will discuss in the later chapter. Cutting Pt/Ir wires at a $\sim 45^0$ with a scissors can produce tips which are as sharp as the commercial ones, but this simple cutting procedure often produces multiple tips, which could cause multiple images of structures. Mechanically cut tips are therefore not suitable for imaging biological materials.

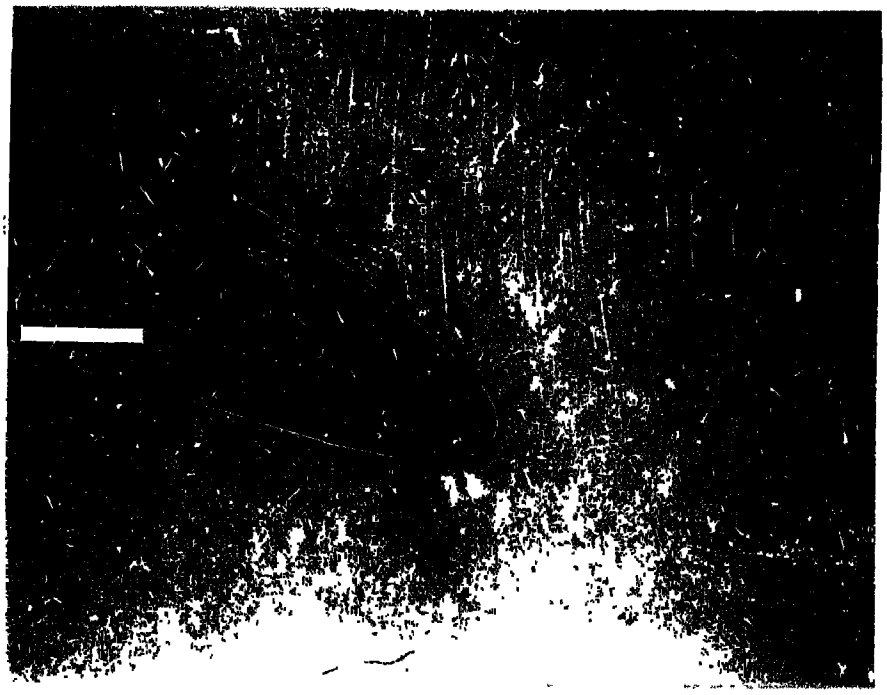

Figure 4.5: TEM image of a commercial Pt/Ir tip. Bar is 200 nm.

Figure 4.6: TEM image of an etched w tip, made as part of this study. Bar is 100 nm.

The tungsten tips used were etched in NaOH following the procedure described by Hacker et al. [64]. The procedure is similar to that of the conventional dc etching except that the lower part of the wire, which is wax coated, is collected as the tunneling tip. The tip geometries were assessed in a TEM. Figure 4.6 is an example TEM image of these etched W tips. The tip ends were ~8 nm in radius, with high aspect ratio of >1. These tips are significantly sharper and narrower than the commercial ones (Fig. 4.5). Using these tips, we resolved the two dimensional ~3 nm x 3 nm lattice structure of the S-layer sheath of the Mh, with a lateral resolution of ~1 nm.

4.3 Measurement

Imaging was performed at room temperature under atmospheric conditions with the STM operating in the constant current mode. The bias voltage and tunneling current were about 0.2 V and 0.2 nA, respectively, giving a gap resistance of 1 GΩ which was essential for non destructive imaging. The scan speed ranged from 100 to 1000 nm/sec. A typical image consisted of 128 scan lines with 256 points per line.

The local barrier height measurements were performed by quickly varying the bias voltage and measuring the change in the z-piezo voltage (this gives the change in tip-sample separation). According to Eqn. 2.4b, switching the bias voltage from V_b to $2V_b$, for example, the apparent barrier height can be calculated by

$$\phi_a=(\Delta \ln V/\Delta \ln s)^2_I=(0.693/\Delta s)^2.$$

where Δs is the measured change in tip-sample separation. The constant $\hbar^2/8m$ is ~1 when s is expressed in Å and ϕ in eV.

5 Results and discussion

5.1 Characterization of structures and comparison with TEM and diffraction results

5.1.1 The end plug

Figure 5.1 shows a Pt-Ir coated end plug about 18 nm high and 350 nm in diameter with a particulate surface. The STM image confirmed the two-dimensional pattern on the surface previously seen by TEM, and also directly measured the plug thickness.

The top plug layers shown in Figures 5.2a, b, and c show three different plug structures: the particulate, holey, and amorphous layers, also seen by TEM. The plugs were 12 nm, 18 nm, and 15 nm, thick respectively. The P6 symmetry with a lattice constant of 18 nm is readily resolvable and the two different arrangements of protein array are distinguishable from each other. However, the sizes of the particles and pores are difficult to determine because they were probably distorted by the tip geometry, via the well known tip convolution effects.

Identifying the relationship between the thickness of the specimen and the topology of its exposed surface provides a means of determining the natural internal organization of whole plugs. The minimum height for an exposed plug structure was ~6 nm (Figure 5.3), which probably corresponded to the thickness of a single plug layer. Experimental data also showed plugs of up to 30 nm, indicating multiple component layers. Each whole plug consisted of at least four single layer elements plus the amorphous material, and these layers were stacked as two particulate layers together and two holey layers together. This agrees with the recent analysis of TEM results [65], and disagrees with the previously suggested [57] particulate-holey-particulate layer sandwich structure.

The identical P6 symmetries of each layer within a plug suggested they align in

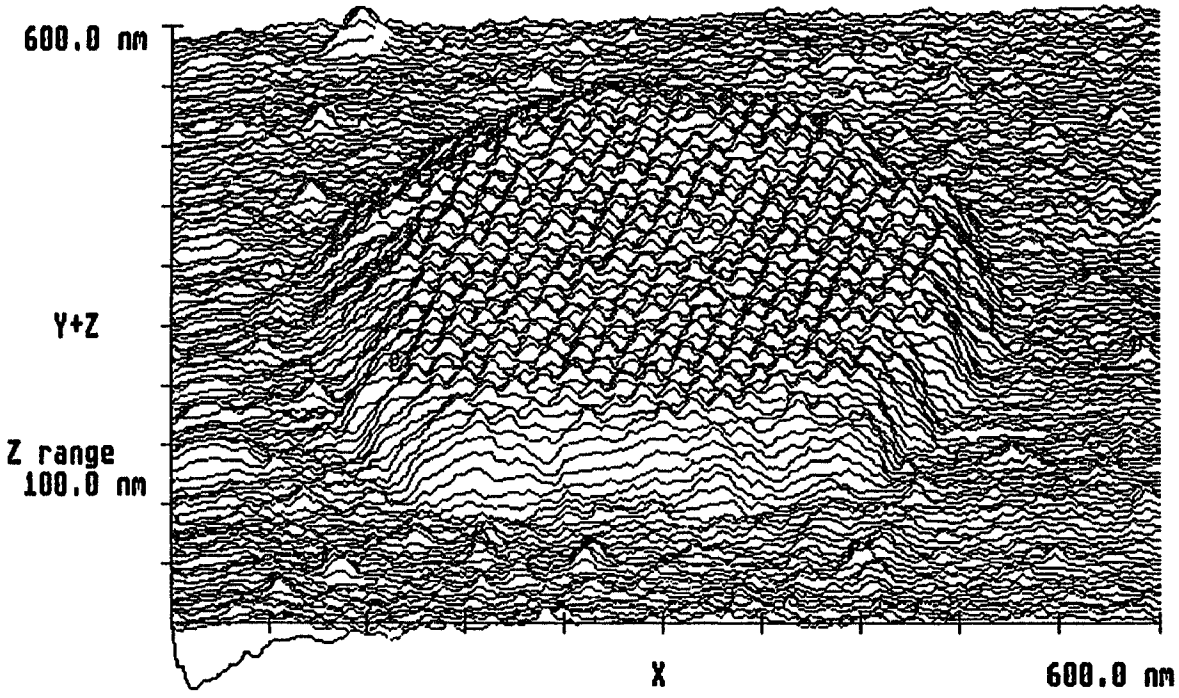

Figure 5.1: A raw data line scan STM image of a Pt/Ir coated plug showing the particulate nature of its surface and the height. The x scan distance is displayed horizontally and y+z is displayed vertically. The z-range is 100 nm full scale.

Figure 5.2a: Height shaded image of a 12 nm thick plug layer with a particulate surface. Bar is 100 nm.

Figure 5.2b: Height shaded image of a 18 nm thick plug layer with a holey surface. Bar is 100 nm.

Figure 5.5: A raw data line scan STM image of a Pt/Ir coated Mh sheath fragment.

Figure 5.6: High resolution, slope shaded image showing the 2-D 3 nm x 3 nm lattice structure. Bar: x,y, 10 nm; z, 1 nm. The 3 nm lobes are ~0.1 nm high.

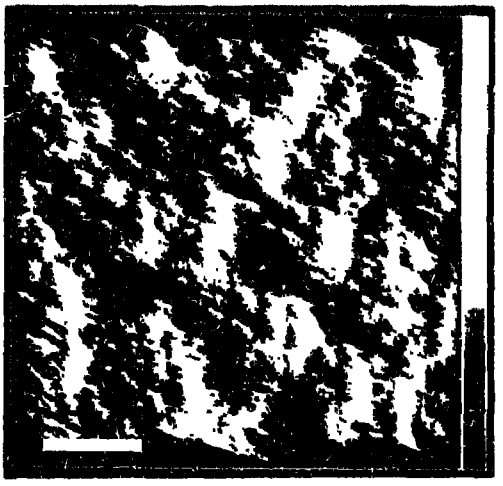

Figure 5.7: High resolution image showing the hoop structure consisting of 10-15 nm wide bands running up to the right. Bar: x,y, 10 nm; z, 1 nm.

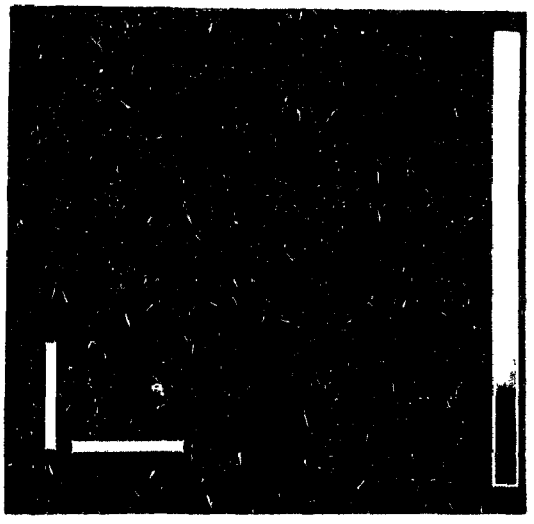

Figure 5.8: Cross-section running parallel to the 3 nm corrugations, and perpendicular to the hoop bands, in Figs. 5.6 and 5.7. Shows the hoop bands to be slightly tilted, giving a shingled appearance to the surface. Bar: x, 15 nm: z, 0.5 nm.

Figure 5.2c: Height shaded image of a 15 nm thick plug layer with a particulate layer obscured by the amorphous matrix. Bar is 100 nm.

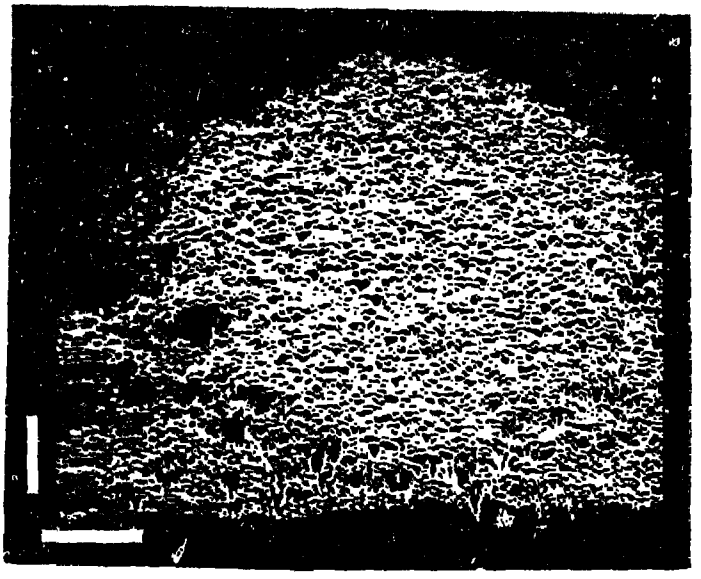

Figure 5.3: A raw data line scan image of a single layer plug (~6 nm thick). Bar: x,y, 100 nm, z, 20 nm.

register to one another. TEM has difficulty ascertaining the exact alignment of this register, e.g., whether the alignment has (1) the particles of one particulate layer lying against particles of another, or (2) the particles fit into and partially occupy the holes of another particulate layer. STM images showing stacking of incomplete layers support the former, node to node register alignment. Fig. 5.2a is direct evidence for this alignment between the two particulate layers, while Fig. 5.2b shows a similar alignment between the two holey layers. In Fig. 5.2a the six units on top appeared larger than those in the lower layer, which indicated a tip broadening effect. I have not yet seen any images that show the alignment between particulate and holey layers.

The height of plugs with respect to the background was interpreted as their thickness. Similar thickness values were obtained for Pt and Pt/Ir coated samples prepared with both air dried and freeze dried plugs, and on both $TaSe_2$ and HOPG substrates. Figure 5.4a and 5.4b are high magnification images of the plugs presented in Fig. 5.2a and 5.2b, respectively. The Pt/Ir coated plug (Fig. 5.4b) showed ~3nm size structures. These may be structures corresponding to molecular folding, or just grains of the Pt/Ir coating. Smoother films were seen on samples with Pt/Ir/C coating (Fig. 5.4a) than with Pt/Ir coating (Fig. 5.4b). The ~3nm size structures seen on Pt/Ir coated plugs may be due to the coating material rather than the molecular structure itself. STM studies have not confirmed those finer details of the plug, which were shown on computer reconstructed images based on optical diffraction data [57].

The images of plugs presented in Figs. 5.1, 5.2, 5.3 and 5.4 were obtained with commercial Pt/Ir tips.

5.1.2 The S-layer sheath

The S-layer sheath has been extensively studied by STM and AFM before [27,28,33,56]. Images showed linear corrugations running perpendicular to the cylinder axis,

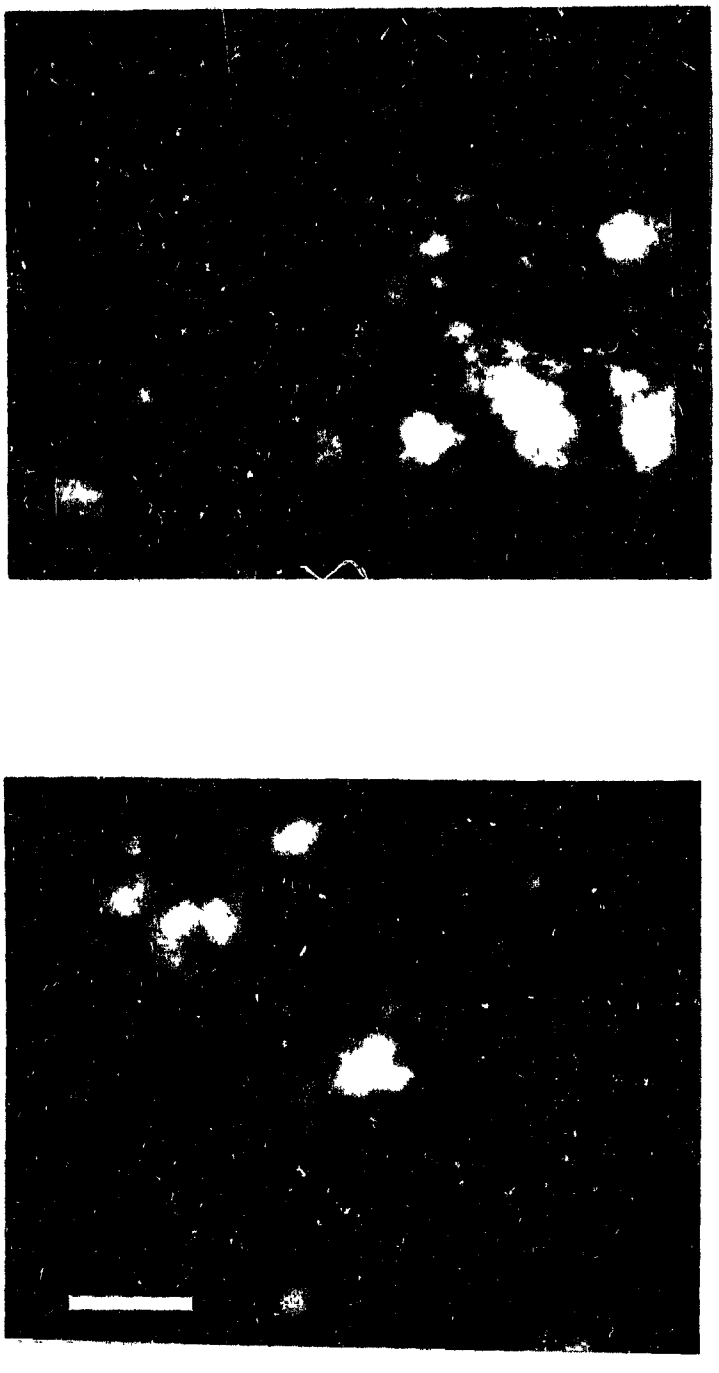

a

b

Figure 5.4: High resolution, height shaded images of the plugs presented in Fig. 5.2a and 5.2b, respectively. (a) is Pt/Ir/C coated; (b) is Pt/Ir coated, showing the ~3 nm structures. Bar is 20 nm.

corresponding to the stacked-hoop structure. The hoop widths were multiples (4-7 typically) of the expected 3 nm subunit, with deep grooves marking the hoop-hoop boundaries [56]. The surface of each hoop showed a complicated structure of ~ 3 nm repeats but the evidence for the 2-D crystal structure was not totally convincing. Some doubts remained as to the origin of the observed ~3 nm repeat structure. Here I present our new results about the nanoscale details of the sheath structure.

Figure 5.5 shows a low resolution, raw data image of a Pt/Ir coated sheath fragment having dimensions ~300 nm wide x 600 nm long x 9 nm thick. The sheath is folded over on itself in the top portion of the figure. The high resolution images presented in Figs.5.6, 5.7 and 5.8 below were taken on top of this fragment in the smoothest region just below the fold. It is not known for certain whether this surface corresponds to the inner or outer surface of a complete sheath [20], but it is thought to be an inner surface, because the relatively deep hoop boundaries which normally appear on the outer surface are not present on this image. Note that the surface of the folded portion is considerably rougher, similar to the background roughness.

Figure 5.6 is a high resolution image viewed at 5^0 to the normal and slope shaded to accentuate the fine structure. It clearly shows corrugations, separated by ~3 nm, running upwards to the left and having lobes spaced at ~3 nm intervals along the corrugations. We interpret this as direct evidence for the 3 nm x 3 nm lobe structure expected from diffraction studies. Note that the corrugations in Figure 5.6 run parallel to the fold in Figure 5.5, which we assume to be parallel to the axis of the sheath.

Figure 5.7 is a higher resolution image of a different area than Fig. 5.6, which shows again the 3 nm x 3 nm lobe structure. It also shows that the corrugations are not continuous but are interrupted by a band structure running perpendicular to them, upwards to the right. These bands are interpreted as due to the hoop structure of the sheath. The figures show that the widths of the hoop are such as to contain ~3 to 5 of the 3 nm lobes, which is consistent

with previous STM studies [56]. Fig. 5.7 also shows that the hoops are slightly tilted giving the appearance of a shingled surface, as shown exaggerated in a line scan running parallel to the 3 nm corrugations, Figure 5.8.

5.2 Discussion on image resolution and interpretation

Considerable care is needed to interpret STM image detail because of the existence of the perturbing effects such as film roughness and tip convolution. Techniques [66] were developed to determine the extent of tip artifacts. However, quantitative restoration of STM data requires extensive numeric calculations on computers, taking into account detailed properties of sample and tip. In this section, a detailed discussion is given on facts which affect the image interpretation and limit the resolution.

5.2.1 Effect of the coating film

Coatings may obscure fine structure and thereby limit the resolution. Furthermore, the grain size of the metal coating may cause misinterpretation of structures with dimensions similar to that of the grains. Investigations on materials and evaporation methods were carried out in efforts to find fine grain films and obtain good contrast of underlying biological structures.

Among the materials used for coating, Pt and Pt/Ir coatings showed 2-3 nm grains. These coatings provided high resolution and contrast (vertical resolution) images, while no noticeable difference between the two coatings was observed. Pt/Ir/C films prepared by electron beam evaporation method were much smoother than Pt/Ir films, they were virtually grainless. The ~3 nm size structure which appeared on both Pt and Pt/Ir coated plugs were not present on Pt/Ir/C coated plugs. The ~3 nm size structures may be due to the Pt and Pt/Ir

coating material rather than the molecular structure itself, however the structures may also be a result of Pt/Ir material preferentially depositing on certain protein structures. For resolving structure detail in nm size range, the effect of decoration might become significant. The fact that the 3 nm x 3 nm structure that corresponds to the known underlying crystalline lattice of sheath was found on Pt/Ir coated sheath suggests that the grains size of the Pt/Ir film was much less than for similar films deposited on a smooth metal surface (~3 nm), or that the Pt/Ir grains attached preferentially to certain proteins on the sheath. Since the ~3 nm structure on Pt and Pt/Ir coated plugs appeared almost unregulated, it most likely refers to the nature of the coating film instead of the plug structure. It is also possible that the tip convolution effect gave the appearance of this unregulated ~3 nm structure, since the 3 nm x 3 nm 2-D structure of sheath was observed with a sharper (radius of ~8 nm) W tip. Plugs were not studied with the super-sharp W tips.

We found that Pt/Ir/C coated samples can be stored without degradation for much longer than Pt and Pt/Ir coated samples. Wepf et.al [24] also noted the advantage of Pt/Ir/C over other conventional high-resolution shadowing materials in keeping structures exposed to atmospheric conditions.

As it has been realized, the specimen temperature may be almost as significant as the coating material. Two facts probably contribute to the increased resolution with lowered specimen temperature. Firstly, molecular motion on the specimen itself is reduced; secondly, mobility of the incident atoms might be reduced since kinetic energy is absorbed more quickly by the colder surface, and the atoms are more likely to stick where they first land. I tried to lower the specimen temperature to that of LN for Pt/Ir coating, and did find the influence of the temperature on the structure detail revealed by STM imaging. Figure 5.9 is a high magnification image of a plug coated with ~2 nm thick Pt/Ir film at a low temperature of -160°C. A fine structure on the 18 nm spacing units appeared different than those of room temperature coated plugs (Fig 5.4b). It is arranged more regularly, almost as a periodic

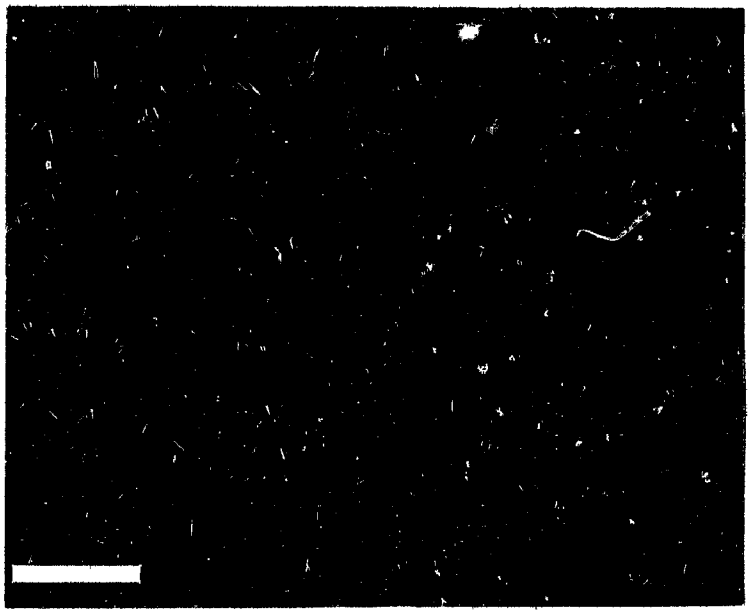

Figure 5.9: High resolution image of a particulate plug coated with Pt/Ir film at -160°c.

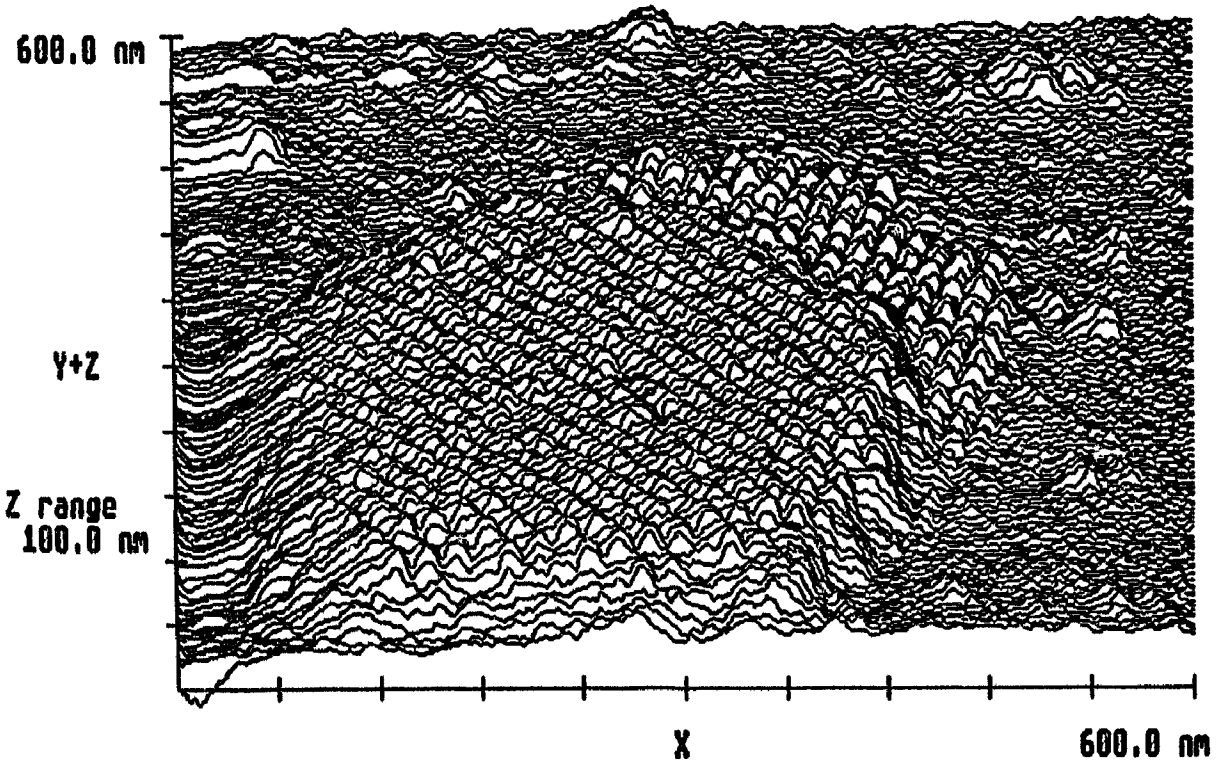

Figure 5.10: A line scan image of the same plug recorded in Fig. 5.1. A second microtip was developed after a few scans.

structure (seven molecules arranged as close packed). It is possible that the atoms of the coating material had preferentially attached to certain sites on the protein structure at low temperature, or the lower temperature reduced the molecular motion and therefore stabilized the structure. However, we can not exclude the possibility of effect of the grains. Comparingthe grains of the film on the substrate and on the biological materials provides a clue to clear these uncertainties about the fine structure. However the grains on the proteins are usually different from those on the substrate, presumably due to different interaction between the substrate atoms and the adatoms. We can not draw conclusion on this fine structure of the plug at this stage.

Pt/Ir/C coatings were well suited for STM imaging when applied to freeze-dried T4 polyheads and HPI-layer. We have yet to test this on plugs and sheaths. Instead, we tested Pt/Ir coatings on freeze-dried plug samples, using the procedure described by Amrein and Gross [67]. No obvious differences in structural details and in film roughness were detected on samples prepared by freeze-drying and air-drying methods. This suggests that the effect of possible artifacts of the air-drying process was small.

Many other materials which were tried did not provide good coatings for biological samples, but may still be worth mentioning here. Gold forms large grains, and the coalescence of the islands happens at about 5 nm, much thicker than Pt and Pt/Ir which is below 2 nm. The deposition of a good quality film requires the substrate to be clean and preferably a single crystal. It was found that coalesce of islands happened later on sites with biological deposition than on an uncovered $TaSe_2$ substrate. Gold evaporated at low temperature forms very smooth films on crystal surfaces as reported by Jaklevic et al. [68]. When applied to biological samples, it also formed a smooth film, however, it tended to smear the underlying structure. Furthermore, the film still needs to be 4-5 nm thick to provide enough conductivity for STM imaging at normal imaging conditions. Gold, which is very diffusive, is therefore less suitable for coating biological samples. Cr films deposited by subliming gives even larger (~30 nm)

and less corrugated grains. A film of 2 nm thick covered biological structures uniformly and thereby provided sufficient conductivity. However the structures were also blurred under the coating.

I should also mention here that, the film roughness and tip convolution interplay to the image formation. An apparent smooth film or structure can be a result of a blunt tip. No conclusion can be drawn before consistent results are obtained.

5.2.2 Effect of the tip convolution artifacts

With highly corrugated surfaces like biological specimens, the point of the tip which dominates the tunneling current can vary during a scan. Thus, the geometry of the tip is convoluted into the topographic image of the sample.

Typical tip problems in imaging biological structures are:

(1) edges of structures are broadened by the tip.

(2) the large tip angle prevents the imaging of bottoms of ditches and holes.

(3) sharp features on the sample image the tip.

(4) multiple tip effect, the object is imaged several times.

For highly corrugated specimens, the best images will be obtained with a tip which is ideally sharp and has an aspect ratio larger than that of the specimen structure. The tip also must be mechanically stable.

The commercially prepared Pt/Ir tips have provided us stable and reproducible images of the plugs with high resolution. TEM revealed the radius of the tip is about 50 nm. A tip of this size allowed us to register the pattern of the 18 nm periodic structure on plugs, although the size and depth of this structure are not reliably indicated by the image. It is also possible that the actual tip was much sharper than 50 nm, which therefore resulted in high image resolution. Microtips can develop during a scan. This might be the reason that we

don't see the high resolution images often. The insufficiently sharp tip could have prevented us from seeing the ~3 nm x 3 nm lattice of the sheath and the finer structure on the plug. The tungsten tips etched following the procedure described by Hacker et al. [64] were much sharper (radius < 8 nm) and longer (aspect ratio >1) than the commercially prepared tips. Imaging with these tips resolved the ~3 nm x 3 nm lattice structure of sheath, with a lateral resolution of ~ 1 nm. These tips were not tested on Plugs.

Tips which proved to be not good enough when tested by imaging can be improved by applying voltage pulses [67] in addition to the tunneling voltage during scanning or local tunneling. Sharpening the commercial Pt/Ir tips was attempted by using this pulse method. Typical pulses were 5-7 V high and 100 micro sec long. The image resolution was increased in some cases which can be explained by the tip being reshaped to a sharper end due to the pulse. This treatment is not well controlled, therefore we don't know what to expect after the pulse. There is a risk of producing blunt tips or most often multiple tips.

It is also possible that the tip changes its performance during scanning. Figure 5.10 is an image of a plug collected right after Fig. 5.1. A second microtip was developed during scanning. The plug was imaged twice and the second microtip appeared sharper than the first one.

Information about tip convolution effects may be obtained from careful interpretation of topographic images. Repeating features showing the same orientation in an STM image are suspected to be due to a tip problem unless there are good reasons to expect such a uniform orientation.

Figure 5.11 is an image of a Pt/Ir coated plug imaged by a mechanically cut Pt/Ir tip. A question arises as to whether this is a plug with two layers shifted relative to each other or due to a double tip effect. The answer is important to biologists, they can draw completely different conclusions to the internal organization of plugs. If it is a two layer plug, both layers are a particulate layer, then the previously predicted sandwich structure should be

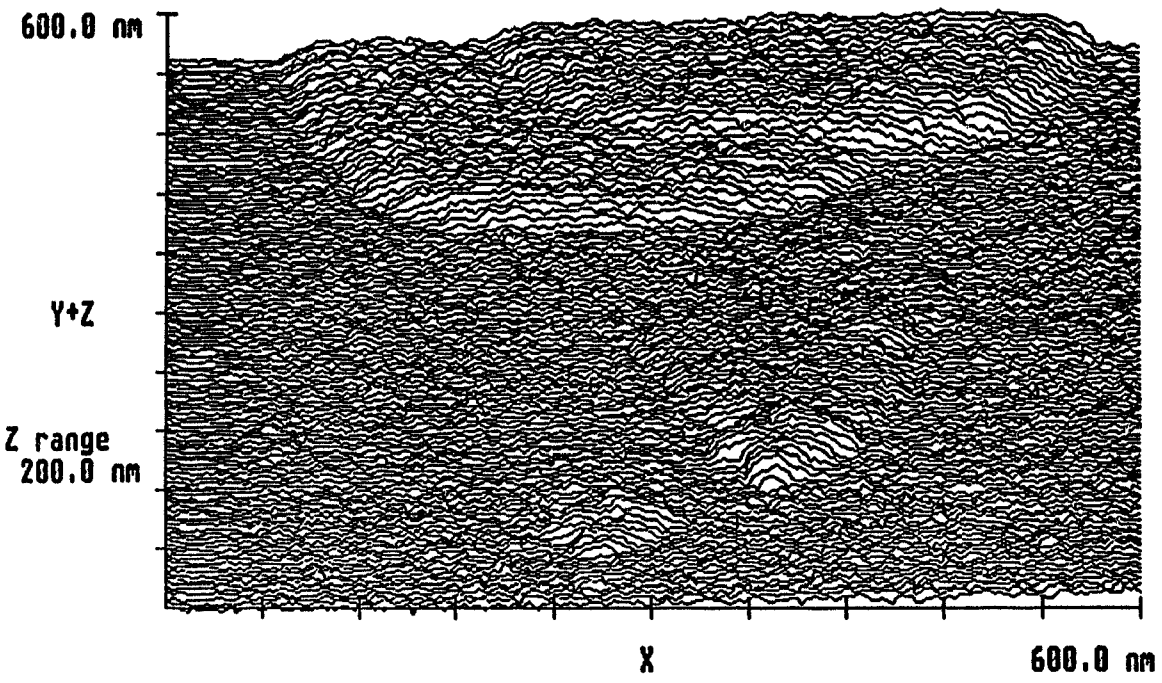

Figure 5.11: STM image of a plug showing a double tip effect.

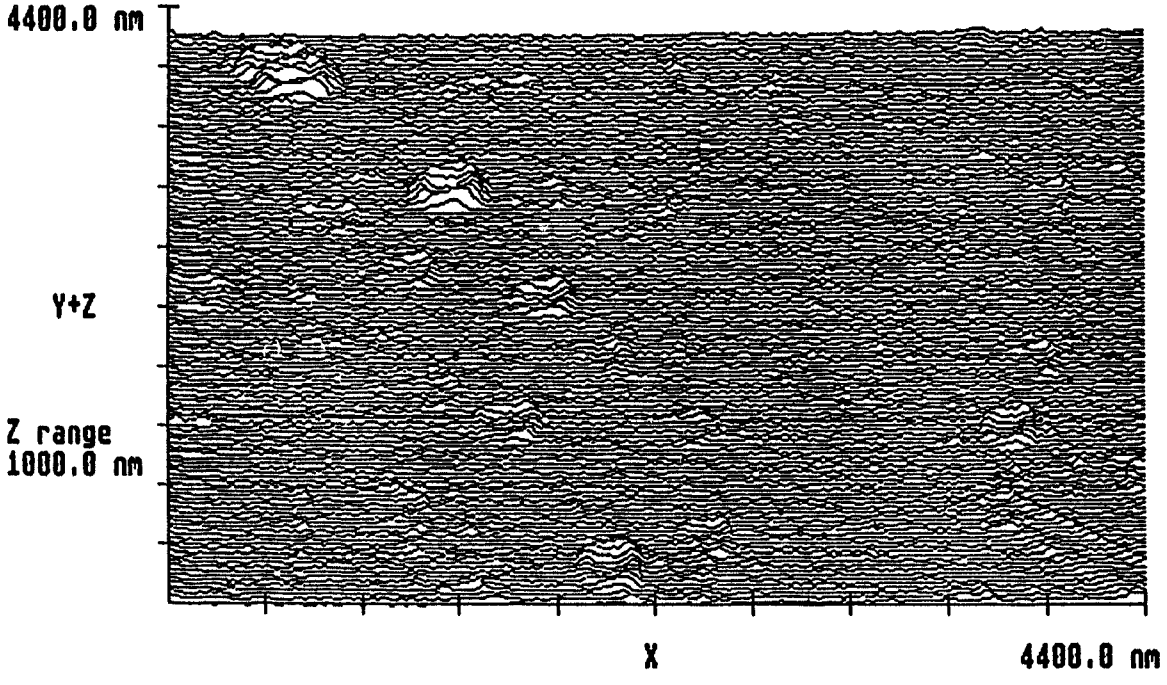

Figure 5.12: STM image showing repeating images of the tip produced by sharp features on the surface.

excluded. We interpret this image as a single layer plug but imaged twice by micro-tips instead of two layers shifted relative to each other. This is evidenced by the fact that the adjacent object was also imaged twice and the distance between the two objects is the same as that between the two plug layers, and the difference in height between the two objects is also the same as that between the two plug layers. Objects with height smaller than the difference in height of the two tips are not subjected to this double tip effect.

Figure 5.12 is another example of tip artifacts. Every sharp feature on the sample gives an image of the tip resulting in multiple features of the same size and orientation all over the STM image, representing the shape of the STM tip.

Since there is no direct way to test the condition of a tip other than by analyzing the images, any inference about the structure requires a careful analysis of the image to identify and account for the distortions. There has been some recent work [66] that has used information contained in the image to place an upper bound on the tip radius. In our study, however, the radius of the tip, the grains of the coating and the structural details we are interested all fall in the range of a few nm, and this increased the difficulties in analyzing the data. Other independent techniques may be necessary to confirm some structural details.

5.2.3 Effect of tip-sample interaction forces

An additional possible imaging problem associated with STM measurement of biological samples is the deformation of the sample under the force of the tip.

The STM tip force can not be ignored even when imaging metal coated biological specimens. The best possible resolution is obtained with thin coating, but such films are very delicate. Substantial plastic deformation occurred when the gap resistance was reduced to ~200 MΩ. We found that a minimum of ~1 GΩ gap resistance was needed for stable and reproducible imaging of plugs covered by a ~2 nm Pt/Ir coating. Even at such a gap

resistance, tip induced displacement or damage was not uncommon. Figure 5.13 is an image of a Pt/Ir coated Synechococcus S-layer in which multiple scans had dislodged one particle and left a hole. The S-layer was then imaged reproducibly for a long time even though there was no metal coating over the hole. We assumed the tip was too broad to penetrate the hole and do further damage, and the current tunnelled from the side of the tip to the nearby metal when the tip was over the bare part.

In order to test whether conductive coating is necessary for providing conductivity for biological samples or only acts to immobilize the structure against the lateral force exerted by the tip, I attempted to remove the coating films on biological samples and do imaging after. Imaging at reduced gap resistances (~200 MΩ) usually resulted in complete breaking of the film and then complete damage of structures. A better controlled way was to break part of the coating. Figure 5.14a is a Pt/Ir coated plug imaged at a tunneling current of 0.2 nA and bias voltage of 0.2 V. There is a crack in the near bottom, which presumably formed before the coating procedure. The bias voltage was then reduced to 0.05 V, a few lines of scan was taken on top but near the bottom edge of the plug, the scan was interrupted and the bias voltage was changed back to 0.2 V. Figure 5.14b is the image taken after, which showed substantial damage. The damaged part, which is lower than the undamaged part still shows the periodic structure. However, by closely examining the structure, we conclude that the top layer collapsed down (perhaps with some of the lower layers removed) but was still covered with the coating which therefore resulted in stable imaging. We did not observe any successful tunneling cases on bare biological samples.

Using the thinnest possible metal coating that still allowed conduction minimized the masking of the underlying structure. However, we found that films a few Angstroms thicker than the minimum allowed us to get stable and reproducible images, and in some cases better resolution, while using a magnitude smaller gap resistance. Obviously, the conductivity of the sample has an effect on the force for a given gap resistance, since poor conductivity of the

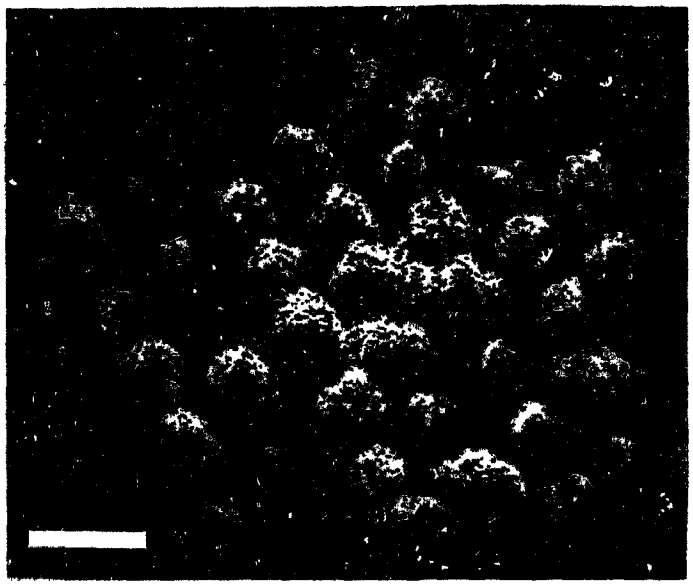

Figure 5.13: STM image of a Pr/Ir coated S-layer. The tip dislodged one structural unit after a few scans. Bar is 30 nm.

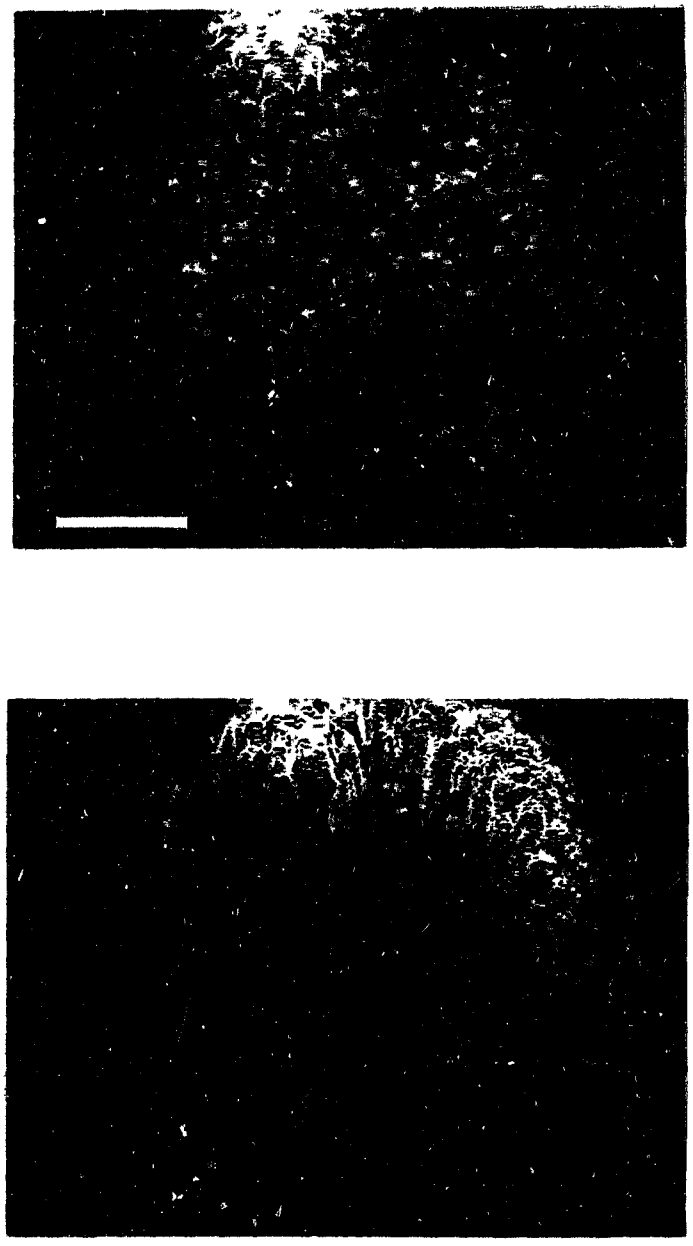

Figure 5.14a: An image of a Pt/Ir coated plug recorded at a normal bias voltage 0.2 V; 5.14b: The same plug recorded at the same bias voltage but after permanent damage was made by reducing the bias voltage to 0.05 V. Bar is 100 nm.

sample requires smaller spacing between the tip and sample for a given gap resistance. Optimum film thickness is a compromise between the conductivity of the coating film and the visibility of the underlying structure. Better resolution may arise from investigating the effects of film thickness and gap resistance on image quality.

Smaller forces produce elastic deformation of the sample, therefore reducing resolution and affecting image interpretation. The height of a soft specimen will appear smaller because of the elastic indentation by the tip force. To evaluate the effect of possible surface deformation on the thickness measurements of the metal coated samples, I took barrier height measurements on coated structures and on background. Low values (~30 meV) were obtained while no significant differences were detected on the plug or sheath, and on background. Changing the gap resistance also had little effect on the relative height of the structures. We conclude that the deformation due to tip-sample interaction did not significantly affect the thickness measurements under our large, ~1 GΩ, gap resistance conditions. The effect of the elastic deformation on the lateral resolution is difficult to estimate but is expected to be small since the structure was likely not distorted significantly in the lateral dimension.

In the above discussions about image resolution and interpretation the effect from the electromechanical response of the instrument was not considered. D.J.Thomson [69] reported some simulations of this effect on the resolution in the case of AFM imaging. The effect from the electromechanical response is expected to be minor in this study.

Conclusions

I presented a detailed study of the metal coating technique for imaging biological macromolecules with STM. The surface characteristics of cell plugs of Methanospirillum hungatei was resolved unambiguously, and the register alignment of the plug layers was identified for the first time. The ~3 nm x 3 nm 2-D lattice structure of the S-layer sheath was observed, which confirmed the result from diffraction studies. The ~1 nm resolution obtained on sheath coated with Pt/Ir films suggests that film graininess was very small for the Pt/Ir films used, even though they were vacuum deposited at room temperature without any special procedures. Furthermore, resolution depends on a compromise between the conductivity and the thickness of the film. The STM has a role as a routine structural analysis tool complementary to TEM, and contributes to a better understanding of the three-dimensional structure of biomolecules and their biological function.

Both the grain size of the metal coating and the geometry of the tip limit the resolution and affect image interpretation. Identification of structural details of a few nm size requires a careful examination of the image to exclude possible artifacts due to the film and or due to the tip convolution. The finer structure observed on plugs remained unidentified. Further study with tips of increased sharpness will help to answer the question whether this ~3 nm structure rs to the molecular structure of the plug.

Part ? Measurements of the elastic properties of biological materials by SFM

6 Introduction

6.1 General background of SFM

SFM was invented in 1986 by Binnig, Quate, and Gerber [70], to overcome the limitation of STM, which can image only conducting materials. The interaction force between a tip and the sample is used to image the surface topography (Figure 6.1). A cantilever with a sharp tip attached to its end serves as a force sensor. While scanning, forces between surface features and the tip deflect the cantilever. A displacement detector measures the cantilever's position, which can be used to determine the force on the tip through Hooke's Law, F=-KZ, where K is the spring constant of the cantilever and Z is the cantilever displacement. Recording the cantilever deflection generates a force map or image of the samples' surface.

The SFM has been used to observe atomic features on both conductors and insulators [71]. True atomic resolution has recently been demonstrated on the cleavage plane of calcite by using imaging forces of 10^{-10} N or less [72]. SFM has been used to probe various forces and nanomechanical properties of materials [73,74], and to modify surfaces [75]. In the field of biology, it has been used to observe cell processes in real time [76].

6.2 Summary of early sample elasticity measurement by SFM

The SFM can be used to probe certain mechanical properties of the sample by measuring the response of the sample to an increased or decreased load by the tip. Two methods have been used to study the elastic properties of the sample.

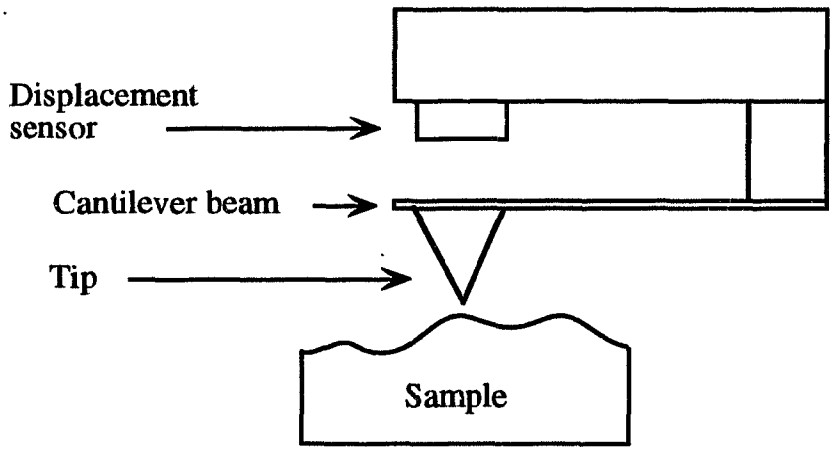

Figure 6.1: Schematic of the basic principle and instrumentation of force microscopy.

6.2.1 Force curve method

Figure 6.2 is a diagram of a force curve, a plot of the force as a function of relative tip-sample separation. The measurement starts with a large tip-sample separation in the non-touching regime. From there, with only little or no deflection of the cantilever, the sample approaches the tip along the horizontal line to the left in the diagram. At a certain tip-sample separation the tip jumps into contact with the sample surface to point *A*. Moving the sample further causes the deflection of the cantilever. If the sample is infinitely stiff, the cantilever deflects the same amount as the sample is moved, this is represented by line *AB*. However, if the sample deforms, the lever deflects following a line such as *AB'*. The force applied, F, and the surface indentation, d, at a particular point, say point *B'*, can be determined by $F=KD_{BC}$, and $d=D_{BB'}$. An indentation curve is obtained by plotting d against F, providing information about the response of the sample to a force. The elastic modulus of the sample can be determined by analyzing the indentation data using a relevant elastic indentation model.

N.Burnham et al. [74] used the force curve method to measure several elasto-plastic properties of materials: the elastic modulus and hardness, the surface forces associated with tip-surface interaction, and the adhesive forces associated with small contacts. Their experiment demonstrated the promise and power of using SFM for this research. They calculated the Young's modulus to be 10^7 N/m^2 for elastomer and 2.25 x 10^8 N/m^2 for graphite.

Weisenhorn et al. [77] measured force curves of a variety of materials. They obtained quantitative information about the elastic modulus of the sample. First they measured the force curves on a material with known Young's modulus, and estimated the geometry of the tip by fitting this force curve with the theory. Next they used the determined tip shape in the calculation of the unknown Young's modulus of other materials. The materials they

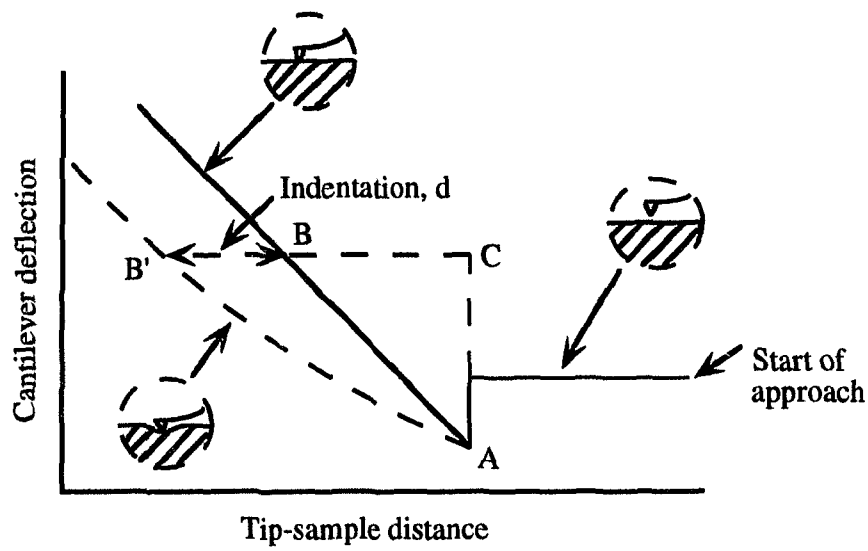

Figure 6.2: Schematic force versus distance curves of soft and hard material. The x-axis represents the distance by which the sample moves towards the tip. The y-axis shows the optic signal which represents the deflection of the cantilever.

examined were soft, with Young's moduli ranging from 10^4 to 10^6 N/m^2.

6.2.2 Force modulation method

Figure 6.3 is a schematic of elasticity measurement by the force modulation method. The modulation of the vertical sample position leads to a modulation of the force between tip and sample. The idea of elasticity measurement by the modulation technique is similar to the force curve method. The difference in the vibrational amplitudes of the sample and the measured response of the cantilever is caused by the surface indentation. Unlike the force curve method, this measurement can be taken while scanning. As the modulation is faster than the response of the feedback system which functions to keep the force constant while the tip is scanned across the surface, topographic images can be recorded as normal. Meanwhile, a map of surface elasticity can be obtained simultaneously by recording the in-phase amplitude response of the cantilever, which varies across the surface if the surface's elastic properties are not uniform.

P.Maivald et al. [78] used this force modulation technique to map the surface elasticity of a carbon fibre and epoxy composite. They found contrast between the two materials and demonstrated the sensitivity of this technique to image mechanical properties of different specimens. M.Radmacher et al. [79] did more careful measurements with this method, and in addition to the topographic and elasticity images they were also able to determine the viscosity by recording the phase shift of the lever response to the modulation. They presented viscoelastic images of Langmuir-Blodgett films of a polymeric amphiphile and of a structured fatty acid. They also gave a theoretical treatment of the elastic tip-sample interaction. Our research group also used this technique to measure the elastic properties of materials such as chitin fibres [80].

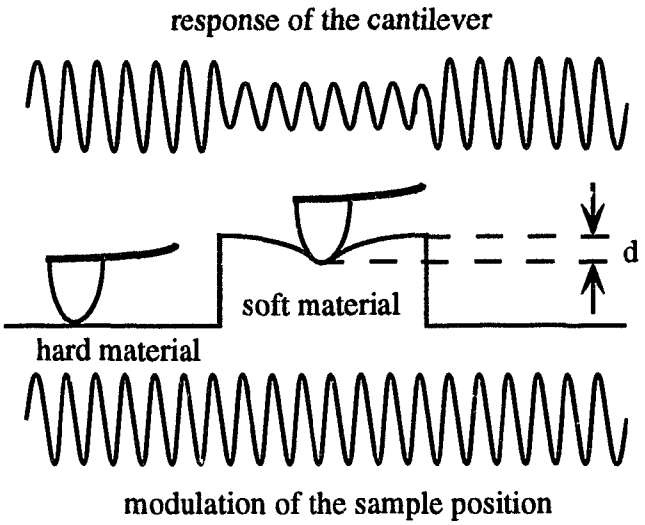

Figure 6.3: Schematic of the force modulation method of elasticity measurement.

6.3 Development of a new technique for elasticity measurement of biological materials

6.3.1 Motivation

SFM has achieved great success in imaging biological materials. Many SFM images of biological materials have been published, including DNA [81,82], membranes [83], surface protein layer [84], macromolecular fibres [80], living cells [76], etc. Some of them were of sufficient resolution to reveal the molecular details of the structures.

W.Haberle et al. investigated the response of living monkey-kidney cells to viruses infection [76], M.Fritz et al. probed the activation of human platelets by SFM [85], and H.Hansma et al. used SFM to dissect plasmids in propanol [82]. These examples showed the ability of SFM to image cell processes, and to manipulate and communicate with the biological structures. Such examples represent new possibilities for application in the field of biology.

In applying SFM to the study of biology, we look for all the opportunities this new tool could bring to biology. One of the greatest advantages of SFM lies with the ability to probe mechanical properties at the nanometer level. Studies of mechanical properties of biological materials are important for an understanding of their function in many physiological and pathological processes [86]. For example, the elastic properties of materials can determine to what extent applied stress and strain modulate the morphology and metabolism of a cell [87]. Direct measurements of elastic properties on a nanometer scale will provide information about the properties at the molecular level and will allow structural biologists to address questions that could never before be answered.

Very few techniques exist that can measure elastic properties on the cellular or sub-cellular levels. The elastic area compressibility modulus of red blood cell membranes was measured with an area dilation method based on the micropipette aspiration [88]. The elastic area compressibility modulus of the erythrocyte membrane was measured using cell poking,

a cell indenting method [86].

As mentioned in the previous section, two SFM methods were used to measure the elastic properties of samples, including some biological specimens. Both methods are based on surface indentation measurements, are only suitable for measuring materials which can be treated as isotropic and infinite half spaces. In Weisenhorn et al.'s experiment, the materials used were either very large (mm in dimension) or very soft (living cells with Young's moduli of 0.13 - 1.5 x 10^5 N/m^2), the depth of indentation was at the order of 10 nm to 400 nm under a force of ~10^{-8} N or less. For small biological materials such as thin membranes deposited on a hard substrate, the force which can be applied to indent the material is limited. Substrate effects may be involved if the indenter penetrates more than a certain critical distance, especially in cases where the materials are not very soft compared to the substrate. Small indentations as response to low loading forces are difficult to detect by the force curve method. Although the force modulation method may allow us to detect smaller indentations, the influences of the tip geometry, surface forces, and interface conditions to the measurement all become significant at low forces. We are also concerned about the fact that for biological materials the small surface indentation may not directly relate to the bulk elastic properties of the material.

6.3.2 Development of a new technique

We used a different approach in this investigation. Instead of resting on a substrate, the material is suspended over a groove in a substrate and free to bend or stretch (Figure 6.4). Measurement of the bending or stretching deflection due to a force applied by the tip determined the elastic properties of the material.

The idea of measuring the deformation of a suspended material was introduced by M.H Jericho et al. [80]. The deflection of a chitin fibre suspended over supports formed by

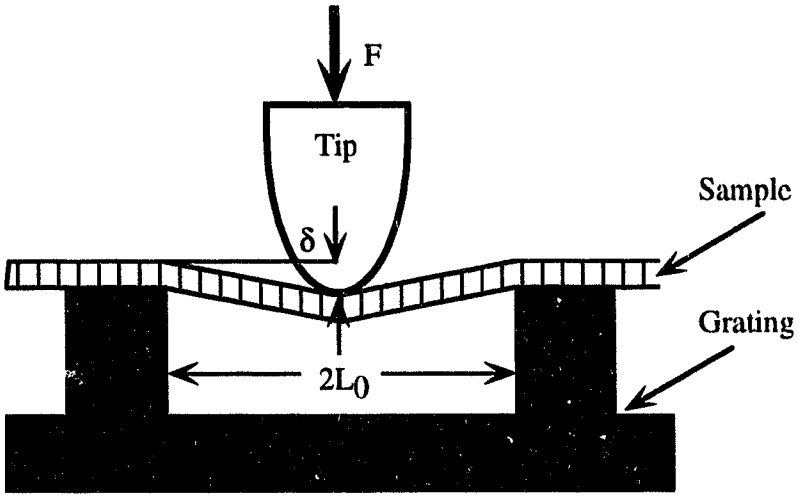

Figure 6.4: Illustration of the suspension method of elasticity measurement.

two other fibres was measured. The chitin fibres appeared rigid, with a Young's modulus of $(1 \pm 0.5) \times 10^{11}$ N/m^2. A.George [89] carried out an experiment to estimate the force exerted on the sample by the STM tip. In his experiment, a diffraction grating was used to suspend chitin fibres, and the sample was coated with gold film in order to do STM imaging.

6.3.3 Scope of the present investigation

The objective of this investigation is to develop a technique to measure the elastic properties of biological materials. It was hoped that the suspension method could provide more accurate deformation data on materials with small thicknesses (a few nm) than the previous methods, and result in bulk elastic properties which are relevant to the material. The investigation includes finding a proper substrate, a reliable sample preparation method to suspend the material, techniques to control the force and measure the response of the sample, and suitable models for interpretation of the data. The two specimens we chose to examine, chitin fibres and the Mh bacterial sheath, are composed of polysaccharide and protein, respectively, two of the most important organic molecules found in cells. The mechanical properties of these materials play an important role in their cell function. Both chitin and sheath have a well defined shape, which makes theoretical modelling relatively easy. From these two relatively simple systems we hope to establish the basis for the suspension method, and extend these studies to more complicated structures.

An ion milled GaAs grating* was used as a substrate to suspend the biological materials. Successfully suspending the biological material over the grating was critical to the measurement and proved not trivial for some materials. Efforts were made to overcome

---

*Fabricated by the institute for Microstructural Sciences at the National Research Council, Ottawa, Canada

problems such as capillary action which pulls materials into grooves.

There are different ways to vary the force and measure the sample's response. In this experiment we used two methods with emphasis on precise lateral position control during measurements. Efforts have also gone into the development of suitable models to interpret the data which describes the deformation of the material under the force. For Mh sheath, one of the materials we examined, a hoop model is used for taking into account its inhomogeneous elastic properties.

With this suspension method we can study other interesting properties of biological materials, such as the ultimate strength of the material. From analyzing the measured yield strength we estimated properties such as the maximum extension the hoop bond could sustain, the number of covalent bonds between hoops, and the maximum sustainable internal pressure of the *Methanospirillum hungatei* organism. The present experiment has proved of great potential to provide information about the biological mechanisms. It may also allow us in future to examine properties about mechanical changes triggered by external stimuli, such as effects of antibiotics on the elastic properties of biological materials.

7 Theory

The SFM detects the interaction forces between the tip and the surface. The dominant interaction between the tip and sample is determined by the distance between them, their properties and the intervening medium. For example, van der Waals forces are significant up to hundreds of Angstroms, while ionic repulsion only acts if the surfaces are not more than a few Angstroms apart. Other interaction forces such as capillary forces, magnetic and electrostatic forces, and frictional forces may exist under specific conditions. Detailed discussion on these forces and their measurements with SFM are described in a number of references [90,91].

7.1 Scanning force microscope imaging

In the SFM (Fig. 6.1) a cantilever which is integrated with the tip responds to the interaction force by deflecting the cantilever beam. A displacement detector is used to measure the cantilever's displacement, which can then be used to determine the force on the tip by using Hooke's Law, F=-KZ, where K is the spring constant and Z is the cantilever displacement.

The SFM can be operated in the contact regime or noncontact regime, depending on whether the cantilever tip and sample are touching. In the contact regime the repulsive forces between the ions of the sample and the ions of the tip are governed by an inverse power law with large exponents, therefore are extremely sensitive to the height of the tip above the surface. Scanning in this regime reveals the surface topography of the sample with a resolution down to atomic scale. In analogy to the operation modes of the STM, such as constant current and constant height mode, the force can be kept constant or varied during scanning to operate the SFM in the constant force mode or constant height mode. In the

noncontact regime the detected forces are only attractive. Another operation mode, constant force gradient mode, is commonly used for the noncontact imaging because it has low sensitivity to variations in gap distance due to thermal drift which is a severe problem in noncontact imaging.

The principle for tip height control, scanning and data recording is identical to that of STM as discussed in Chapter 4.

7.2 Elasticity measurements with the SFM

7.2.1 Elastic model of the SFM system

The SFM can be configured to determine the elastic properties of the sample by varying the force and detecting the response of the sample. The essential concept of elasticity measurements can be elucidated by modelling the entire mechanical system with a set of springs in series, as shown in Figure 7.1.

The cantilever, tip, and the sample are modeled by springs with spring constants K_c, K_t, and K_s, respectively. The base and the piezo are assumed rigid so that they do not compress as force is applied. Z_p is the distance between the z-piezo and the back of the sample (this distance is controlled by the voltage applied to the piezo), Z_g is the gap between the piezo and the back of the lever (this is measured by the displacement detector), Z_t is the length of the tip, and Z_s is the height of the sample.

The length Z_p from the back of the sample to the piezo is

$$Z_p = Z_g + Z_t + Z_s . \qquad 7.1$$

Let ΔZ_p represent a change in the position of the piezo. Applying Hooke's law, the

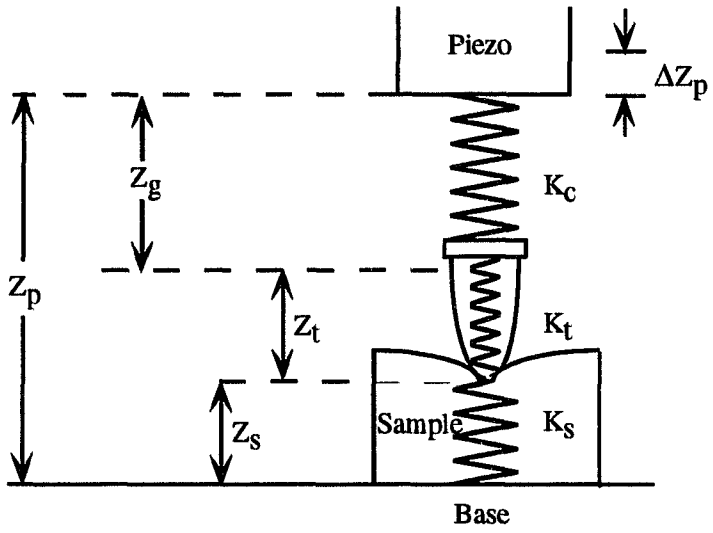

Figure 7.1: Spring model of the components of a SFM.

change in the interaction force ΔF between the tip and sample can be written as

$$\Delta F=\Delta Z_p/\left(\frac{1}{K_c}+\frac{1}{K_t}+\frac{1}{K_s}\right)=\Delta Z_p/\left(\frac{1}{K_c}+\frac{1}{K_i}\right) \qquad 7.2$$

here we have denoted the stiffness of the entire tip-sample interaction as K_i, since in our measurement only the position of the piezo and the distance between the piezo and the back of the cantilever are detected, there is no direct information on Z_t and Z_s. In a force curve measurement, the z-piezo is moved towards or away from the sample, changing the length Z_p from the back of the sample to the piezo by ΔZ_p. This results in a change of the gap between the piezo and the back of the cantilever ΔZ_g, thus a change of force by $\Delta F=K_c\ \Delta Z_g$. The force curve is generated by recording this force change ΔF against the position change of the z-piezo ΔZ_p. The slope of this curve gives the total stiffness K_m defined by $K_i\ K_c/(K_i+K_c)$. The difference in ΔZ_p and ΔZ_g is the deformation of the tip-sample system. The tip-sample interaction stiffness K_i can be found from K_m if K_c is not too small compared to K_i. The measured stiffness will be dominated by the weakest spring in the series. In cases where the sample is much softer than the tip, we can assume the tip to have negligible elastic deformation. Therefore $K_i=K_s$. Both the stiffness and the deformation of the sample can be determined from the force curve.

Capillary forces modify the interaction between the tip and sample, in particular, increase the contact area and the force the tip exerts on surface atoms of the material under the tip apex. These internal forces, however, do not transmit through the sample as the loading force does. I leave the discussion of the effect of capillary forces on force measurements to chapter 10.

7.2.2 Elastic models of the response of the sample

A force may make a sample indent, bend, or stretch. To convert the measured data to the important parameters such as the Young's modulus of the material, we must use the relevant deformation model.

(a) Surface indentation

If the deformation is caused by surface indentation, as is usual in the SFM contact mode imaging, the Hertzian model [92] describes the functional dependence of the relevant variables. A force F on a tip with radius R leads to an indentation of depth d in the sample according to:

$$d^3 = \frac{9\pi^2}{16}\frac{F^2}{E^{*2}R} \qquad 7.3$$

$E^*=\pi E/(1-\nu^2)$, where ν is the Poisson ratio, and E is the Young's modulus. This analysis assumes that the deformation of the tip is negligible compared to that of the much softer sample. The Young's modulus of the material can be determined from a plot of indentation versus force.

Expanding this relation around a typical equilibrium load F_0 we obtain the form:

$$\frac{\partial F}{\partial d}=K_i=\left[\left(\frac{6}{\pi^2}\right)\left(E^{*2}RF_0\right)\right]^{1/3} \qquad 7.4$$

This equation can be used to calculate the local elastic modulus of the sample after the K_i is determined.

(b) Beam deflection

A suspended material responds to a normal force by deflecting vertically. The experiments described here exclusively use materials suspended at both ends.

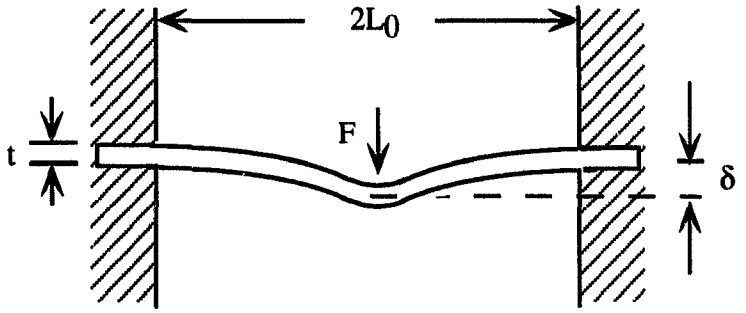

Figure 7.2: Schematic of a clamped beam bent by a normal force applied mid-point.

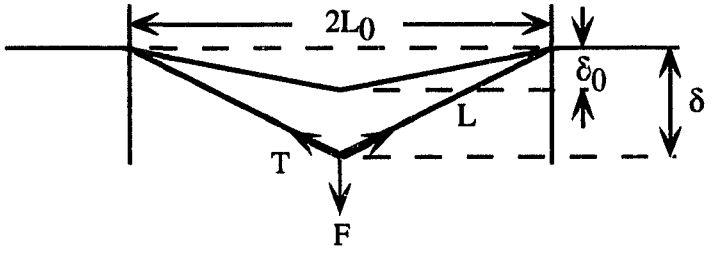

Figure 7.3: Schematic of an ends fixed strip stretched by a normal force applied mid-point.

Consider a uniform rectangular beam clamped at both ends bent by a force applied to its mid-point, as shown in the Figure 7.2. According to the standard elastic theory [93], the relation between the applied force F and the deformation δ can be expressed in the form:

$$\delta = \frac{1}{16}\frac{F}{wE}\left(\frac{2L_0}{t}\right)^3 \qquad 7.5$$

where E is the Young's modulus of the beam material, $2L_0$, w, and t are the length, width, and thickness of the beam, respectively.

The deformation of the beam is a linear function of the applied force. Therefore the Young's modulus can be calculated from

$$E = \frac{1}{16}\frac{dF}{d\delta}\frac{1}{w}\left(\frac{2L_0}{t}\right)^3 \qquad 7.6$$

if the deflection change to a force change is measured, and the dimensions of the beam are known.

For a beam with ends simply supported instead of clamped, the deformation is described by a similar form to Eqn. 7.5. but with a coefficient of 1/4 instead of 1/16.

Equations 7.5 and 7.6 are only valid for deflections which are much smaller than the suspended length of the beam.

(c) Thin plate deflection

One of the materials studied was a Mh membrane that could be modelled as a rectangular thin plate with two sides clamped and the other two sides free.

The deflection problem of a rectangular plate with the imposed boundary conditions as stated above under a given normal pressure is very complex, and can not be solved analytically, and has not been solved numerically.

The bending problem of a plate with the boundary condition we have here was solved using an approximate method by Timoshenko [94]. However we knew from earlier STM and SFM imaging that the sheath material has very little bending rigidity [56,95]. Therefore a limiting case of pure stretching is relevant here instead of pure bending. We will model the problem as a plate stretched by a normal force, in which only tensile forces in the plate are considered.

(i) Plate stretching

In the pure stretching model, the vertical deflection δ of a plate of thickness t relates to the pressure P applied vertically by equations [93]:

$$t\left(\frac{\partial^2\chi}{\partial y^2}\frac{\partial^2\delta}{\partial x^2}+\frac{\partial^2\chi}{\partial x^2}\frac{\partial^2\delta}{\partial y^2}-2\frac{\partial^2\chi}{\partial x\partial y}\frac{\partial^2\delta}{\partial x\partial y}\right)+P=0 \qquad 7.7$$

$$\nabla^4\chi+E\left[\frac{\partial^2\delta}{\partial x^2}\frac{\partial^2\delta}{\partial y^2}-\left(\frac{\partial^2\delta}{\partial x\partial y}\right)^2\right]=0 \qquad 7.8$$

These equations are very complicated, analytical solutions were possible only under some extreme approximations such as the Membrane approximation. A membrane is a thin sheet subject to large external stretching forces applied at its circumference. In the case of isotropic stretching, when the extension of the membrane is the same in all directions, the problem reduces to solving a Poisson equation [93].

$$T\nabla^2\delta+P=0 \qquad 7.9$$

where $\bar{T}$ is the absolute magnitude of the stretching force per unit length.

The membrane we are dealing with is a cell component, its boundary is not sealed and

it is not subjected to a large external stretching force applied to its circumference, therefore the conditions for the membrane approximation are not met for our problem.

An estimate of the terms in Eqn.7.8 from dimensional consideration shows that $\chi \sim E\delta^2$. The order of magnitude of the first term in Eqn.7.7 is then $t\delta\chi/L^4 \sim Et\delta^3/L^4$ (L is the dimension of the plate). Therefore, we see that the deflection δ is proportional to the cube root of the force in this pure stretching case. If the force is applied uniformly across the width of the plate, the problem can be solved easily by using stress and strain analysis of one dimensional case (Figure 7.3). The relationship between the relevant variables is

$$F \sim WtE(1/L_0)^3\delta(\delta^2-\delta_0^2) \qquad 7.10$$

where w is the width of the strip and $2L_0$ is the length of the suspended region. An initial sag at zero loading force is considered, which is important in the experiment. The cube root dependence of the deflection on the force comes from the fact that the tension in the strip, T, which relates to the vertical force by $T=F/2(L_0/\delta)$, and the extension of the strip, $\epsilon=L-L_0=(\delta^2-\delta_0^2)/2L_0$, follows Hooke's law

$$T=wtE\frac{\epsilon}{L_0}. \qquad 7.11$$

(ii) Trapezoidal model

In the experiment, the sheath of 690 nm width (collapsed double layer) bridges the 300 nm gap, and a tip with a radius of about 20 nm presses at the center of the sheath. The extraction of the elastic properties from the deflection measurement is complicated by this geometry, as shown through Eqns. 7.7 and 7.8. We simplify the problem here by making some

assumptions, that will then allow us to use simple geometric analysis and Hooke's law to derive the functional dependence of the relevant variables.

Figure 7.4a is a diagram of the trapezoidal model. We assumed that the strain on a thin membrane clamped at two ends only and loaded in the centre is taken primarily by the two trapezoidal regions shown shaded in Fig. 7.4a, and the free edges take minimal strain. (Macroscopically, this can be illustrated by clamping the opposite ends of a piece of plastic wrap and putting a small weight on the centre.) The problem then reduces to a calculation of the strains in a trapezoidally shaped membrane when a stress is applied at the narrow end.

If the ratio of the width of the wider end, w_0, to the length of the trapezoid, L_0, is much less than unity then the tensile force per unit length is approximately constant across the trapezoid and equals T/w along any horizontal line of width $w=w_0-y(w_0-w_t)/L_0$. In that case the total extension, ϵ, of the trapezoid when a tension, T, is applied to the narrow end (see Figure 7.4b) is given by

$$e=\int_0^{L_0}\frac{1}{E}\frac{T}{wt}dy. \qquad 7.12$$

This results in

$$T=w_{eff}tE\frac{e}{L_0} \qquad 7.13$$

where the effective width, w_{eff}, is

$$w_{eff}=\frac{(w_0-w_t)}{\ln(w_0/w_t)}, \qquad 7.14$$

defined as an analogy to the one dimensional case. The problem is equivalent to that for a

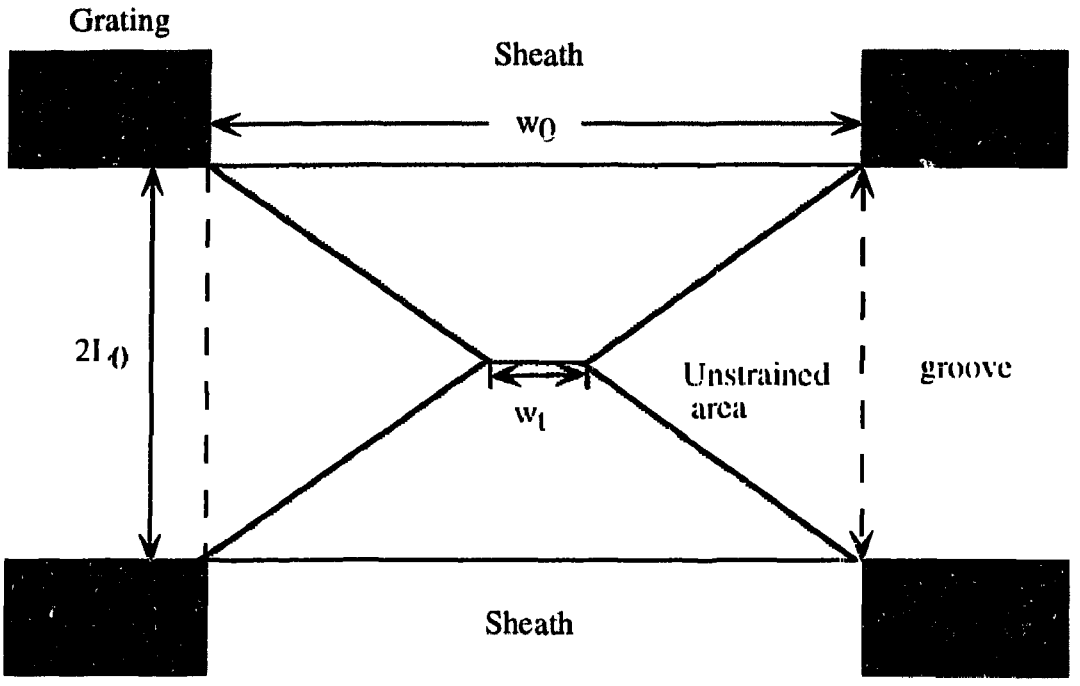

Figure 7.4a: Diagram showing the geometry of the suspended sheath loaded at the center. The strain is taken by the two trapezoidally shaped areas bounded by the width of the sheath, w_0, at the grating side, and by a length of w_t that represents the contact diameter of the tip at the tip side.

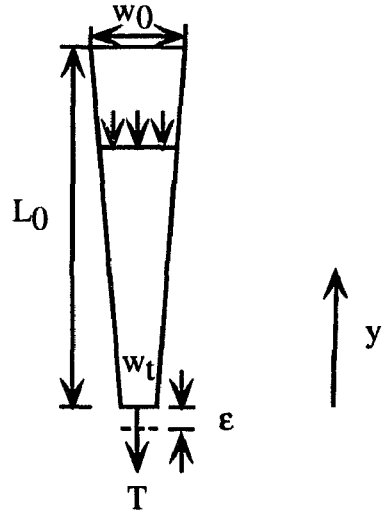

Figure 7.4b: A trapezoid with $L_0 >> w_0$. The tension is uniform across the trapezoid and equals T/w along any horizontal line of width w.

strip of width w_{eff} stretched by a normal force which is uniformly applied along the width (Eqn. 7.11).

On the other hand, if $w_0 \geq L_0$ then the stress is no longer uniform across the membrane but is largest near the center region. To obtain an estimate of the total stretch of the membrane for an applied load at the center and hence an estimate for the deflection of the AFM cantilever, we divided the principal trapezoidal regions into sections each of angular width $d\theta$ as shown in Figure 7.5. Each section is bounded by the groove edge on one end and by a circular arc that represents the contact circle of the AFM tip on the other end. Each angular section is now treated as an independent trapezoid of mean length $L_i=L_0/\cos(\theta)$. The effects of shear distortions in the membrane are therefore neglected. For the membrane to remain flat, an applied load that stretches the central trapezoid by an amount Δl_c must stretch the trapezoid at the angular position θ by an amount $\Delta l_i=\Delta l_c\cos(\theta)$. If the membrane is treated as an elastically homogeneous sheet, then the strain for the i^{th} section is

$$\Delta l_i / L_i = \frac{1}{E} (T_i / S_{ieff} t)\, d\theta . \qquad 7.15$$

The tension per unit angle in the i^{th} section in terms of the tension in the central section is given by

$$T_i = T_c (S_{ieff} / S_{ceff}) \cos^2(\theta) . \qquad 7.16$$

Following Eqn.7.14, the effective width of the i^{th} section S_{ieff} in Eqns. 7.15 and 7.16 is given by

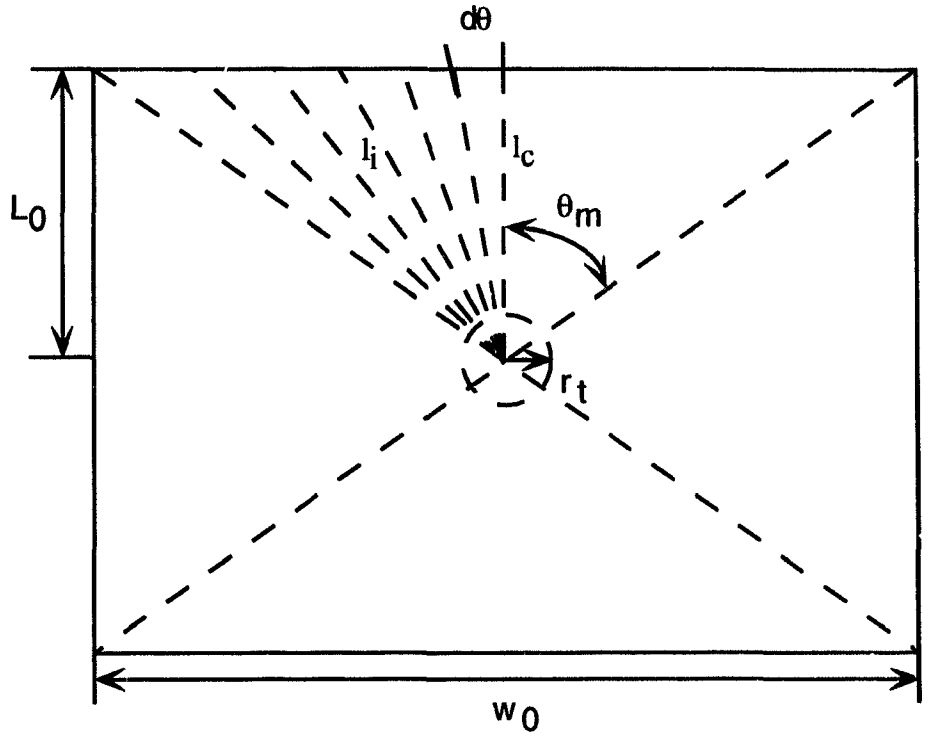

Figure 7.5: Diagram showing the idea of stress and strain analysis for a wide trapezoid.

$$S_{ieff}=\frac{(L_0/\cos(\theta))\,d\theta - r_t d\theta}{\ln(L_0/r_t\cos(\theta))}. \qquad 7.17$$

The component of T_i that is on the plane of the membrane and perpendicular to the groove edge is

$$T_{iv}=\frac{T_c\cos^2(\theta)}{1-\dfrac{\ln(\cos(\theta))}{\ln(L_0/r_t)}} \quad for\ L_0/r_t>1. \qquad 7.18$$

The total tensile force, T, perpendicular to the groove edge is

$$T=2\int_0^{\theta_m} T_{iv}\,d\theta \qquad 7.19$$

where θ_m is the maximum angular width for the membrane.

The logarithmic term in Eqn. 7.18 is zero when θ=0 and varies slowly with increasing θ compared to the $\cos^2(\theta)$ term. We neglected this term in the integration and then obtained the following approximate expression for the tension per unit angle:

$$T_{iv}\cong\frac{T\cos^2(\theta)}{f(\theta_m)} \quad where\ f(\theta_m)=\theta_m+\frac{1}{2}\sin(2\theta_m) \qquad 7.20$$

If the principal trapezoidal regions remain plane after a load is applied, then the extension Δl_c of the central section can be related to the total membrane depression relative to the substrate, δ, by simple geometry (Fig. 7.3) and $\Delta l_c=(\delta^2-\delta_0^2)/2L_0$, and also the tension in the plane, T, relates to the vertical load applied, F, by $F=2T(\delta/L_0)$. Applying Eqns. 7.15 and 7.20 to the central section suggests the following relationship between force and membrane depression:

$$F/\delta = \frac{f(\theta_m)}{L_0^2 \ln(L_0/r_t)} tE(\delta^2 - \delta_0^2) . \qquad 7.21$$

This model was tested macroscopically by doing analogous experiments on plastic films [96]. Two types of experiments were performed. In the first type a complete rectangular shaped film spanned a gap and was deflected vertically under forces applied by a spherical loading device at the center. In the second type, the film was cut to a trapezoidal shape (shaded region in Fig. 7.4a). The relative dimensions of the rectangle and the trapezoid and the size of the deformer resembled that of the sheath, except the thickness. For both types of sample the depression depth at the center as a function of the applied load was measured. The results are plotted in Figure 7.6 in the form suggested by Eqn. 7.21. For both types of sample the data was well represented by Eqn. 7.21 and the results support the various assumptions made in the derivation of Eqn. 7.21. The slope of the lines in Fig. 7.6 permit a determination of the Young's modulus of the plastic films. The values obtained for the intact and cut films were $(1.0 \pm 0.1) \times 10^8$ N/m^2, same within the experimental error. A direct modulus measurement on a narrow strip of the film stretched vertically by fixing one end and hanging weights at the other end gave a value of $(1.18 \pm 0.02) \times 10^8$ N/m^2, in good agreement with the above value. For the simulation the contact radius of the spherical indentor could be determined directly by viewing the indentor through the transparent film. The agreement between Eqn. 7.21 and the data for the simulation experiments gives us confidence to apply the model later to the sheath suspended over a groove in the GaAs substrate.

(iii) Hoop model

The models discussed above are relevant only when the material is homogeneous. The hoop structure of the Mh sheath suggests that the sheath material is inhomogeneous. The

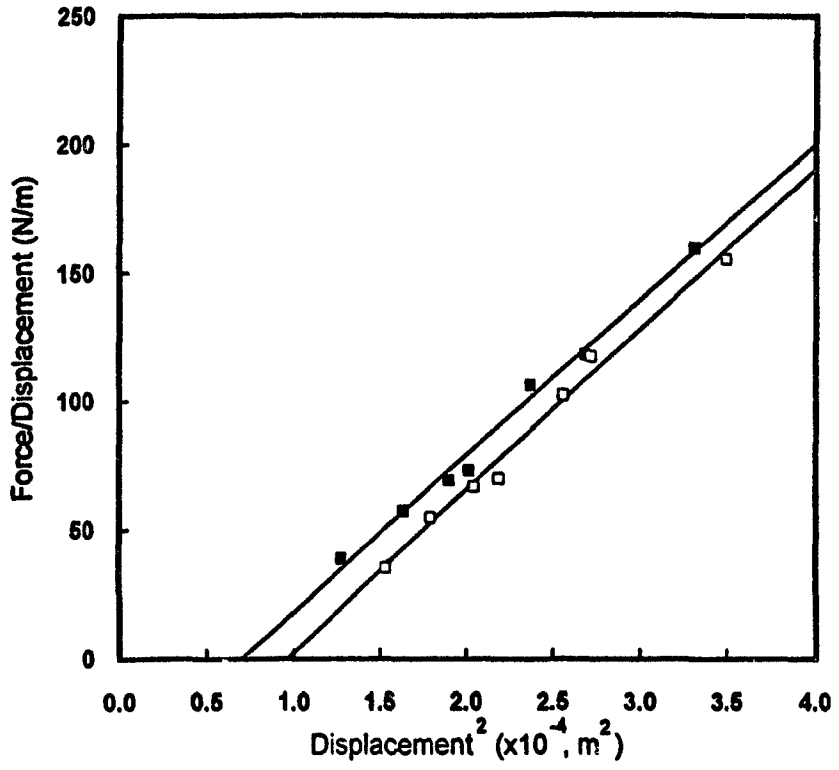

Figure 7.6: Plot of F/δ versus δ^2 of the data from simulation experiments on plastic films.

□: cut film; ■: complete film.

bonds holding the hoops together into a sheath are perhaps weaker [20] than the bonds of molecules in each hoop. In this case one might expect most of the stretch in the sheath under an applied load to come from the bonding elements that bind hoops to each other. To estimate the magnitude of the dilation of the gaps between hoops, we use a hoop model, which is depicted in Figure 7.7. The sheath consists of hoops which are about 3 nm wide. Each pair of hoops is joined by linear springs spaced with a distance of a, and each spring has a spring constant K_h. The bonding between the subunits within each hoop is unknown and was not modeled since we assumed the hoops are unstretchable. Now we are able to relate the deflection of the sheath δ under the force F to the molecular bonding properties which appear in the constant K_h/a:

$$F=\frac{1}{L_0^2\,(a/K_h)\,c}\,\delta\,(\delta^2-\delta_0^2) \qquad 7.22$$

where c is a size factor which is calculated by

$$c=\left(\frac{1}{w_0}+\frac{1}{w_1}+\frac{1}{w_2}+\cdots+\frac{1}{w_9}\right) \qquad 7.23$$

where w_0 through w_9 represent the widths of each joint between hoops in the trapezoid, and w_0 is taken as the width of the sheath. The total extension of the half sheath is

$$\epsilon_t=\Sigma\epsilon_i=\frac{1}{2L_0}\,(\delta^2-\delta_0^2) \qquad 7.24$$

with

7.25

$$\epsilon_i = T(a/K_h)/w_i$$

where T is the tension in the sheath as drawn in the diagram.

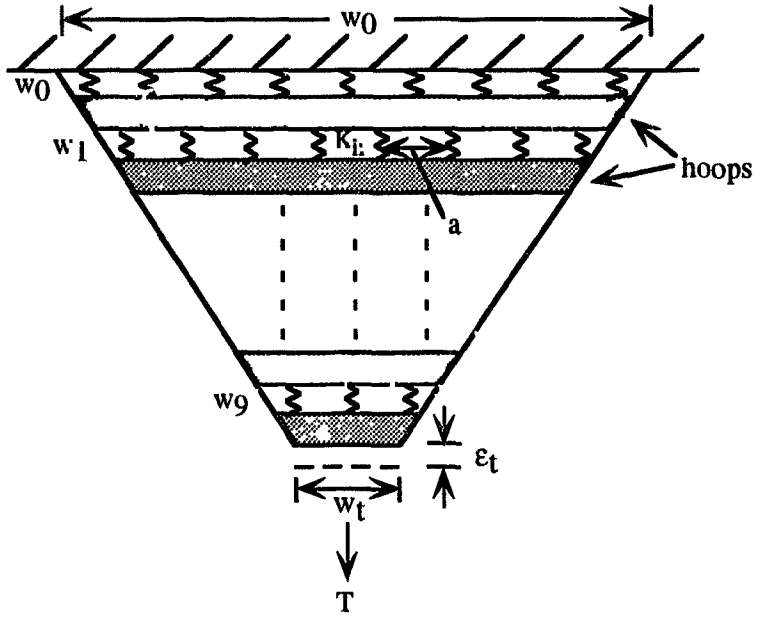

Figure 7.7: Hoop model. Each hoop is joined by springs with a spring constant of K_h and equally spaced with a distance of a.

8 Apparatus and measurements

8.1 The scanning force microscope

Figure 8.1 is a schematic of the SFM used in this investigation. It has been described in detail elsewhere [97]. In brief, Piezo bimorph disks are used to drive the xyz tripod arms for three dimensional movements. The cantilever is supported at one end on a detachable barrel at the end of the z arm, and free at the other end with an integrated tip at the bottom. The detection for cantilever deflection is an interferometer type. An optic fibre is held inside the z-arm with its end positioned a few μm from the back of the cantilever. Reflections from the cantilever and from the glass-air interface at the end of the fibre form an interference pattern which is used to measure the deflection of the cantilever. The light source is a high-stability single-mode He-Ne laser, model 210 from Laboratory for Science. The Si cantilever from Nanoprobe has a force constant of 0.16-0.48 N/m. The sample is situated below the lever, mounted on a stage bimorph which is on a movable stage. The coarse approach is done by advancing the stage towards the tip by a lever and a differential micrometer assembly described in reference [98].

A photomultiplier tube (PMT) is used to transfer the optic signal from the interferometer to a voltage signal, which is then fed into the input of the feedback circuit. The deflection of the cantilever due to the force exerted by the sample causes a change in intensity of the PMT output signal in a fringe pattern. Advancing the sample stage by 316.4 nm, half the wavelength of the He-Ne laser, causes an intensity change by one fringe in the PMT output, and a resultant change in force of 316.4 x K, where K is the force constant of the cantilever. A particular point on the fringe represents a particular force between the tip and the sample. A loading force is set by advancing the sample stage to the cantilever until the PMT signal reaches a predetermined interference intensity on the fringe, termed the

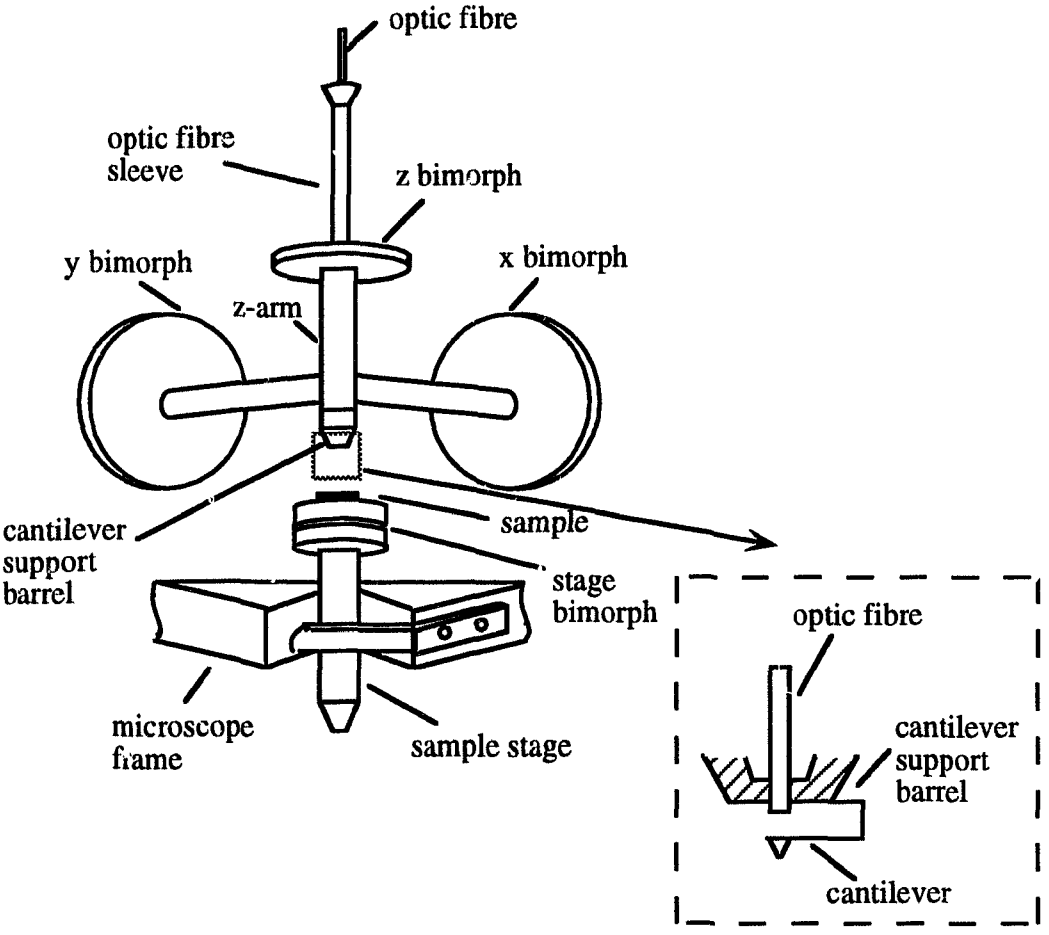

Figure 8.1: Schematic of the SFM.

operating point. In constant force mode, the feedback circuit compares the PMT signal with a reference voltage which is set for the particular interference intensity, and produces a voltage to adjust the z piezo to maintain that interference intensity. The movement of the z piezo is recorded to provide a topology of the surface.

8.2 Measurement techniques and experimental set-up

Figure 8.2 is a schematic of the suspension method and the experimental set-up for the elasticity measurement. The suspended material is pushed down midway. As the loading force is increased, the amount of deformation due to bending or stretching of the material responding to this force is measured. The force was varied by altering the reference setting of the feedback circuit while the feedback is on. A loading force was first set at a point at the most sensitive part of a fringe, operating point A. Altering the reference setting changed the operating point to A'. Changing the operating point on the fringe required changing the interferometer gap, which in turn meant bending the cantilever holding the tip. The amount of the produced force change was calculated from the cantilever force constant K_c and the change in cantilever deflection (or change in the interferometer gap) ΔZ_g: $\Delta F = K_c \Delta Z_g$. The movement of the z-piezo, ΔZ_p, was the sum of the deflection of the material under the tip and the change in the interferometer gap. Ideally, a displacement versus force curve is measured on an infinitely stiff substrate and is used as a reference to calibrate the force as a function of the measured voltage on the PMT signal, and the deflection of the material: the force varied is calculated by $\Delta F = K \Delta Z_p$, because the cantilever must deflect the same amount (ΔZ_g) as the z-piezo moved (ΔZ_p) on a surface which does not deform; the deflection of the material under investigation was the difference between the z-piezo displacement over the material and at a given force and the displacement over the substrate at the same force. In the experiment, the GaAs substrate has a Young's modulus of 7×10^9 N/m^2 [99] and its elastic

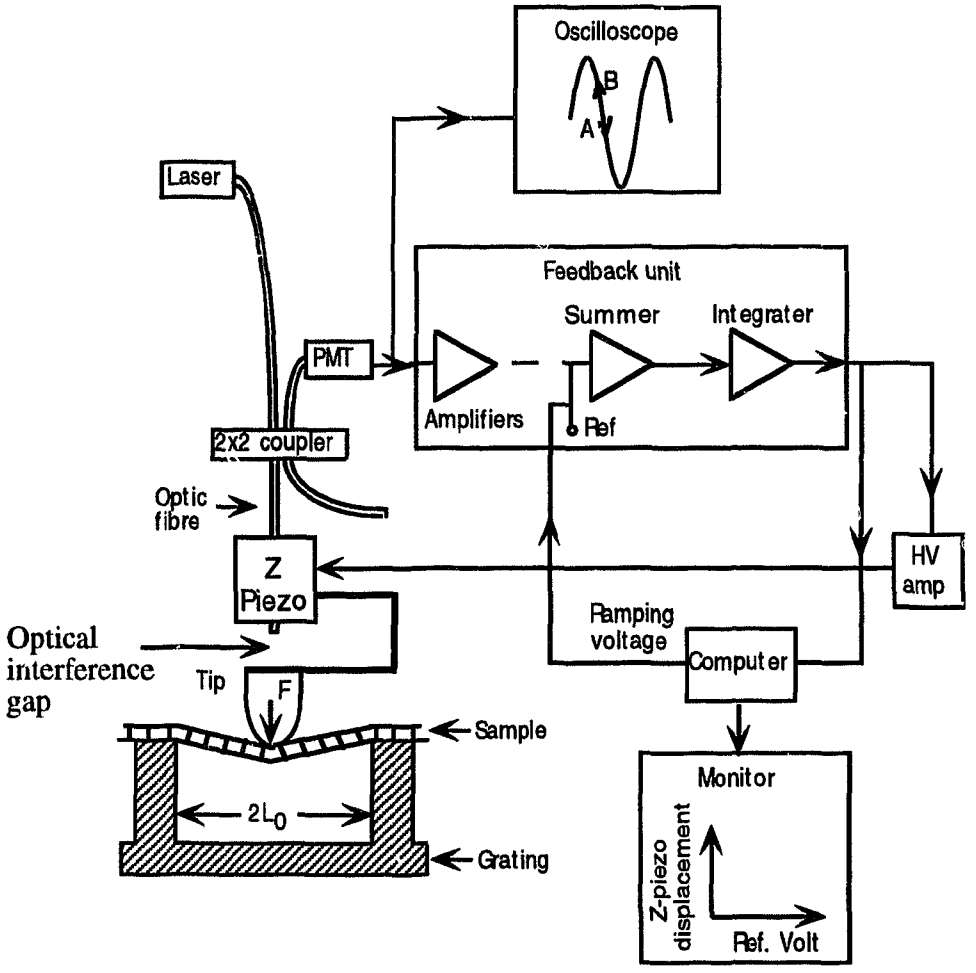

Figure 8.2: Schematic of the suspension method and the experimental set-up for the elasticity measurement.

yield is not negligible under the forces used. However the effect of the surface deformation of the GaAs substrate to the deflection measurement can be corrected with the help of indentation Eqn. 7.3 (details will be given in the result chapter).

An alternative measurement technique can be used if the suspended material has an intrinsic sag and the response of the system to an applied force is non-linear. Complete images of the material under consideration and the supporting grating can be measured at different imaging forces. Cross-sections through the images reveal the total depression at the center of the span relative to parts on the supports. Note the actual shape of the material can not be obtained from the image because the data corresponds to the deflection of the material when only the point being imaged was under load.

An interferometer displacement sensor has two disadvantages for the deflection measurements. First, the detected intensity is a sinusoidal function of the displacement. Linear variations in the reference voltage do not produce linear force variations. Second, the total lever deflection must be less than half a fringe and this limited the dynamic range of applied forces. To avoid non-linearity, we only changed the force within the linear range surrounding the operating point on the side of the fringe as shown in Figure 8.2. Larger force variations were performed by interrupting the feedback control and moving the sample stage to a new fringe.

The voltage ramping signal, which adds to the reference voltage to scan the force, was controlled by a computer interface system and the z-piezo voltage was simultaneously recorded. Each force curve had 400 data points. The whole cycle took 1 second. No significant alteration in the response were detected for cycle rates that were tenfold slower than 1 second. The response to both increasing and decreasing forces was recorded.

Large range scans were first performed to locate appropriately suspended materials. Once located, high resolution images were collected. The located area was re-scanned and the tip was positioned at the midpoint of the suspended material by holding the x and y piezo

voltages fixed (handled by the computer). A displacement versus force curve was then taken.

In the force curve measurements I described above, the tip was always in contact with the material, and the feedback control was never interrupted. This is different from the commonly used method to measure force curves in which the feedback control is interrupted and the tip is brought from noncontact to contact with the sample. The method I described here provides better position control which is important for measurements with the suspension method.

The z-drift rate of the microscope is ~0.4 nm/min, measured half an hour after making approach. This drift should not affect the force curve measurements which were completed within 1 second.

Measurements were done in air, images were recorded with the SFM operating in the contact regime and constant force mode.

8.3 Calibration of cantilever spring constants

The SFM probes were silicon cantilevers with integrated tips from Nanoprobe. The cantilever has a rectangular cross section. According to the manufacturer, the force constants are 0.03-0.12 N/m and the resonance frequencies are 5-7 KHz. More accurate values of the force constants were required for our Young's modulus measurements. We calibrated individual levers by the following method.

The spring constant, K, of an end-loaded cantilevered beam of rectangular cross section is given by [100]

$$K = \frac{Et^3 w}{4l^3} \qquad 8.1$$

where E is the Young's modulus, t, w, and l are the thickness, width, and the length,

respectively.

The variability of the spring constants for a single type of cantilever is most likely caused by variations of thickness of the cantilevers [101]. The thickness of the cantilever is submicrometers, close to the typical lateral resolution in photolithography.

By approximating the beam as a spring of stiffness K with an effective mass m^*, the resonant frequency is given by

$$\nu_0 = \frac{\omega_0}{2\pi} = \frac{1}{2\pi}\left(\frac{K}{m^*}\right)^{1/2} \qquad 8.2$$

$m^* = 0.24\ m_b$ for a uniform beam of rectangular cross section [100].

Substituting m_b with ρwtl, where ρ is the material density, Eqn. 8.2 becomes

$$\nu_0 = \frac{t}{2\pi^2}\left(E/\rho\right)^{1/2} \qquad 8.3$$

therefore

$$K = 2\pi^3 l^3 w\left(\frac{\rho^3}{E}\right)^{1/2}\nu_0^3 \qquad 8.4$$

The spring constant scales with the cube of the unloaded resonance frequency. J.P.Cleveland et al. [102] suggested a simple way to estimate the spring constant by measuring the unloaded resonance frequencies. We adapted their method to calibrate the spring constants of cantilevers.

Measurement of the resonance frequency is simple. The vibrations of the lever excited by thermal oscillations are measured by the interferometer, and an Fourier Transform spectrum of the interferometer signal is recorded on a LeCroy Model 9420 oscilloscope.

Figure 8.3 shows a resonance curve of a cantilever used for Young's modulus

measurements on biological specimens. The resonance frequency is 8.475 KHz. Using the numbers provided by the manufacturer for l and w, a material density 2.2g/cm^3, and an elastic modulus 1.15x10^{11} N/m^2 for Si, the spring constant of the lever is calculated to be 0.17 N/m.

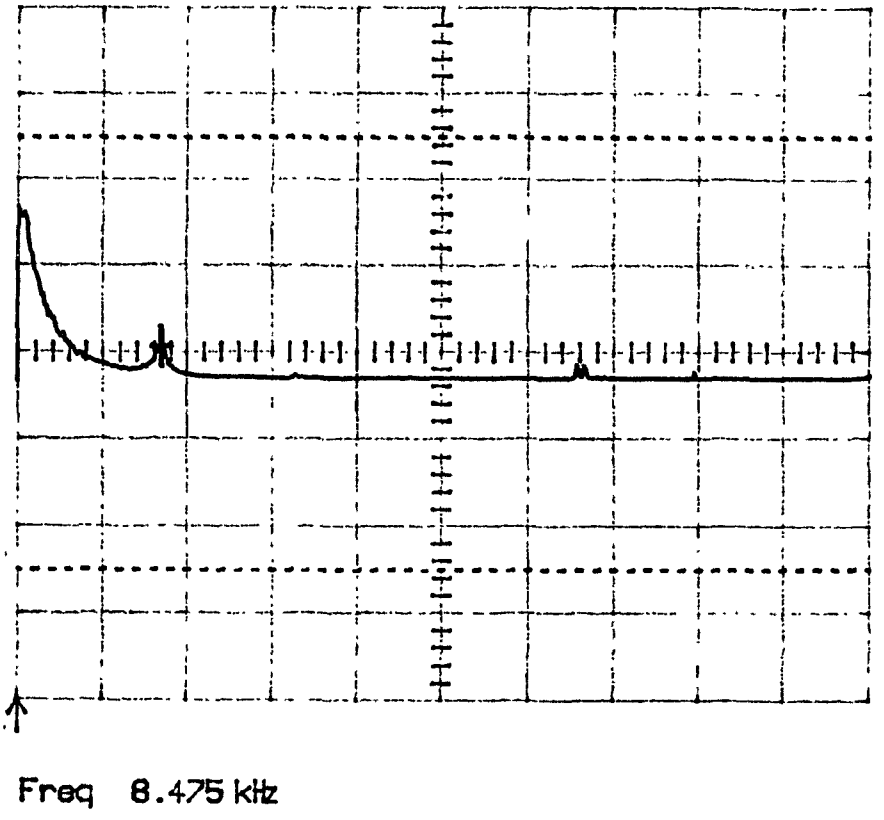

Figure 8.3: A resonance curve of a cantilever used for Young's modulus measurements. The x-axis represents the frequency and the y-axis records the optical signal which represents the cantilever's fluctuation due to thermal excitation. The resonance frequency is 8.475 KHz.

9 Materials and sample preparation

9.1 Materials

The chitin spines used here were supplied by L.Fritz of the National Research Council of Canada Institute for Marine Biosciences. The β-chitin spines are produced by the unicellular marine diatom Thalassiosira fluviatilis. The chitin spines as seen in the electron microscope are ~60 μm long, up to 100-200 nm wide, and about 50 nm thick [103]. These spines were observed to be composed of a number of macrofibres with widths of 20-30 nm and thicknesses of 18 nm. The smallest fibre seen is 3.5 x 2.0 nm, known as the elementary fibre [104]. The unit cell of the crystalline structure of the β-chitin is monoclinic with a=0.482 nm, b=1.032 nm, c=0.983 nm, and $\beta=112^0$. The b axis of the crystal is the long axis of the fibre [103]. The polymeric chains are parallel to each other, linked in a crystallographic array through hydrogen bonds between neighbouring chains [103,105]. The majority of the spines and macrofibres both in SEM and SFM images appeared straight or to have a very slight curvature [80,104], indicating the high rigidity of this crystalline structure.

The other material used was Mh sheath described in chapter 3.

9.2 Substrate

Mounting materials on a support which allows them to span over a groove and with ends firmly anchored to the support is the most critical part of this experiment.

Figure 9.1 is a sketch of the grating pattern of the GaAs substrate. These grooves were 700 nm, 500 nm, or 300 nm wide, many microns long, and 300 nm deep. Samples deposited on the grating spanned these grooves. The span distance of the material under study on a particular groove varies depending on the relative angle of the material to the groove.

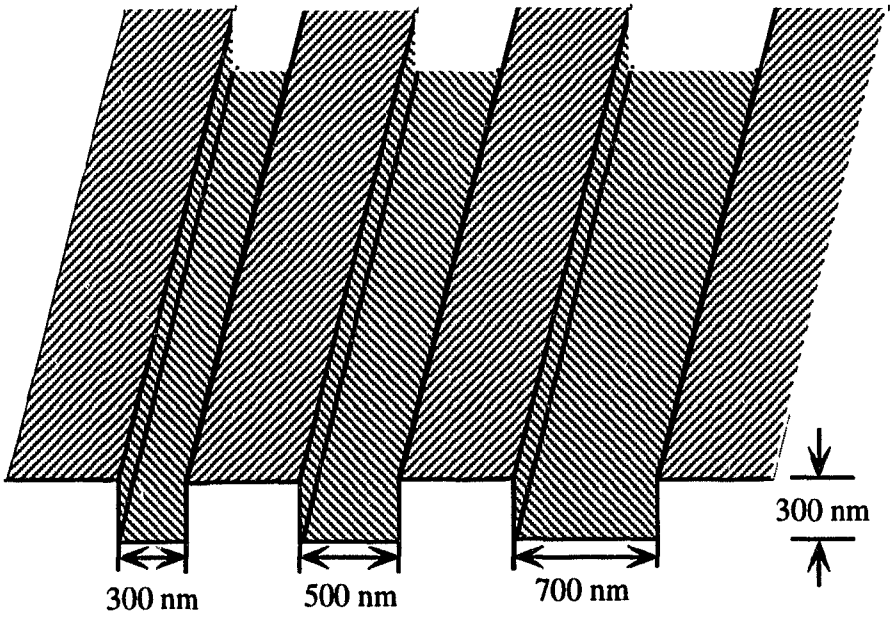

Figure 9.1: Sketch of the grating pattern of the GaAs substrate.

Therefore this grating provides an assortment of widths for different materials or the same material with different sizes. GaAs has a Young's modulus of 7×10^9 N/m^2, which is not stiff enough for providing an absolute reference for the deformation measurement. Corrections have to be made to take away the effect due to indentation of the GaAs support.

9.3 Material suspension

To prepare biological samples for SFM study, we need techniques of getting materials uniformly distributed with a high enough density such that they can be found, but do not overlap.

Chitin fibres were spread from a water suspension. The materials tended to clump when spread on a substrate from a pure suspension. Adding 5% triton to the solution made chitin fibres spread more uniformly over the substrate. A freeze-drying method was used to dry the materials on the grating.

A drop of the solution was deposited on the grating, and left for 15 mins. Most of the fibres settled on the grating during this period. Excess water in the drop was then removed with filter paper and the sample was quickly immersed in liquid nitrogen to be frozen. The sample was quickly transferred from liquid nitrogen to the cold finger of a freeze drying unit [89]. The sample was left to sublime at 1×10^{-5} torr pressure at -160 C^0 over night. The cold finger was warmed up slowly to room temperature in vacuum, and the sample was then exposed to air.

Chitin fibres prepared by this method were found well suspended over grooves of the grating. Freeze drying was thought to be necessary, because earlier experiments with optical gratings showed that the capillary force during air drying could pull the materials into the grooves. However later tests showed this was not necessary if the GaAs grating was extremely clean. Clean GaAs expels water completely, as indicated by the sharp contact angle of a water

drop placed on it. Water did not get into the grooves, and so no forces acted to pull the fibres into the grooves during the drying process. Air drying the chitin produced equally suitable samples as freeze drying.

The sheath samples were prepared by a suspension technique followed by air drying. Sheath materials were found suspended on the grooves. The ends usually remained anchored to the supports after the middle part was pushed during the measurement, although slipping of the ends did occur in a few cases.

10 Results, analysis and discussion

10.1 Chitin

10.1.1 z-piezo displacement versus force curves

Figure 10.1 is a data set of z-piezo displacement versus force (represented by the reference voltage) curves for chitin. The lower curves are the z-piezo displacements due to force on the bare substrate. The upper curves in Figure 10.1 are the z-piezo displacements over the chitin when pressing at the centre of the span. The lower curves were used as the reference to calibrate the force and deflection of chitin. A 1V change in the reference voltage moved the z-piezo ΔZ_p=25.5 nm. The spring constant of the lever was calibrated as K_c=0.17 N/m. Due to the insufficient stiffness of the GaAs substrate, the induced change in force is not simply 25.5 nm x 0.17 N/m=4.2 nN, but determined by the relationship: $\Delta Z_p=\Delta F/K_c+\Delta d$, where Δd is the change in deformation of the GaAs surface described by Eqn.7.3. However, calculations showed that the change in force can be calculated by K_c x ΔZ_p with an error of only 2-3% for all the experimental conditions used, which is negligible in comparison to the accuracy of our measurements. Therefore for all the data presented, the force was calibrated directly by the reference curve without making corrections. The net displacement in ΔZ_p, plus the indentation change of the GaAs substrate, which is 0.1 nm for the 4.2 nm force change in this case, is the deflection of the fibre, δ. Note that the suspended fiber was under load even before varying the reference voltage, so δ is actually the change in deflection of the fibre due to the change in force. The deflection is linear over the range of force used. A second or third run on the same place reproduced to the first with an error of only ~4% on chitin and GaAs support. The minimal hysteresis between the loading and unloading curves suggests that the GaAs and Chitin mainly respond elastically. In a few cases, plastic deformation did occur on both chitin and GaAs, as represented by the significant hysteresis

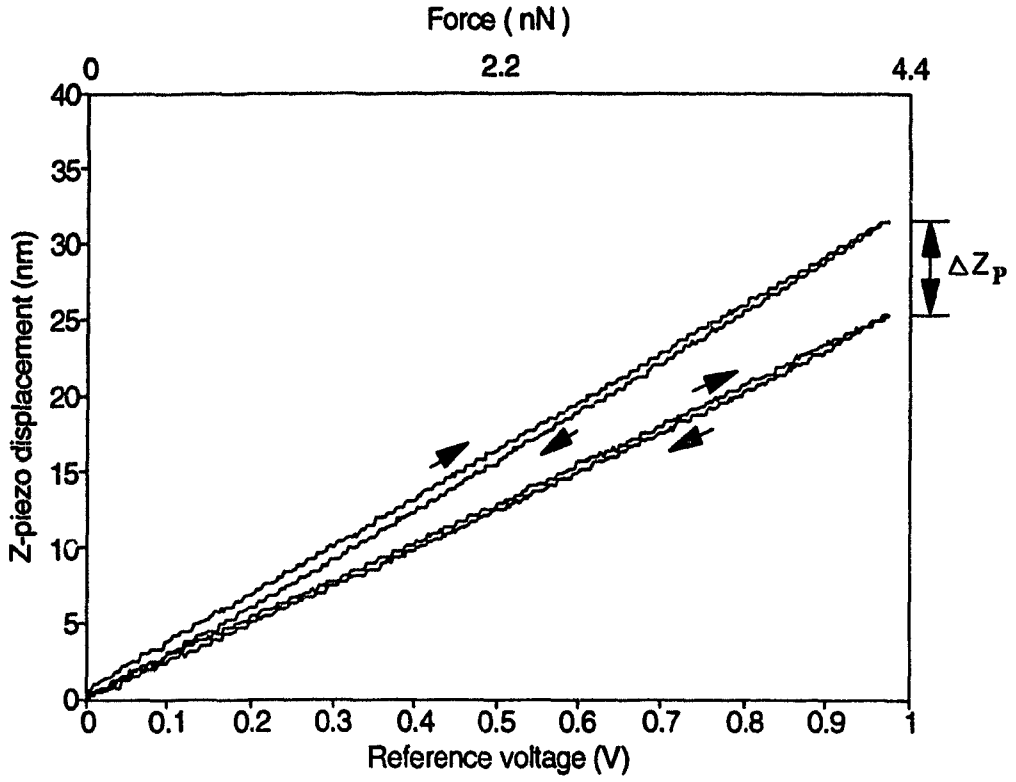

Figure 10.1: Z-piezo displacement versus force curves for chitin. The lower curves were measured on the uncovered GaAs support. The upper curves were measured when pressing at the center of the span. The net displacement in ΔZ_p plus the indentation change of the GaAs substrate is the deflection of the fibre.

on the loading and unloading force curves. Some molecular bonds breaking and the material yielding to the force could be the origin of observed hysteresis. Other possibilities such as tip slipping, defect in the material, and cantilever dependent instability could also cause the hysteresis. Since the plastic effects were not routinely observed and not reproducible, we did not investigate its origin. This type of curve was not used for calculations.

The deflection of the fibre was obtained by measuring changes in the cantilever deflection as the loading forces were varied. This meant that although capillary forces between tip and biological material can greatly increase the force the tip exerts on the top surface of the material, their effect on the deflection measurement should be minor.

10.1.2 Young's modulus

The rigidity of chitin and the small deflection relative to the length of the span suggested a beam bending model was appropriate. The ends of the beam were considered clamped rather than supported because the very long fibre (up to 60 μm) would be in contact with the substrate at many points and was not likely to flex at the ends. An evidence which supported this assumption is that no relative movement of fibres to the substrate was observed. The Young's modulus of chitin fibre was determined by analyzing the experimental data using Eqn.7.6. The dimensions of the fibres and the distances spanned were determined from the topographic images.

Figure 10.2 is a topographic image of the suspended chitin fibre used to measure the force curves in Figure 10.1. The dimensions of the fibre were measured from a cross section of the part of the fibre sitting on the grating. The measured width was corrected for errors due to convolution with the tip width. The tip radius was estimated to be 20 nm from the tip broadening effects at the edges of the grating and the sheath edges. The fibre is 150 nm wide and 60 nm high, and the longest suspended section is about 1500 nm. Using Equation 7.6,

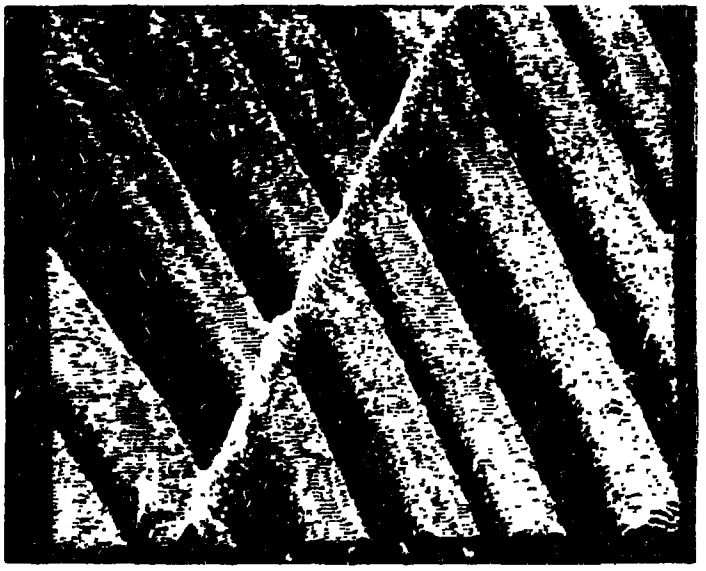

Figure 10.2: SFM image of a chitin fibre suspended over grooves in the GaAs grating. The spine has a cross-section of 150 nm x 60 nm. The image was taken at a load of 7 x 10^{-9} N with a cantilever of a spring constant 0.17 N/m. The nonstraight appearance of the grooves is an artifact of the non-linear response of the piezo drive.

the Young's modulus of this particular fibre was 3.8 x 10^9 N/m^2. Measurements on different fibres gave a range of Young's modulus from ~3 x 10^8 N/m^2 to ~1 x 10^{11} N/m^2. Spines and macrofibres had different Young's moduli. Spines had a measured Young's modulus of 3 x 10^8 to 6 x 10^9 N/m^2, while macrofibres (40 nm x 20 nm) had a larger Young's modulus of (0.5-1.5) x 10^{11} N/m^2. The larger figure is comparable to that of glass, and is of the same order as in our preliminary study which used a less sophisticated technique [80]. This rigidity is attributed to the high crystallinity of the macrofibres. The spines are composites of the macrofibres. The bonding between the macrofibres is weak, indicated by the spines fragmenting into macrofibres. The simple model of a uniform beam is not applicable to the spines but is appropriate for the macrofibres. The fact that biological specimens usually have different orders of structures with different kinds of bonding underscores the critical need for using an appropriate model for the system under consideration.

10.1.3 Structure and rigidity of the chitin fibres

The rigidity of a material is a property of its three dimensional structure. For β-chitin, this rigidity comes from the covalent bonding in the chitin chains and the hydrogen bonding between the chitin chains in the two dimensions perpendicular to the axis of the fibre. The existence of water might be important to retain the rigidity of the chitin fibres as we found from a comparative studies of chitin fibres with STM and SFM [80]. Figure 10.3 is an SFM image of chitin fibres deposited on mica. There were spines of 200 nm wide by 50-60 nm high. The macrofibres in these spines lay parallel rather than braided together, consistent with the known conformation of β-chitin. Individual macrofibres were typically 35-40 nm wide by 20 nm high. Most of the spines and macrofibres appeared rigid as they lie straight and span other fibres. Figure 10.4 is an STM image of chitin fibres. The 100 nm wide by 20 nm high spine follows the contours of the fibre bundle upon which it rests, which

Figure 10.3: 2900 nm by 2300 nm SFM image of chitin fibres on mica.

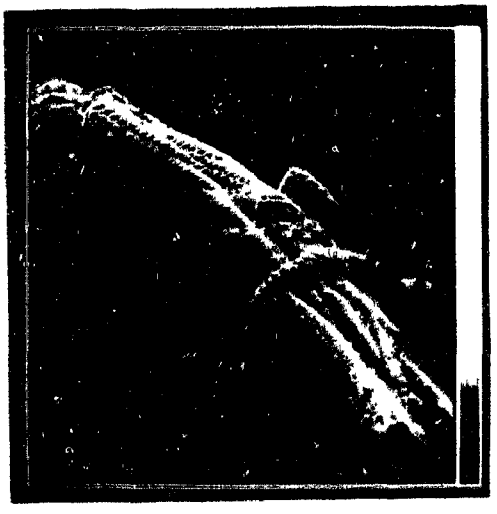

Figure 10.4: 3300 nm by 3300 nm STM image of Pt/Ir coated chitin fibres on $TaSe_2$.

was in contrast to the SFM images. STM samples had to be put under vacuum and metal coated. The evacuation may have removed water from the chitin fibres and hence disrupted the hydrogen bonds, and the fibres lost their rigidity.

In the Young's modulus measurements, both air dried and freeze dried macrofibres were rigid, and had a Young's modulus of ~1 x 10^{11} N/m^2. The freezing and subsequent vacuum sublimation may not have removed enough water molecules to provoke the disruption of the hydrogen bonds which hold chitin chains together and give the rigidity of the macrofibres. It is also possible that water re-entered these hydrophillic polysacchrides when they were exposed to air after the freeze drying process and chitins regained their rigidity.

The freeze drying process could have caused rupture of the bonds between macrofibres which made up spines and spines lost their rigidity. A freeze dried spine is a strand of many macrofibres free from bonding to each other. Because the model appears not applicable to spines as we have discussed before, we can't estimate to what level the given low value of Young's modulus of spines was attributed to the effect of the freeze drying process.

10.1.4 Uncertainties in the measurement

The output of the interferometer intensity is not a linear function of the lever deflection. In the small region around the most sensitive part of the fringe, it is approximately linear, with an error of about 4% for the ranges used in the force curve measurements. The actual error in the final result is much less than 4% because two curves (measured on a beam and on the grating) with similar errors subtracted tends to cancel the error.

The maximum deflection is obtained by pushing at the mid-point of the suspended fibre. Care was taken in the measurement to ensure the tip was sitting as close as possible to this mid-point. A multistep process was used to find the mid-point. After the measurement

site was chosen, the magnification was reduced to enlarge the area around the site. Scan speed was reduced to about 30 nm/sec (~1 μm/30 sec) before stopping the tip at the right site, to minimize the effect of piezo creep. The position error is estimated to be as large as 5% of the span of the fibre. The deflection of a clamped beam loaded anywhere between the two edges is

$$\delta(x) = \frac{1}{16}\frac{F}{wE}\frac{4x^2(3l-4x)}{t^3} \qquad 10.1$$

where x is the loading point. If a beam is loaded at a distance which is 5% off the mid point, the deflection difference compared to a mid point loaded beam is only about 1%. This is not significant.

As a further check on the position of the loading, the scan was resumed after the force curve was taken. Sometimes, the tip slipped down narrow fibres. These runs were rejected.

Contamination of the substrate surface could change the measured elastic response because the force curve measurement on the grating is simply a surface indentation measurement. A variation of about 5% was measured on different spots of the grating. This could be caused by non-uniform surface contaminations such as a water film or a residue from the suspension solution. This effect was reduced by averaging data measured on 5 different spots of the grating.

The largest error for this measurement was perhaps from substrate roughness preventing the accurate measurement of span distances. The image in Figure 10.2 shows the grating is not perfectly uniform, there are small undulating ridges. These were probably produced by the etching process. The ridges can be as high as 25 nm, and the fibre could rest on these ridges instead of the flat support. This was probably the case when pushing on the fibre over the grating produced unexpected large deformations. The measured Young's modulus on the same chitin fibres spaced over 500 nm and 700 nm differed by as much as

30%. This large error was mostly due to the uncertainties in the measurement of span distances.

10.2 Bacterial Mh sheath

10.2.1 Elastic deformation

(a) Young's modulus

Figure 10.5 shows an SFM image of two suspended sheathes. The sheath bridges the 300 nm groove with only small deflection under minimum imaging force. This image showed the sheath material had little rigidity. The sheath bends around and contours the structures underneath it in a manner similar to that of kitchen plastic wrap. The sheath is sufficiently weak that its deformation can be approximated as pure stretching.

Z-piezo displacement versus force curves of the sheath were recorded in a manner similar to those described for chitin fibres. The suspended sheath was under load even before varying the force, therefore the z-piezo displacement versus force curve gives only the change in deflection of the sheath due to the change in force. Because of the nonlinear response of the deflection to the normal force, data from the deflection change versus force change is not sufficient for analyzing the result. Absolute values of the deflection under the force were obtained by the alternative measurement technique: taking topographic images at different loading forces and measuring the deflections from the cross-sections of these images.

Figure 10.6 shows plots of F/δ versus δ^2 of the experimental data for three specific sheaths. Curve a, represented by points □, is a complete data set over a large range of force up to near the elastic limit. The data points were measured by both techniques. Figure 10.7 shows an example for measuring absolute values of the deflection under the force by taking

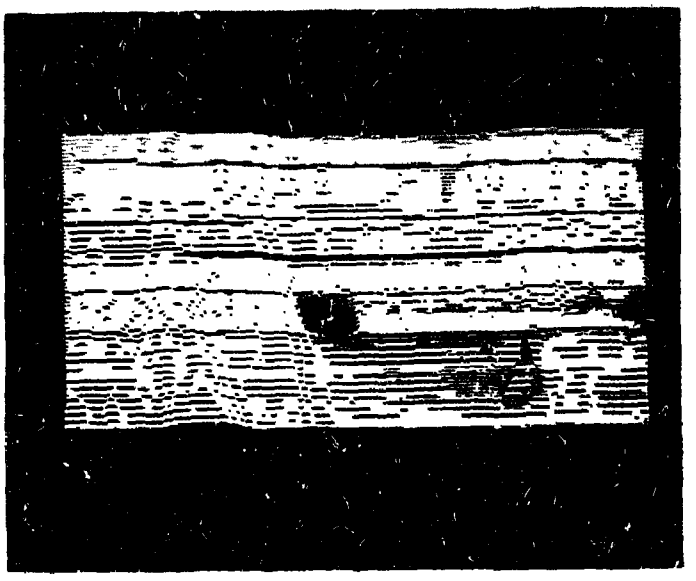

a

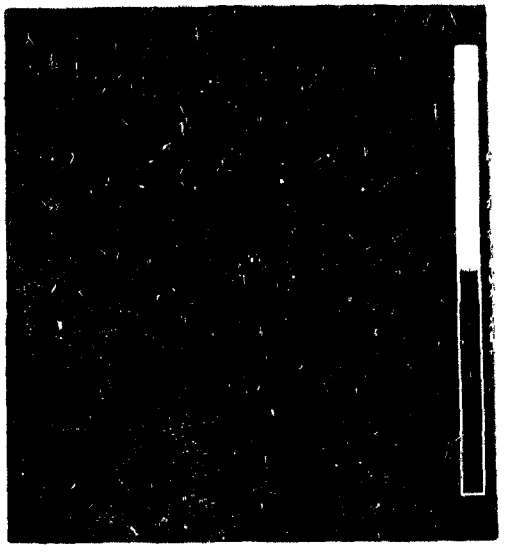

b

Figure 10.8a: Image of a sheath showing the plastic deformation induced by a force of ~2 x 10^{-7} N. 10.8b: Cross-section through the hole shows that the depth is ~30 nm, revealing the tip geometry.

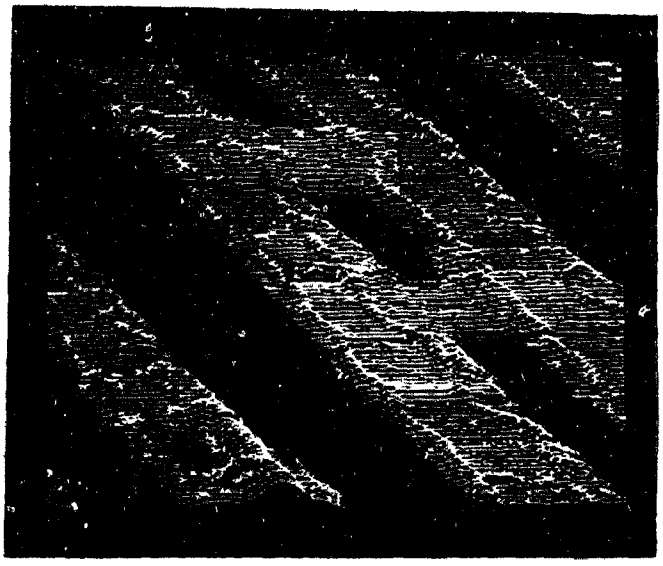

Figure 10.5: 2900 nm by 3800 nm SFM image of two sheaths suspended over a 300 nm wide gap. The imaging force was 2 x 10^{-8} N.

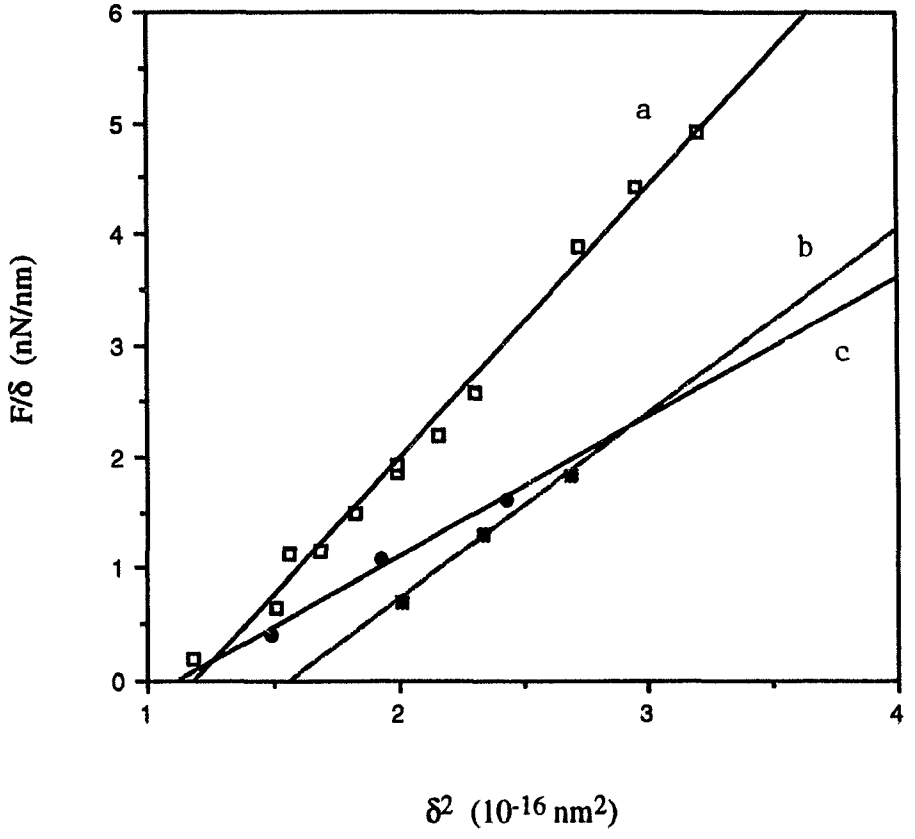

Figure 10.6: Plots of F/δ versus δ^2 of the experimental data for three specific sheaths.

a

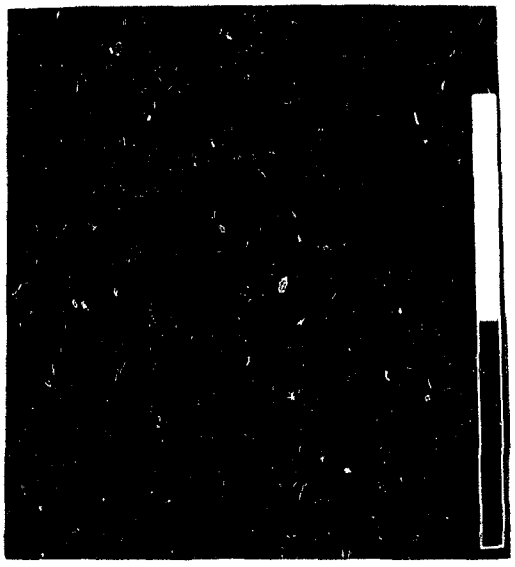

b

Figure 10.7a: SFM image of a suspended sheath stretched into the 300 nm gap by a loading force of 9 x 10^{-8} N. 10.7b: Cross-section running through the center of the sheath reveals the deflection (20 nm) of the sheath.

cross-sections. The surface indentation of GaAs under each loading force is calculated according to Eqn. 7.3 using a indenter with a radius of 40 nm (tip radius plus the thickness of the sheath), and added to the measured deflection of the center of the sheath. Deflection change versus force change is measured at every loading force by measuring z-piezo displacement versus force curves at these loading forces. The linear functional dependence of F/δ on δ^2 is evident, which agrees with the stretching model described by Eqn. 7.21. Due to the difficulties of varing the loading force continuously over large range with the interferometer type detector, measurements on some sheaths were only taken in limited ranges (as curves **b** and **c**, represented by points ■ and ●, respectively). The calculation of the elastic modulus from the slope of the curve requires a knowledge of the tip contact radius on the sheet. The tip radius was estimated to be 20 nm from the tip broadening effects at the edges of the grating and the sheath edges. For small vertical deflections, the effective tip contact radius can be much smaller. However, a roughness with an amplitude up to 3 nm (vertical corrugation) was observed on the surface of the sheath, and this limited the contact radius of the tip to the sheath surface to ~11 nm. For a contact radius range of 11 nm to 20 nm (maximum) and with $f(\theta_m)\approx 1.5$ for the geometry of the sheath, curve **a** gives a value of 11 nm for the initial sag δ_0 and a Young's modulus range of $4 - 5 \times 10^{10}$ N/m^2. Measurements on a number of sheath bridges gave a range of δ_0 values from 8 nm to 12 nm and a range of Young's modulus values $(2\text{-}5) \times 10^{10}$ N/m^2. The model gave consistent results for a variety of sheaths, forces, and gaps.

We have ignored the deflection of the sheath due to surface indention in analyzing the deflection data. According to Eqn.7.3, the indentation of the sheath under a force of 10^{-7} N (maximum force used for the elastic deformation measurements) applied by a spherical indenter of a radius 20 nm is about 0.6 nm, which is significantly smaller than the deflections we measured (20 nm). The tip contact radius resulting from this indentation is about 4 nm and is less than that caused by the roughness of the surface structure of the sheath. Therefore

the effective contact radius of the tip with the sheath surface is at least 11 nm.

(b) Spring constant of the bond between hoops

The hoop model we developed to take into account the inhomogeneous elastic properties of the sheath is based on the assumption that the bonding between hoops is much weaker than that within each hoop, i.e. the sheath fragments perpendicular to the cylinder axis to give hoops easily but is otherwise mechanically rigid. Two evidences support this assumption. First, chemical disruption treatments can break the sheath into hoops, and much more severe treatments attack the hoops [20]. Second, in an experiment of preparing sheath sample on grating with the freeze drying method, we found that the sheath fragmented along the hoop boundaries when frozen to LN temperature. As is known in molecular biology, some biopolymers have different level of structures, categorized by the forces that hold the molecules together [106]. It is reasonable to think that the sheath, hoops and individual subunits belong to three different levels of structure, and the bonding between the subunits within each hoop is much stronger than that between hoops. Then the hoop model (Figure 7.7) we proposed can be used to analyze the data in Figure 10.6.

In a 150 nm length of sheath (half the span) we can expect about 10 hoops (assuming the width of each hoop is 15 nm) and about the same number of joints. The widths of each joints in the trapezoid region and the size factor C in Eqn. 7.23 can then be determined. The calculated ratio of the spring constant to the spacing between springs, K_h/a, from Eqn. 7.22 is 2×10^{10} N/m^2. Since the sheath stretched was a double layer, the spring constant versus spring distance for the hoop bond is 1×10^{10} N/m^2. Data measured on different sheaths gave a value of this ratio from 0.4 to 1×10^{10} N/m^2.

10.2.2 Plastic deformation

The sheath responded elastically when the force was less than 10^{-7} N. On increasing the force, the sheath deformed irreversibly, and this provided an estimate for the ultimate strength of the sheath. Figure 10.8a shows a sheath on which a ~100 nm diameter hole was made at the middle by a force of ~2 x 10^{-7} N, and the rest part of the sheath remained intact. Figure 10.8b is a cross-section through the hole. The measured depth of 30 nm of the hole reflects the tip geometry. The force and deflection of the sheath at the elastic limit were $F_m \approx 10^{-7}$ N and $\delta_m \approx 20$ nm respectively. The corresponding total extension of the sheath in the half span, 150 nm, is calculated with Eqn.7.24 to be $\epsilon \approx 1.0$ nm. The extension in each joint was calculated using equation 7.25 and plotted in Figure 10.9. The gap closest to the tip extended $\epsilon_9 = 0.3$ nm while the gap closest to the support only extended $\epsilon_0 = 0.04$ nm. The total extension summed up to 1.0 nm. Therefore the hoop joint may separate by 3 angstroms before fracture of the inter-hoop bond occur.

Yield information can be used to determine absolute physical limits on internal pressures. For the K_h/a value we obtained above (0.4-1 x 10^{10} N/m^2), the maximum sustainable tension for the complete tubular sheath bacterial is $2\pi r_{sheath}(K_h/a)\epsilon_9 \sim 1.7\text{-}4.1 \times 10^{-6}$ N. This in turn implies a maximum internal pressure of 110 - 270 atmospheres. The large variation in this estimated maximum internal pressure is from the uncertainty in the measured K_h/a values, which could be due to the effect of defects in the sheath material.

We can also estimate the number of bonds per structural subunit along the circumference. The maximum elastic energy that was put into a spring in a joint is

$$\Xi = 1/2\ (K_h/a)\ \epsilon_i^{\ 2}\ a$$

where K_h/a is the ratio of the hoop bond spring constant to the distance between springs as defined before. Dissolution analysis of the sheath material suggested that the hoops were bonded covalently by disulfide chains [55]. If using an average value of 7 x 10^9 N/m^2 for K_h/a and $\epsilon_9 = 0.3$ nm for the maximum extension, and Ξ is to be a covalent bond energy,

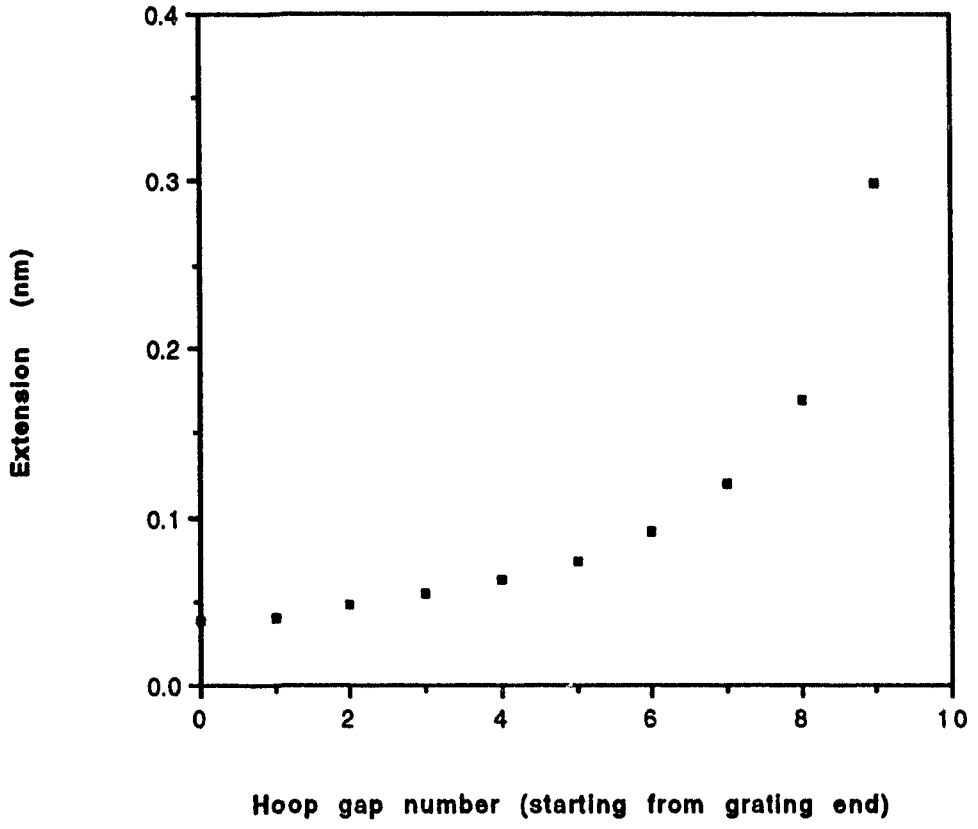

Figure 10.9: Plot of the extension of the hoop joints calculated according to the hoop model.

E~2 eV= 2 x 1.6 x 10^{-19} Joules [107], then the spring distance, a, must be ~ 1 nm. The size of the structural subunits along the circumference is ~2.8 nm. This implies there are about 3 bonds per subunit.

The area compressibility modulus, characterizing the resistance to area expansion or compression, is defined as the isotropic tension per unit length versus unit fractional change in area [88]. For a critical force of 10^{-7} N and a maximum deflection of 20 nm, the critical tension in the sheath is $T_m=F/2 \times (L_0/\delta_m) \sim 3.7 \times 10^{-7}$ N. This tension applied in a width of w_t of ~80 nm (the width of the gap closest to the tip in the hoop model) gives a maximum tension per unit length of ~2 N/m (for single layer), and this maximum tension per unit length produced a fractional change in area of ~2 x 10^{-2} (0.3 nm maximum extension per hoop spacing 15 nm) assuming the width of sheath did not change, the area compressibility is then estimated to be 100 N/m.

10.2.3 Discussion

The Young's modulus analyzed from the homogeneous trapezoidal model of the stretching response of sheath is (2-5) x 10^{10} N/m^2, which is very stiff compared with other biological materials measured by the surface indentation method [77]. Langmuir-Blodgett films are an example of well ordered polymeric films. The elastic constants of LB films formed from cadmium salts of the fatty arachidic acid have been determined by a Brillouin scattering experiment [108]. They are between 4 x 10^8 and 2.1 x 10^{10} N/m^2, and the elastic constant corresponding to the stretching in the film plane is ~1 x 10^{10} N/m^2. Our result for sheath is reasonable considering that sheath is not a usual cell membrane, but is instead a rigid cell envelope built out of covalently linked polymeric peptidoglycan.

The area compressibility, 100 N/m, estimated from critical values for the sheath, is about two and half orders of magnitude greater than that of the red blood cell membrane (~2

x 10^{-1} N/m) measured by micropipette aspiration [88], and the erythrocyte membrane (1-3 x 10^{-1} N/m) measured by cell poking [86]. Bacteria are known to be able to sustain high osmotic pressure. For example, the internal osmotic pressure for E-coli is 3-5 atm [109]. The basis of the ability of bacteria to withstand such stresses has been understood: unlike animal cells, most bacteria contain a very strong cell wall which resists the pressure build-up that would otherwise rip the cell apart [110]. The cell wall is built of some of the strongest material formed with covalent bonds [111]. Our result implies that a three orders of magnitude larger force is required to produce the same extension in sheath than in animal cell membranes. This is no surprise considering that the membranes are composed of short fatty-acid chains that self-assemble into sheets under the influence of hydrophobic and hydrophillic interactions while the sheath is composed of covalently bonded peptidoglycan chains.

The maximum internal pressure of the Mh organism was estimated to be ~200 atm, more than 20 times higher than the usual osmotic pressure involved in normal cell function. The sheath is an envelop outside the cell walls, it has to be very strong to function to maintain the integrity of the bacterium organism, and to function as a sieve to exclude large molecules [20]. All the studies conducted on sheath have shown the unusual stability and strength of this material.

The uncertainties in the measurement discussed in the chitin fibre measurements are also relevant to the measurements on sheath. The value of the elastic modulus derived from the data depends on the choice for the contact radius between the tip and sheath. Depending on how the sheath deforms around the tip, the contact radius may be comparable to the tip radius in an extreme case. However, the calculated Young's modulus only depends logarithmically on the contact radius and thus could be affected by 30% at most. Capillary forces were not included in Figure 10.6, and therefore not in the calculations. As is explained in chapter 7, although capillary forces can greatly increase the force the tip exerts on the top surface of the material under the tip apex, they are balanced by the attractive forces between

the tip and surface at the vicinities of the contact and therefore do not add to the loading force which deflects the material. Their effect is rather to bring the material to deform around the tip and therefore change the contact area. The capillary force between a spherical tip and a surface in contact is given by $F=4\pi R\gamma\cos\Theta$, where R is the radius of curvature, Θ the contact angle and γ the surface tension coefficient [91]. For a tip radius of 20 nm we obtain a maximum force $F_{max}=1.8 \times 10^{-8}$ N. An estimate showed that a capillary force of 1.8×10^{-8} N can produce a deformation of the sheath around the tip, with a contact radius of ~6 nm. We have pointed out earlier that the contact radius is limited to ~11 nm by the roughness of the sheath surface and we have also allowed a large uncertainty on the contact radius (11 nm - 20 nm) in the calculation, therefore the effect of capillary forces should not introduce larger errors than quoted.

Not discussed above are the difficulties involved in preparing suitable materials for this SFM technique. Each new material being studied has unique properties and preparation techniques must be developed for each one. The material of interest must be removed from other biological material present and reduced to sub-micro size. The purification of the sample is particularly critical because contamination may co-deposit with the material of interest. The dimensions of the sample, the width of the gaps on the GaAs substrate, and the force constant of the cantilever must all be matched to allow for a suitable span of material and a depression into the gap. Also, the adhesion between a particular material and the support has to be strong enough to anchor the ends of the material.

11 Conclusion and future studies

A new technique to measure elastic properties by bending or stretching material on microscopic grooves etched in a GaAs substrate has been developed. This technique, and suitable models yielded reproducible measurements of the elastic and plastic parameters of two biological materials, β-chitin fibres and the S-layer sheath of the archeobacterium *Methanospirillum hungatei*. This work demonstrated the possibility of obtaining elastic properties of relatively small biological materials and giving insight into possible biological mechanisms from the material bending and stretching measurements.

The β-chitin behaved as an elastic material, and the measurements gave a range of values of 3×10^8 to 1×10^{11} N/m^2 for the Young's modulus, depending on the size of the fibre. Chitin fibres with cross sections less than 40 nm x 20 nm had a Young's modulus of $(0.5\text{-}1.5) \times 10^{11}$ N/m^2, which is comparable to that of glass ($0.5\text{-}0.7 \times 10^{11}$ N/m^2), and several orders of magnitude larger than that of cartilage, $0.16\text{-}0.6 \times 10^6$ N/m^2, reported by Weisenhorn [77]. We have consistently found that β-chitin is a very stiff material: the fibres are straight or have only a very slight curvature on SEM and SFM images; they freely span a distance of microns without significant deflection; and they have large Young's modulus values. We have also resolved a ~1 nm period structure with SFM, which corresponds to the known crystalline periodicity of chitin chains along the b axis [80]. The high imaging resolution achieved is also believed due to the high rigidity of the material. This rigidity is attributed to the high crystallinity of the microfibres. The bacterial sheath behaved elastically below a limiting stretching force. In the homogeneous approximation, the Young's modulus was $(2\text{-}5) \times 10^{10}$ N/m^2. According to the inhomogeneous hoop model, the ratio of the spring constant to the distance between springs of the hoop bond was calculated to be $(0.4\text{-}1) \times 10^{10}$ N/m^2. Plastic deformation of sheath was also investigated and used to provide information on the ultimate strength of the material. We estimated the physical limits on internal pressure

of the Mh organism and the extension of the hoop bonds. The maximum internal pressure was estimated to be as high as 200 Atm, which corresponds to a maximum extension of 0.3 nm at each hoop joint under a maximum tensile force per unit length of 2 N/m. The area compressibility modulus, 100 N/m, characterizing the resistance to area expansion or compression, is two and half orders of magnitude greater than that of the red blood cell membrane measured by micropipette aspiration and the erythrocyte membrane measured by cell poking.

The accuracy of the method for determining the elastic constant of a biological material depends on the type of material investigated and to the extent to which the various assumptions apply. For both chitin and Mh sheath, the calculated Young's moduli varied by a factor of ~3. Although this represents a large uncertainty, the elastic properties of biological material at the nanometer scale are difficult to obtain and determination of the modulus to an order of magnitude is often of interest. For example, Weisenhorn et al. [71] reported large variations (a factor of four) of the elastic modulus for rubber and cartilage obtained with the indentation method.

The overall objective of this work was to validate the measurement, by this bending or stretching method, of the elastic properties of biological materials. Although the measurements and analysis provided consistent results on both β-chitin fibres and the S-layer sheath of Mh, an independent, accurate method to determine the similar parameters is lacking. The experiment was done only on relatively simple biological systems and at certain conditions. There are still a number of aspects that depend on assumptions and models. Some further studies can be conducted in future to provide more detailed information about the interpretation of the data and a better understanding of biological mechanisms.

(a) Use gratings be made with Si, which is considerably stiffer than GaAs. Corrections for the indentation of the reference surface will then be unnecessary, and this will improve the accuracy of the measurement.

(b) Improve the modelling for the stretching of the sheath in order to obtain a more quantitative estimation of the elastic properties.

(c) Perform same measurements under an aqueous solution containing the buffer salts present on a living organism. Comparison of results with those from measurements in air may yield important clues concerning how the environment alters the mechanical properties of these materials. As is known in biochemistry, in a dry environment a larger amount of energy is needed to rupture certain bonds than in a wet environment [109]. The very high values of the yield strength of the sheath measured in this experiment could be a result of this effect. Measuring biological properties in situ is the eventual goal.

(d) Extend the elasticity measurement to whole cells or organisms. The mechanical properties of cell components may be different when they are separated from their cells as compared to when they perform normal cell function. The simple indentation technique has to be chosen to measure on cells and a more complicated mechanical analysis has to be used to extract useful information about the elastic modulus.

(e) Use this technique to study materials with known Young's moduli to test the technique as well as the models used. At the present stage we do not have a suitable system for this test. The dimensions of the sample, and the width of the gaps must be matched to allow for a suitable span of material and a depression into the gap.

This technique was developed for measuring the mechanical properties of biological materials, but it is suitable for any materials because it does not require the material to be softer than the substrate. This new technique could be applied to smaller structures if smaller width grating grooves can be manufactured. We hope that this technique will encourage the development of cell biology and nanotechnology to a more microscopic scale.

Bibliography

[1] G.Binnig, H.Rohrer, Ch.Gerber and E.Weibel. Tunneling through a controllable vacuum gap. *Appl. Phys. Lett.*, 40:178, 1982.

[2] G.Binnig, H.Rohrer, Ch.Gerber and E.Weibel. *Phys. Rev. Lett.*, 49:57, 1982.

[3] G.Binnig and H.Rohrer. Scanning tunneling microscopy. In Trends in physics. *European Physical Society*, 38-46, 1984.

[4] A.M.Baro, R.Miranda, .Alaman, N.Garcia, G.Binnig, H.Rohrer, Ch.Gerber, and L.Carrascosa. *Nature*, 315:253, 1985.

[5] K.A.Fisher, K.C.Yanagimoto. Scanning tunneling microscopy of planar biomembranes. *Ultramicroscopy*, 33:117-126, 1990, and references therein.

[6] B.L.Blackford, M.H.Jericho and P.J.Mulhern. A review of scanning tunneling microscopy and atomic force microscopy imaging of large biological structures: Problems and prospects. *Scanning Microscopy Intl.*, 5:907-1006, 1991, and references therein.

[7] H.Fuchs, S.Akari, K.Dransfeld. Molecular resolution of Langmuir-Blodgett monolayers on tungsten diselenide by scanning tunneling microscopy. *J. Phys.* B80:389-392, 1990.

[8] E.D.C.Chidsey, D.N.Loiacono, T.Sleator, and S.Nakahara. STM study of the surface morphology of gold on mica. *Surf. Sci.*, 200:45-66, 1988.

[9] A.Putnam, B.L.Blackford, M.H.Jericho, and M.O.Watanabe. Surface smoothness study of gold deposited on mica using scanning tunneling microscopy-Effect of mica temperature. *Surf. Sci.*, 217:276-288, 1989.

[10] S.M.Lindsay and B.Barris. Imaging Deoxyribose Nucleic acid molecules on a metal surface under water by scanning tunneling microscopy. *J. Vac. Sci. Technol.*, A6:544-547, 1988.

[11] J.Schneir, O.Marti, G.Remmers, D.Gläser, R.Sonnenfeld, B.Drake, and P.K.Hansma. Scanning tunneling microscopy and atomic force microscopy of the liquid-solid interface. *J. Vac. Sci. Technol.*, A6:283-286, 1988.

[12] A.Stemmer, R.Reichelt, A.Engel, J.R.Rosenbusch, J.Ringger, H.R.Hidber, and H.-J.Günterodt. *Surf. Sci.*, 181:394, 1987.

[13] R.Guckenberger, B.Hacker, T.Hartmann, T.Scheybani, Z.Wang, W.Wiegräbe, and W.Baumeister. Imaging of uncoated purple membrane by scanning tunneling microscopy. *J. Vac. Sci. Technol.*, B9:1227-1230, 1991.

[14] M.Amrein, R.Durr, A.Stasiak, H.Gross, and G.Travaglini. Scanning tunneling microscopy of uncoated recA-DNA complexes. *Science*, 243:1708-1711, 1989.

[15] A.Cricenti, S.Selci, A.C.Felici, R.Generosi, E.Gori, W.Djaczenko, and G.Chiarotti. Molecular structure of DNA by scanning tunneling microscopy. *Science*, 245:1226-1227, 1989.

[16] T.E.Wilson, M.N.Murry, D.F.Ogletree, M.D.Bednarski, C.R.Cantor, and M.B.Salmeron. Scanning tunneling microscopy at high gap resistances and on chemically modified silicon surfaces. *J. Vac. Sci. Technol.*, B9:1171-1176, 1991.

[17] W.M.Heckl, K.M.R.Kallury, M.Thompson, Ch.Gerber, H.Horber, and G.Binnig. *Langmuir*, 5:1433, 1989.

[18] M.H.Jericho, B.L.Blackford, and D.C.Dahn. Scanning tunneling microscope imaging technique for weakly bonded surface deposits. *J. Appl. Phys.*, 65:5237-5239, 1989.

[19] M.H.Jericho, B.L.Blackford, and D.C.Dahn, C.Frame, and D.Maclean. Scanning tunneling microscopy of uncoated biological material. *J. Vac. Sci. Technol.*, A8:661-666, 1990.

[20] T.J.Beveridge, G.Southam, M.H.Jericho, and B.L.Blackford. High-resolution topography of the S-layer sheath of the archaebacterium Methanospirillum hungatei provided by scanning tunneling microscopy. *J. Bacteriol.*, 172:6589-6595, 1990.

[21] V.Elings. Tapping mode atomic force microscopy. *Abstracts of Papers of the American Chemical Society.*, 207:107, 1994.

[22] T.Shibata-Seki, W.Watanabe, and J.Masai. Imaging of cells with atomic force microscopy operated at a "tapping mode". *J. Vac. Sci. Technol.*, B12:1530-1534, 1994.

[23] M.Amrein, R.Dürr, H.Winkler, G.Travaglini, R.Wepf, and H.Gross. STM of freeze-dried and Pt/Ir/C coated bacteriophage T4 polyheads. *J. Ultra. Struct. and Mol. Struct. Res.*, 102:170-177, 1989.

[24] R.Wepf, M.Amrein, U.Bürkli, and H.Gross. Platinum-iridium-carbon, a high resolution shadowing material for TEM, STM, and SEM of biological macromolecular structures. *J. Microscopy*, 163:51-64, 1991.

[25] M.Amrein, A.Stasiak, H.Gross, E.Stoll, and G.Travaglini. Scanning tunneling microscopy of recA-DNA complexes coated with a conducting film. *Science*, 240:514-516, 1988.

[26] R.Guckenberger, W.Wiegräbe, and W.Baumeister. Scanning tunneling microscopy of biomacromolecules. *J. Microscopy*, 152:795-802, 1989.

[27] B.L.Blackford, M.O.Watanabe, M.H.Jericho, and D.C.Dahn. STM imaging of the complete bacterial cell sheath of Methanospirillum hungatei. *J. Microsc.*, 152:237-243, 1988.

[28] B.L.Blackford, M.O.Watanabe, D.C.Dahn, M.H.Jericho, G.Southam, and T.J.Beveridge. The imaging of a complete biological structure with the scanning tunneling microscope. *Ultramicroscopy*, 26:427-433, 1989.

[29] S.M.Lindsay, Y.Li, J.Pan, T.Thundat, L.A.Nagahara, P.Oden, J.A.DeRose, and U.Knipping. Studies of the electrical properties of large molecular adsorbates. *J. Vac. Sci. Technol.*, B9:1096-1101, 1991.

[30] R.Garcia, D.Keller, J.Panitz, and D.G.Bear. Imaging of metal-coated biological samples by scanning tunneling microscopy. *Ultramicroscopy*, 27:367-374, 1989.

[31] M.Stewart, T.J.Beveridge, and G.D.Sprott. Crystalline order to high resolution in the sheath of Methanospirillum hungatei: a cross-beta structure. *J. Mol. Bio.*, 183:509-515, 1985.

[32] G.D.Sprott, T.J.Beveridge, G.B.Patel, and G.Ferrante. Sheath disassembly in Methanospirillum hungatei GP1. *Can. J. Microbiol.*, 32:847-854, 1986.

[33] B.L.Blackford, M.H.Jericho, P.J.Mulhern, C.Frame, G.Southam, and T.J.Beveridge. Scanning tunneling microscope imaging of hoops from the cell sheath of the bacteria Methanospirillum hungatei and atomic force microscope imaging of complete sheaths. *J. Vac. Sci. Technol.*, B9:1242-1247, 1991.

[34] R.W.Keller, D.D.Dunlap, C.Bustamante, and D.J.Keller. Scanning tunneling microscopy images of metal-coated bacteriophages and uncoated, double-stranded DNA. *J. Vac. Sci. Technol.*, A8:706-712, 1990.

[35] R.Emch, X.Clivaz, C.Taylor-Denes, P.Vaudaux, and P.Descouts. Scanning tunneling microscope for studying the biomaterial-biological tissue interface. *J. Vac. Sci. Technol.*, A8:655-658, 1990.

[36] K.A.Fisher, S.L.Whitfield, R.E.Thomson, K.C.Yanagimoto, M.G.L.Gustafsson, and

J.Clarke. Measuring changes in membrane thickness by scanning tunneling microscopy. *Biochimica et Biophysica Acta*, 1023:325-334, 1990.

[37] Z.Wang, T.Hartmann, W.Baumeister, and R.Guckenberger. *Proc. Nat. Acad. Sci. USA* 87:9343-9347, 1990.

[38] J.A.Zasadzinski, J.Schneir, J.Gurley, V.Elings, and P.K.Hansma. Scanning tunneling microscopy of freeze-fracture replicas of biomembranes. *Science*, 239:1013-1014, 1988.

[39] B.L.Blackford and M.H.Jericho. A metallic replica/anchoring technique for scanning tunneling microscope or atomic force microscope imaging of large biological structures. *J. Vac. Sci. Technol.*, B9:1253-1258, 1991.

[40] J.G.Simmons. Generalized formula for the electric tunnel effect between similar electrodes separated by a thin insulating film. *J. Appl. Phys.*, 34:1739, 1963.

[41] N.Garcia, C.Ocal, and F.Flores, *Phys. Rev. Lett.*, 50:2002, 1983.

[42] E.Stoll, A.Baratoff, A.Selloni, and P.Carnevali. *J. Phys.* C17:3073, 1984.

[43] J.Bardeen. Tunneling from a many-particle point of view. *Phys. Rev. Lett.*, 6:57, 1961.

[44] I.Giaever. Energy gap in superconductors measured by electron tunneling. *Phys. Rev. Lett.*, 5:147-148, 1960.

[45] J.Tersoff and D.R.Hammann. Theory and application for the scanning tunneling microscope. *Phys. Rev. Lett.*, 50:1998-2001, 1983.

[46] A.Baratoff. Theory of scanning tunneling microscopy (STM). *Europhys. Conf. Abstracts*, 7B:364-367, 1983.

[47] N.D.Lang. Resistance of a one-atom contact in the scanning tunneling microscope. *Phys. Rev.* B36:8173, 1987.

[48] J.Tersoff and D.R.Hamann. Theory of the STM. *Phys. Rev.* B31:805, 1985.

[49] R.J.Hamers, R.M.Tromp, and J.E.Demuth. Surface electronic structure of Si (111)-7 x 7 resolved in real space. *Phys. Rev. Lett.*, 56:1972, 1986.

[50] J.M.Soler, A.M.Baro, N.Garcia, and H.Rohrer. Interaction forces in STM: giant corrugation of the graphite surface. *Phys. Rev. Lett.*, 57:444-447, 1986.

[51] H.J.Mermin, E.Ganz, D.W.Abraham, R.E.Thomson, and J.Clarke. Contamination-mediated deformation of graphite by STM. *Phys. Rev.* B34:9015-9018, 1986.

[52] J.H.Coombs and J.B.Pethica. Properties of vacuum tunneling current: Anomalous barrier heights. *IBM J. Res. Develop.*, 30:455-459, 1986.

[53] J.Tersoff and N.D.Lang, *Phys. Rev. Lett.*, 65:1132, 1990.

[54] T.J.Beveridge, M.Stewart, R.J.Doyle, and G.D.Sprott. Unusual stability of the Methanospirillum hungatei sheath. *J. Bacteriol.*, 162:728-737, 1985.

[55] G.Southam and T.J.Beveridge. Dissolution and immunochemical analysis of the sheath of the archaeobacterium Methanospirillum hungatei GP1. *J.Bacteriol.*, 6213-6222, 1991.

[56] G.Southam, M.Firtel, B.L.Blackford, M.H.Jericho, W.Xu, P.J.Mulhern, and T.J.Beveridge. Transmission electron microscopy, scanning tunneling microscopy, and atomic force microscopy of the call envelop layers of the archaebacterium Methanospirillum hungatei GP1. *J. Bacteriol.*, 175(7):1946-1955, 1993.

[57] T.J.Beveridge, G.D.sprott, and P.Whippey. Ultrastructure, inferred porosity, and gram-staining character of Methanospirillum hungatei filament termini describe a unique cell permeability for this archaeobacterium. *J. Bacteriol.*, 173:130-140, 1991.

[58] Made at Dalhousie University, Department of Physics.

[59] B.L.Blackford and M.H.Jericho. Simple two-dimensional piezoelectric micropositioner for STM. *Rev. Sci. Instrum.*, 61:182, 1990.

[60] Ch.Renner, Ph.Niedermann, A.D.Kent, and O.Fischer. *Rev. Sci. Instrum.*, 61:965, 1990.

[61] EBL Co. East Hartford, Ct. 06108, U.S.A.

[62] Made at Dalhousie University. HV op amps:PA88 by Apex Microtechnology Corp.

[63] Materials Analytical Services. Raleigh, NC 27607, U.S.A.

[64] B.Hacker, A.Hillebrand, T.Hartmann, and R.Guckenberger. Preparation and characterization of tips for scanning tunneling microscopy of biological specimens. *Ultramicroscopy*, 42-44:1514-1518, 1992.

[65] M.Firtel, G.Southam, G.Haraus, and T.J.Beveridge. The organization of the

paracrystalline multilayered spacer-plugs of Methanospirillum hungatei. *J. Structral Biology*, 112:60-171, 1994.

[66] K.L.Westra, A.W.Mitchell, and D.J.Thomson. Tip artifacts in atomic force microscope imaging of thin film surfaces. *J. Appl. Phys.*, 74(5):3808-3810, 1993.

[67] M.Amrein and H.Gross. STM of biological macromolecular structures coated with a conducting film. *Scanning Microscopy Intl.*, 6:335, 1992.

[68] R.C.Jaklevic, L.Elie, Weidian Shen, and J.T.Chen. Application of the scanning tunneling microscope to insulating surface. *J. Vac. Sci. Technol.*, A6(2):448-453, 1988.

[69] D.J.Thomson. Resolution of the atomic force microscope. Submitted to *Scanning Microscopy International*, 1994.

[70] G.Binnig, C.F.Quate, and Ch.Gerber. Atomic force microscope. *Phys. Rev. Lett.*, 56:930-933, 1986.

[71] T.R.Albrecht and C.F.Quate. *J. Vac. Sci. Technol.*, A6:271, 1988

[72] F.Ohnesorge and G.Binnig. True atomic resolution by atomic force microscopy through repulsive and attractive forces. *Science*, 260:1451-1456, 1993.

[73] H-J.Butt. Measuring electrostatic, van der Waals, and hydration forces on electrolyte solutions with an atomic force microscope. *Biophys. J.*, 60:1438-1444, 1991.

[74] N.A.Burnham and R.J.Colton. Measuring the nanomechanical properties and surface forces of materials using an atomic force microscope. *J. Vac. Sci. Technol.*, A7(4):2906-2913, 1989.

[75] A.L.Weisenhorn, J.E.MacDougall, S.A.C.Gould, S.D.Cox, W.S.Wise, J.Massie, P.Maivald, V.B.Elings, G.D.Stucky, and P.K.Hansma. *Science*, 247:1330, 1990.

[76] W.Häberle, J.K.H.Hörber, F.Ohnesorge, D.P.E.Smith and G.Binnig. In situ investigations of single living cells infected by viruses. *Ultramicroscopy*, 42-44:1161-1167, 1992.

[77] A.L.Weisenhorn, M.Khorsandi, S.Kasas, V.Gotzos and H-J.Butt. Deformation and height anomaly of soft surfaces studied with an AFM. *Nanotechnology* submitted.

[78] P.Maivald, H.J.Butt, S.A.C.Gould, C.B.Prater, B.Drake, J.A.Gurley, V.B.Elings, and

P.K.Hansma. Using force modulation to image surface elasticities with the atomic force microscope. *Nanotechnology*, 2:103-106, 1991.

[79] M.Radmacher, R.W.Tillmann, and H.E.Gaub. Imaging viscoelasticity by force modulation with the atomic force microscope. *Biophys. J.*, 64:735-742, 1993.

[80] M.H.Jericho, P.J.Mulhern, W.Xu, B.L.Blackford, and L.Fritz. SFM and STM imaging of β-chitin. *SPIE 1855 Scanning Probe Microscopies* II:48-56, 1993.

[81] J.Vensenka, M.Guthold, C.L.Tang, D.Keller, C.Delaine, and C.Bustamante. Substrate preparation for reliable imaging of DNA molecules with the scanning force microscope. *Ultramicroscopy*, 42-44:1243-1249, 1992.

[82] H.G.Hansma, J.Vesenka, C.Sxeigrist, G.Kelderman, R.Morrett, R.L.Sinsheimer, V.Elings, and C.Bustamante. Reproducible imaging and dissection of plasmid DNA under liquid with the atomic force microscope. *Science*, 256:1180-1184, 1992.

[83] M.Egger, F.Ohnesorge, A.L.Weisenhorn, S.P.Heyn, B.Drake, C.B.Prater, S.A.C.Gould, P.K.Hansma, and H.E.Gaub. Wet lipid-protein membranes imaged at submolecular resolution by atomic force microscopy. *J. Struct. Biol.*, 103:89-94, 1990.

[84] D.Anselmetti, R.Lüthi, E.Meyer, M.Dreier, T.Richmond, J.Frommer, and H.-J.Güntherodt. Biological materials studied with dynamic force microscopy. *J. Vac. Sci. Technol.* B12(3):1500-1503, 1994.

[85] M.Fritz, M.Radmacher, and H.E.Gaub. In vitro activation of human platelets triggered and probed by atomic force microscopy. *Experimental cell research*, 205:187-190, 1993.

[86] B.Daily, E.L.Elson, and G.Zahalak. Cell poking: Determination of the elastic area compressibility modulus of the erythrocyte membrane. *Biophys. J.*, 45:671-682, 1984.

[87] R.Tran-Son-Tay. Techniques for studying the effects of physical forces on Mammalian cells and measuring cell mechanical properties. In *physical forces and the mammalian cell ed. J.A.Frangos.* Academic press, Harcourt Brace Jovanovich Publishers, 1993.

[88] E.A.Evans, R.Waugh, and L.Melnik. Elastic area compressibility modulus of red cell membrane. *Biophys. J.*, 16:585-595, 1976.

[89] A.George. Elastic effects and tunneling forces in scanning tunneling microscopy.

Master's thesis, Dalhousie University, 1993.

[90] N.A.Burnham and R.J.Colton. Force microscopy. In *Scanning tunneling microscopy and spectroscopy*. Ed: D.A.Bonnell. VCH, New York, 1993.

[91] E.Meyer and H.Heinzelmann. Scanning force microscopy. In Springer series in surface sciences, 28. *Scanning tunneling microscopy II*. Eds:R.Wiesendange, and H.-J.Guntherrodt.

[92] H.Hertz and J.R.Angew. *Math.*, 92:156, 1882; K.L.Johnson. *Proc. Instn. Mech. Engl.*, 196:363, 1982.

[93] L.D.Landau and E.M.Lifshitz. *Theory of elasticity*. Pergamon Press, Addison-Wesley Publishing Company Inc., 1975.

[94] S.Timoshenko. *Theory of elasticity*. McGraw-Hill Book Company Inc. 1934.

[95] B.L.Blackford, W.Xu, M.H.Jericho and P.J.Mulhern, M.Firtel and T.J.Beveridge. Direct observation by scanning tunneling microscopy of the two-dimensional lattice structure of the S-layer sheath of the archaeobacterium Methanospirillum hungatei GP1. *Scanning Microscopy Intl.*, submitted.

[96] M.H.Jericho et al. To be published.

[97] P.J.Mulhern, T.Hubbard, C.S.Arnold, B.L.Blackford, and M.H.Jericho. A scanning force microscope with a fibre-optic-interferometer displacement sensor. *Rev. Sci. Instrum.*, 62(5):1280-1284, 1991.

[98] M.H.Jericho, D.C.Dahn, and B.L.Blackford. Scanning tunneling microscope with micrometer approach and thermal compensation. *Rev. Sci. Instrum.*, 58(8):1349-1352, 1987.

[99] Calculated from the elastic constants provided in *American Institute of physics handbook*, 2nd edition. McGraw-Hill, 1963.

[100] W.F.Stokey. In *Shock and vibration handbook*. 7.1-7.44. McGraw-Hill, New York, 1989.

[101] T.R.Albrecht, S.Akamine, T.E.Carver, and C.F.Quate. *J. Vac. Sci. Technol.*, A8:3386, 1990.

[102] J.P.Cleveland and S.Manne. A nondestructive method for determining the spring constant of cantilevers for scanning force microscopy. *Rev. Sci. Instrum.*, 64(2):403-

405, 1993.

[103] N.E.Dweltz and J.R.Colvin, and A.G.McInnes. Studies of chitin (β-(1→4)-linked z-acetamido-z-deoxy-D-glucan) fibres of the diatom Thalassiosira fluviatilis, hustedt.III. The structure of chitan from x-ray diffraction and electron microscope observations. *Can. J. Chem.*, 46:1513-1521, 1968.

[104] K.H.Gardner and J.Blackwell. The substructure of crystalline cellulose and chitin mecrofibrils. *J. Polymer. Sci.*, part C, 36:327-340, 1971.

[105] J.Blackwell. *Biopolymers. 7:281, 1969.*

[106] R.C.Cantor, and P.R.Schimmel. *Biophysical chemistry.* Part I: The conformation of biological macromolecules. Ed:W.H.Freeman, San Francisco, 1980.

[107] C.Kittle. 3. Crystai binding. In *Introduction to solid state physics.* 3rd edition, John Wiley & Sons, Inc., 1966.

[108] R.Zanoni, C.Naselli, J.Bell, G.I.Stegeman, and C.T.Seaton. *Phys. Rev. Lett.*, 57(22):2838-2840, 1986.

[109] L.Koch. How bacteriaa grow and divide in spite of internal hydrostatic pressure. *Can. J. Microbiol.*, 31:1071-1084, 1985.

[110] D.Mirelman. Biosynthesis and assembly of cell wall peptidoglycan. In *Bacterial outer membranes.* Ed:M.Inouye. John Wiley & Sons, New York, 115-116, 1978.

[111] H.J.Rogers, J.R.Perkins, and J.B.Ward. Microbial cell walls and membranes. Chapman & Hall. London, 1980.